Facultad de Ciencias

Departamento de Física de Materiales

Single photon source based on InGaN/GaN dot-in-a-wire heterostructure

PhD Thesis

Presentada por:
Ekaterina Chernysheva
Licenciada en Ciencias Físicas

Directora:
Snežana Lazić
Doctora en Ciencias Físicas

Madrid, 2016

RESUMEN

Esta tesis presenta una investigación sobre las propiedades ópticas, de las propiedades estructurales y ópticas de puntos cuánticos (PCs) formados en inclusiones de InGaN con distintas orientaciones (polares, semi-polares y no polares) incluidas en nanocolumnas de GaN. Las principales conclusiones son las siguientes:

- Los puntos cuánticos polares de InGaN de las estructuras de InGaN/GaN tienen una alta calidad de emisión óptica con alto grado de polarización lineal y son visibles hasta 80 K. El origen de la formación se atribuye a fluctuaciones aleatorias de concentración de In. La sección eficaz de absorción obtenida está entre las más altas reportadas para puntos cuánticos semiconductores. Las vidas medias estimadas de los excitones están en el rango de nanosegundos. Estos puntos cuánticos constituyen fuentes de fotones individuales, como demuestran las medidas de interferometría Hanbury Brown y Twiss. Los valores estimados de la función de correlación de segundo orden a retardo de tiempo cero están muy por debajo del umbral de dos fotones. Esta fuente de fotones individuales emite en el espectro visible y opera hasta un rango de 1 GHz.
- La modulación espectral dinámica de la emisión de los PCs polares de InGaN se consiguió mediante el uso de ondas acústicas superficiales y diferentes técnicas estroboscópicas. La modulación obtenida de la energía de emisión para el exciton y el biexciton es un paso prometedor hacia la realización de una fuente sintonizable de fotones individuales operando a alta frecuencia sin necesidad de excitación pulsada. Además, se obtuvo la modulación acústicamente inducida de la energía de ligadura del biexcitón sin ninguna degradación apreciable de la intensidad de emisión. También se determinó que el campo piezoeléctrico lateral es responsable de la inyección de pares de electrones-huecos en el PC desde la región InGaN circundante.
- Los PCs de InGaN formados en los planos semi-polares y no polares de la heterostructura de nanocolumna con capa lateral (core-shell) poseen cualidades similares a sus homólogos polares. Debido a la influencia reducida del campo eléctrico interno para los planos semi-polares y no polares, las vidas de emisión son más pequeñas y en el rango de picosegundos. Se obtuvo en una sola nanocolumna una fuente de fotones que emitía en las regiones espectrales ultravioleta (PCs no polares), violeta (PCs semi-polares) y visible (PCs polares). El régimen de operación alcanza hasta 2,1 GHz, lo que hace que este dispositivo sea adecuado para aplicaciones de alta frecuencia en el campo del procesamiento de información cuántica.

Los resultados obtenidos son un paso prometedor hacia la realización de un emisor de fotones individuales sintonizable dinámicamente con alto grado de polarización lineal y operando a alta frecuencia, que es un componente crucial para la computación cuántica óptica lineal, la comunicación cuántica, la criptografía cuántica y la distribución de claves cuánticos.

INTRODUCCIÓN Y OBJETIVOS

Una fuente de fotones individuales (FFI) es un componente fundamental para los experimentos de óptica cuántica. La manera común de realizarla es usar un sistema de dos niveles: primer estado excitado y estado fundamental. El proceso de excitación transfiere un electrón del estado fundamental al estado excitado, seguido por la recombinación y la emisión de un fotón. Después de eso no se pueden emitir más fotones hasta que el sistema se excite de nuevo. La primera demostración exitosa de una FFI fue realizado utilizando átomos individuales *[Kim 1977]*. La primera realización de FFI en estado sólido fue en vacantes de diamante *[Kur 2000]*, puntos cuánticos (PCs) coloidales CdSe *[Mic 2000]* y por puntos cuánticos de InAs crecidos epitaxialmente *[Mic1 2000]*. Aunque los átomos son sistemas de dos niveles perfectos, la manipulación de átomos individuales es muy difícil, lo que resulta en experimentos complejos. Además, las vidas atómicas típicas de decenas de ns limitan el ritmo de generación de fotones individuales. Al contrario, los puntos cuánticos semiconductores, a veces también conocidos como "átomos artificiales", son más prometedores debido a sus propiedades excepcionales: escalabilidad, vidas cortas, líneas de emisión estrechas, posibilidad de excitación eléctrica, etc. Además, los puntos cuánticos epitaxiales son compatibles con modernas tecnologías de semiconductores y pueden integrarse fácilmente con otras estructuras de semiconductores. Por ejemplo, la incorporación de los PCs en nanocolumnas permite mejorar la emisión de FFIs aprovechando la mayor calidad estructural de las columnas. También permite el control de las propiedades de polarización de PCs *[Des 2013]* y mejorar la eficiencia de emisión y la direccionalidad *[Cla 2010; Gre 2008]* que es un requisito clave para las comunicaciones cuánticas a larga distancia. El primer efecto se logra a través de la fuerte atenuación del campo eléctrico perpendicular al eje c de la nanocolumna debido a la gran diferencia de constantes dieléctricas entre el aire y el material de la columna. En el segundo caso, un aumento de la eficiencia y la direccionalidad de la emisión se consiguen afilando la parte superior de la columna. Tal diseño es una alternativa interesante a las estructuras PC-microcavidad porque elimina restricciones sobre la longitud de onda de emisión PC asociada a la resonancia de la cavidad. Una radiación altamente direccional es ideal para la recogida en una fibra óptica para aplicaciones como distribución de claves cuánticas, así como el acoplamiento a guías integradas de onda, para la gestión de la información cuántica en el chip.

Avances significativos en fuentes de fotones individuales basadas en compuestos III-As se han demostrado recientemente. Se han conseguido con éxito emisores de fotones individuales bombeados eléctricamente *[Pat 2010; Ben 2000; Yua 2002]* y ópticamente *[Shi 2002; Shi 2003; San 2001]*. Sin embargo, este sistema material sólo puede cubrir la región espectral infrarroja (IR). El uso de PCs de InP/GaInP *[Now 2009]* y CdSe *[Lou 2000; Seb 2002]* permitió ampliar el régimen de operación hasta ~ 520 nm. Se puede conseguir una extensión adicional hacia regiones azules y ultravioletas (UV), que son deseables para la comunicación en el espacio libre, empleando FFIs basados en PCs de nitruros del grupo III. Por otra parte, los nitruros son muy prometedores debido a la posibilidad de funcionamiento a alta temperatura, amplio rango espectral de UV a IR, alto grado de

polarización lineal y piezoelectricidad *[Zhu 2016]*. Recientemente se ha publicado una demostración exitosa de la operación de FFIs basados en nitruros del grupo III a temperatura ambiente *[Hol 2014]*.

Aparte de la utilidad para comprobar aspectos fundamentales de la mecánica cuántica, los FFIs son componentes vitales para la computación cuántica óptica *[Jen 2010; Kni 2001; Nie 2000; Obr 2007]*, memorias cuánticas *[Lvo 2009]*, comunicación cuántica *[Kuz 2003]*, criptografía cuántica y distribución de claves cuánticas *[Yam 2005; Wak 2002]*, teleportación cuántica *[Yam 2005; Fat 2004; Fat1 2004]*, metrología *[Gio 2006]*, etc. La ventaja principal de un objeto mecánico cuántico para las comunicaciones seguras es su modificación, en cualquier intento de medirlo. Esta propiedad está en la base de muchos protocolos para la distribución de claves seguras *[Wak 2002]* ya que cualquier interceptación de la señal por un intruso puede ser detectado inmediatamente. La capacidad de manipular las propiedades de los fotones abre la posibilidad de construir sistemas para una computación excepcionalmente rápida, alta densidad de almacenamiento y comunicación en el espacio libre. Por ejemplo, un alto grado de polarización lineal es vital para la computación cuántica óptica lineal o la criptografía cuántica. Además, se desea un FFI sintonizable con línea de emisión estrecha para permitir la selección de una longitud de onda óptima para una aplicación particular. Muchos grupos de investigación centraron sus esfuerzos en buscar las maneras de controlar las propiedades ópticas de puntos cuánticos. Varios métodos de deformación elástica e ingeniería eléctrica se emplearon con éxito para la manipulación de la energía de emisión de los PC *[Zha 2015; Zha 2016, Zha 2014]*. En este contexto, recientemente se logró un notable progreso en las FFIs basadas en materiales III-As para demostrar con éxito un PC-FFI controlado acústicamente *[Cou 2009; Her 2012; Gel 2008]*. Esto abrió la posibilidad de obtener emisores de fotones individuales sintonizables dinámicamente sin el uso de excitación óptica pulsada. Además, se consiguió una operación de alta velocidad, hasta el rango de GHz. La modulación acústica también permite controlar el desdoblamiento de estructura fina de un excitón e incluso cancelarlo. Esto hace posible obtener pares de fotones enredados, que son cruciales para la computación cuántica escalable y la comunicación con protocolos ópticos lineales *[Ver 2014; Pat 2010]*. Sin embargo, los informes sobre la aplicación de técnicas similares en los PC-FFI basados en nitruros son escasos.

El propósito general de esta Tesis es profundizar en el conocimiento de los PC-FFI basados en nitruros e intentar extender el control dinámico de algunas propiedades de FFIs basadas en arseniuros a nitruros del grupo III.

En particular, esta Tesis se centra en la investigación de las propiedades ópticas de fuentes de fotónes individuales basados en PC de InGaN/GaN inmersos en nano-columnas de GaN. Se ha observado la emisión de fotónes individuales por PCs formados en planos no polares, semi-polares y polares de las heterostructuras. Se ha llevado a cabo una profunda investigación de las propiedades ópticas de los PCs formados en diferentes planos cristalográficos por medio de espectroscopía de micro-fotoluminiscencia resuelta en tiempo y en la polarización. La emisión de fotones individuales fue confirmada mediante medidas de correlación de fotones realizadas utilizando interferometría Hanbury Brown y Twiss (HBT). La influencia de ondas acústicas de

superficie (SAWs) sobre las propiedades ópticas de PC se investigó mediante espectroscopía óptica. En particular se ha estudiado el efecto de la SAW en la energía de emisión de los PC y la modulación de su intensidad por el campo de deformación y el campo piezoeléctrico inducidos por la SAW.

La estructura de Tesis es la siguiente:

El Capítulo 2 presenta una breve revisión de las propiedades estructurales, electrónicas y ópticas de los sistemas basados en nitruros del grupo III, seguida del caso más específico de los puntos cuánticos. Se dan los fundamentos de la teoría de la correlación de fotones. Finalmente, se presenta una introducción a las ondas acústicas superficiales en heterostructuras de semiconductores con una breve visión de los avances recientes en esta área.

En *El Capítulo 3* se da la descripción de las técnicas experimentales. Se presentan los detalles sobre la configuración óptica para micro-fotoluminiscencia (μ-FL) resuelta en el espacio, la polarización y el tiempo, seguido de la interferometría HBT y las técnicas de excitación y de detección estroboscópicos.

El Capítulo 4 se ocupa de las propiedades ópticas de los puntos cuánticos formados en planos polares de nanodiscos de InGaN incluidos en nanocolumnas de GaN. Se da una descripción detallada del crecimiento de las matrices de nanocolumnas ordenadas periódicamente. Las mediciones de μ-FL en muestras originales (tal como han sido crecidas) y dispersadas revelan líneas de emisión intensas y estrechas, presentes hasta 80 K, en el región espectral visible. Estas líneas fueron asignadas a transiciones de excitones confinados en puntos cuánticos formados por las fluctuaciones de concentración de In. La mayor parte de los puntos cuánticos investigados tienen un alto grado de polarización lineal, típico del sistema InGaN. Se obtuvieron tiempos de recombinación de excitones en el rango de ns mediante μ-FL resuelta en tiempo. La estadística de fotones se estudió mediante mediciones de autocorrelación. Se obtuvieron valores de la función de correlación de segundo orden $g^{(2)}(0)$ muy por debajo del umbral 0.5, que corresponde a la emisión de dos fotones independientes, probando así el funcionamiento como FFI de los PC en las nanocolumnas en estudio. Finalmente, el ritmo de recombinación de excitones ($\sim$ 1 GHz) y la sección eficaz de absorción ($\sim 10^{-14}$ cm^2) de los puntos cuánticos se estimaron a partir de la medición de la función de autocorrelación en función de la potencia bajo excitación óptica continua.

El Capítulo 5 contiene una investigación detallada de las propiedades ópticas de los PCs polares (P), semi-polares (SP) y no polares (NP) formados en la capa interna de GaN en las nanocolumnas. Se observaron líneas de emisión estrechas en las regiones: visible (P PCs), violeta (SP PCs) y ultravioleta (NP PCs) con alto grado de polarización lineal. Los tiempos de vida de las emisiones variaban desde el intervalo de ns hasta ps y seguían la secuencia $\tau_{NP} < \tau_{SP} < \tau_{polar}$. El funcionamiento como FFI fue demostrado mediante interferometría HBT bajo excitación cw para

P PCs y excitación óptica pulsada para SP PCs y NP PCs y los valores resultantes de $g^{(2)}(0)$ fueron inferiores a 0.5.

En *El Capítulo 6* se investiga la modulación acústicamente inducida de las propiedades ópticas de las PCs polares. La modulación dinámica inducida por las SAW de los picos del excitón y el biexcitón se estudió para diferentes potencias acústicas y se discutió en términos del campo deformación inducido por las ondas acústicas con una posible contribución de la componente transversal del campo piezoeléctrico inducido por la SAW. La energía de ligadura del biexciton también es modulada por el campo deformación de la SAW. Finalmente, se encontró que se produce la inyección simultánea de electrones y huecos en los PC desde el disco de InGaN circundante y se discutió en términos de la componente longitudinal del campo piezoeléctrico inducido por la SAW.

En *El Capítulo 7* se presentan las conclusiones generales de esta Tesis.

References

[Ben 2000] Benson, O., Santori, C., Pelton, M. & Yamamoto, Y. Regulated and Entangled Photons from a Single Quantum Dot. *Phys. Rev. Lett.* **84,** (2000).

[Cla 2010] Claudon, J., Bleuse, J., Malik, N. S., Bazin, M., Jaffrennou, P., Gregersen, N., Sauvan, C., Lalanne, P. & Gérard, J.-M. A highly efficient single-photon source based on a quantum dot in a photonic nanowire. *Nat. Photonics* **4,** 174–177 (2010).

[Cou 2009] Couto, O. D. D., Lazić, S., Iikawa, F., Stotz, J. A. H., Jahn, U., Hey, R. & Santos, P. V. Photon anti-bunching in acoustically pumped quantum dots. *Nat. Photonics* **3,** 645–648 (2009).

[Des 2013] Deshpande, S., Heo, J., Das, A. & Bhattacharya, P. Electrically driven polarized single-photon emission from an InGaN quantum dot in a GaN nanowire. *Nat. Commun.* **4,** 1675 (2013).

[Fat 2004] Fattal, D., Inoue, K., Vučković, J., Santori, C., Solomon, G. & Yamamoto, Y. Entanglement Formation and Violation of Bell's Inequality with a Semiconductor Single Photon Source. *Phys. Rev. Lett.* **92,** 37903 (2004).

[Fat1 2004] Fattal, D., Diamanti, E., Inoue, K. & Yamamoto, Y. Quantum Teleportation with a Quantum Dot Single Photon Source. *Phys. Rev. Lett.* **92,** 37904 (2004).

[Gel 2008] Gell, J. R., Ward, M. B., Young, R. J., Stevenson, R. M., Atkinson, P., Anderson, D., Jones, G. A. C., Ritchie, D. A. & Shields, A. J. Modulation of single quantum dot energy levels by a surface-acoustic-wave. *Appl. Phys. Lett.* **93,** 81115 (2008).

[Gio 2006] Giovannetti, V., Lloyd, S. & Maccone, L. Quantum Metrology. *Phys. Rev. Lett.* **96,** 10401 (2006).

[Gre 2008] Gregersen, N., Nielsen, T. R., Claudon, J., Gérard, J.-M. & Mørk, J. Controlling the emission profile of a nanowire with a conical taper. *Opt. Lett.* **33,** 1693–1695 (2008).

[Her 2012] Hernández-Mínguez, A., Möller, M., Breuer, S., Pfüller, C., Somaschini, C., Lazić, S., Brandt, O., García-Cristóbal, A., de Lima, M. M., Cantarero, A., Geelhaar, L., Riechert, H. & Santos, P. V. Acoustically Driven Photon Antibunching in Nanowires. *Nano Lett.* **12,** 252–258 (2012).

[Hol 2014] Holmes, M. J., Choi, K., Kako, S., Arita, M. & Arakawa, Y. Room-temperature triggered single photon emission from a III-nitride site-controlled nanowire quantum dot. *Nano Lett.* **14,** 982–6 (2014).

[Jen 2010] Jennewein, T., Barbieri, M. & White, A. G. Single-photon device requirements for operating linear optics quantum computing outside the post-selection basis. *J. Mod. Opt.* **58,** 37–41 (2010).

[Kim 1977] Kimble, H. J., Dagenais, M. & Mandel, L. Photon antibunching in resonance fluorescence. *Phys. Rev. Lett.* **39,** 691–695 (1977).

[Kni 2001] Knill, E., Laflamme, R. & Milburn, G. J. A scheme for efficient quantum computation with linear optics. *Nature* **409,** 46–52 (2001).

[Kur 2000] Kurtsiefer, C., Mayer, S., Zarda, P. & Weinfurter, H. Stable Solid-State Source of Single Photons. *Phys. Rev. Lett.* **85,** 290–293 (2000).

[Kuz 2003] Kuzmich, A., Bowen, W. P., Boozer, A. D., Boca, A., Chou, C. W., Duan, L.-M. & Kimble, H. J. Generation of nonclassical photon pairs for scalable quantum communication with atomic ensembles. *Nature* **423,** 731–734 (2003).

[Lou 2000] Lounis, B., Bechtel, H. A., Gerion, D., Alivisatos, P. & Moerner, W. E. Photon antibunching in single CdSe/ZnS quantum dot fluorescence. *Chem. Phys. Lett.* **329,** 399–404 (2000).

[Lvo 2009] Lvovsky, A. I., Sanders, B. C. & Tittel, W. Optical quantum memory. *Nat. Photonics* **3,** 706–714 (2009).

[Mic 2000] Michler, P., Imamoglu, A, Mason, M., Carson, P., Strouse, G. & Buratto, S. Quantum correlation among photons from a single quantum dot at room temperature. *Nature* **406,** 968–70 (2000).

[Mic1 2000] Michler, P., Kiraz, A, Becher, C., Schoenfeld, W. V, Petroff, P. M., Zhang, L., Hu, E. & Imamoglu, A. A quantum dot single-photon turnstile device. *Science* **290,** 2282–5 (2000).

[Nie 2000] Nielson, M. A. & Chuang, I. L. *Quantum Computation and Quantum Information*. *Cambridge Univ. Press* (Cambridge University Press, 2000).

[Now 2009] Nowak, A., Gallardo, E., Sarkar, D., van der Meulen, H., Calleja, J., Ripalda, J., González, L. & González, Y. Thermal effects in InP/(Ga,In)P quantum-dot single-photon emitters. *Phys. Rev. B* **80,** 161305 (2009).

[Obr 2007] O'Brien, J. L. Optical Quantum Computing. *Science.* **318,** 1567–1570 (2007).

[Pat 2010] Patel, R. B., Bennett, A. J., Cooper, K., Atkinson, P., Nicoll, C. A., Ritchie, D. A. & Shields, A. J. Quantum interference of electrically generated single photons from a quantum dot. *Nanotechnology* **21,** 274011 (2010).

[San 2001] Santori, C., Pelton, M., Solomon, G., Dale, Y. & Yamamoto, Y. Triggered Single Photons from a Quantum Dot. *Phys. Rev. Lett.* **86,** 1502–1505 (2001).

[Seb 2002] Sebald, K., Michler, P., Passow, T., Hommel, D., Bacher, G. & Forchel, A. Single-photon emission of CdSe quantum dots at temperatures up to 200 K. *Appl. Phys. Lett.* **81,** 2920–2922 (2002).

[Shi 2002] Shields, A. J., Stevenson, R. M., Thompson, R. M., Yuan, Z. & Kardynal, B. E. chapter in *Nano-Physics Bio-Electronics A New Odyssey* 111–146 (Elsevier, 2002).

[Shi 2003] Shields, A. J., Stevenson, R. M., Thompson, R. M., Ward, M. B., Yuan, Z., Kardynal, B. E., See, P., Farrer, I., Lobo, C., Cooper, K. & Ritchie, D. a. Self-assembled quantum dots as a source of single photons and photon pairs. *Phys. status solidi* **238,** 353–359 (2003).

[Ver 2014] Versteegh, M. A M., Reimer, M. E., Jöns, K. D., Dalacu, D., Poole, P. J., Gulinatti, A., Giudice, A. & Zwiller, V. Observation of strongly entangled photon pairs from a nanowire quantum dot. *Nat. Commun.* **5,** 5298 (2014).

[Wak 2002] Waks, E., Inoue, K., Santori, C., Fattal, D., Vuckovic, J., Solomon, G. S. & Yamamoto, Y. Secure communication: quantum cryptography with a photon turnstile. *Nature* **420,** 762 (2002).

[Yam 2005] Yamamoto, Y., Santori, C., Solomon, G., Vuckovic, J., Fattal, D., Waks, E. & Diamanti, E. Single photons for quantum information systems. *Prog. Informatics* 5–37 (2005).

[Yua 2002] Yuan, Z., Beata E. Kardynal, Stevenson, R. M., Shields, A. J., Lobo, C. J., Cooper, K., Beattie, N. S., Ritchie, D. A. & Pepper, M. Electrically Driven Single-Photon Source. *Science (80-.).* **295,** 102–105 (2002).

[Zha 2014] Zhang, L., Teng, C.-H., Ku, P. C. & Deng, H. Electrically driven single-photon emission from site-controlled InGaN/GaN quantum dots. *CLEO 2014 Postdeadline Pap. Dig.* **1,** JTh5B.6 (OSA, 2014).

[Zha 2015] Zhang, J., Wildmann, J. S., Ding, F., Trotta, R., Huo, Y., Zallo, E., Huber, D., Rastelli, A. & Schmidt, O. G. High yield and ultrafast sources of electrically triggered entangled-photon pairs based on strain-tunable quantum dots. *Nat. Commun.* **6,** 10067 (2015).

[Zha 2016] Zhang, L., Teng, C.-H., Ku, P.-C. & Deng, H. Site-controlled InGaN/GaN single-photon-emitting diode. *Appl. Phys. Lett.* **108,** 153102 (2016).

[Zhu 2016] Zhu, T. & Oliver, R. A. Nitride quantum light sources. *EPL (Europhysics Lett.* **113,** 38001 (2016).

CONCLUSIONES

En esta Tesis se han investigado matrices ordenadas de nanocolumnas hexagonales de GaN incluyendo puntos cuánticos (PCs) de InGaN crecidos por epitaxia por haces molecular asistida por plasma. Se estudiaron las propiedades ópticas de los puntos cuánticos de InGaN formados en los planos polares, semi-polares y no polares. Para la espectroscopía de nanocolumnas individuales, los nanocolumnas se retiraron de su sustrato nativo y se dispersaron sobre una oblea de silicio. Un patrón metálico, modelado sobre la superficie del silicio, facilitó el acceso a nanocolumnas individuales. Las principales conclusiones se dividen en dos partes, correspondientes a los PCs polares, y a los semi-polares y no polares respectivamente, seguidas de las observaciones finales:

- InGaN/GaN PCs polares

  - ✓ Se ha realizado el análisis estructural, las propiedades ópticas y las estadísticas de fotones de PCs de InGaN formados en las estructuras de InGaN/GaN disco-en-columna. El análisis estructural realizado por catódoluminiscencia resuelta en el espacio y espectralmente reveló la formación de dos regiones distintas de InGaN dentro de la punta de la nanocolumna. La más gruesa se forma en el plano polar (ápice de la columna), y tiene la más alta concentración de In. La segunda región de InGaN está formada en las facetas laterales semi-polares de la nanocolumna. Mediante tomografía lineal de cátodoluminiscencia (CL), tomada a diferentes alturas de la columna, se reveló la distribución no uniforme del contenido de In. La espectroscopia de micro-fotoluminiscencia a baja temperatura confirmó los hallazgos de CL, revelando bandas de emisión similares. El origen de estas bandas se discutió en términos de incorporación de In y diferencias en el campo eléctrico para los planos cristalográficos con polaridades diferentes.

  - ✓ Además, la emisión de la parte superior del nanodisco de InGaN (región polar) muestra picos estrechos e intensos superpuestos sobre un fondo ancho. Las líneas estrechas se atribuyeron a los potenciales de confinamiento similares a puntos cuánticos formados por fluctuaciones aleatorias de In, y el fondo a la emisión de la región circundante de pozo cuántico de InGaN. Los espectros de μ-FL registrados para columnas individuales mostraron ocasionalmente más de un pico de emisión, confirmando el origen sugerido de tales PC. Los PCs emiten en el rango espectral visible y son observables hasta 80 K. La mayoría de las líneas de emisión investigadas tienen un alto grado de polarización lineal con dirección de polarización aleatoria. Esta fuerte polarización lineal es de gran importancia para numerosas aplicaciones en el campo del procesamiento de la información cuántica (por ejemplo, distribución de claves cuánticas y computación cuántica). Los picos observados se asignaron a excitones y biexcitones, como atestigua la

dependencia de la intensidad integrada del correspondiente pico con la potencia. No se detectó desdoblamiento de estructura fina. Los tiempos de recombinación de excitones, medidos por μ-FL resuelta en tiempo, estaban en el rango de nanosegundos.

El funcionamiento como emisores de fotones individuales de los nanocolumnas-PCs se demostró por el fuerte antibunching observado en las medidas de correlación de fotones para dos geometrías de nanocolumnas (crecidas e individuales dispersadas). La función de correlación de segundo orden a retardo de tiempo cero, después del procedimiento de corrección, estaba muy por debajo del umbral 0.5 tanto para las columnas crecidas como las individuales dispersadas, demostrando así la emisión de fotones individuales. Los tiempos de recombinación de excitones se estimó a partir de las mediciones de autocorrelación dependientes de la potencia con excitación contínua para nanocolumnas individuales dispersadas. El valor obtenido en el rango de GHz está en buen acuerdo con la medición directa de la vida del exciton por μ-FL resuelta en el tiempo. Tales emisores de fotones individuales son muy atractivos para aplicaciones de procesamiento de información cuántica a alta frecuencia. Además, se estimó la sección eficaz de absorción de las mismas medidas de autocorrelación dependiente de la potencia y su valor estimado fue alto en comparación con otros PCs de semiconductores.

- ✓ Se logró la modulación de las energías de emisión inducida por ondas acústicas de superficie (SAW) tanto para el excitón como el biexciton. Se determinó que el campo de deformación inducido por SAW es responsable de la división de los picos del excitón y biexcitón en dobletes en los espectros promediados en tiempo. La amplitud de modulación alcanza 1.51 meV para el excitón y 1.62 meV para el biexcitón para la mayor potencia acústica aplicada. La dependencia sub-lineal del desdoblamiento en energía con la amplitud de SAW para ambas líneas de emisión fue explicada por el acoplamiento mediante el mecanismo de potencial de deformación con una posible contribución del efecto Stark lineal confinado cuántico, esperado para III-Nitruros. También se logró una modulación inducida por SAW de la energía de ligadura del biexcitón hasta 100 μeV sin ninguna degradación apreciable de su emisión, permitiendo ası el control in-situ del sistema exciton-biexciton. Se encontró que cuando la potencia acústica aumenta, la energía de ligadura del biexciton aumenta linealmente para la compresión y disminuye por tensión. Este comportamiento se discutió en términos de interacciones Coulomb dentro del complejo biexcitónico.

- ✓ El uso de diferentes técnicas estroboscópicas permitió observar las oscilaciones de la energía de emisión del excitón y del biexcitón. Este último se observa en espectros de μ-FL promediados en el tiempo, mientras que las oscilaciones de

energía excitónica se observan en espectros de μ-FL resueltos en el tiempo. Esta diferencia se explicó por la relación entre la vida del fotón emitido y la mitad del período de la SAW. El decaimiento de la intensidad de emisión para ambos complejos excitónicos se estudió para varias fases de SAW revelando oscilaciones periódicas de intensidad. Estas oscilaciones se asignaron a la inyección de pares de electrones-huecos en el PC de la región InGaN circundante debido a la componente lateral del campo piezoeléctrico inducido por SAW.

- InGaN/GaN PCs semi-polares and non-polares

  - ✓ En las nanocolumnas con capa lateral (core-shell), se formaron puntos cuánticos en diferentes planos cristalográficos de la región InGaN: semi-polares y no polares (además de los polares). Sus propiedades ópticas fueron investigadas mediante espectroscopia μ-FL y CL, revelando tres bandas de emisión, correspondientes a las tres orientaciones. Los PCs polares emiten en el rango espectral visible, los PCs semi-polares en el violeta y los PCs no polares en el ultravioleta. La diferencia en la energía de emisión de PCs se discutió en términos del contenido de In, la geometría (tamaño/forma), el confinamiento y el efecto del campo piezoeléctrico. Los tres tipos de PCs tienen también alto grado de polarización lineal y no mostraron ningún desdoblamiento de estructura fina. La dirección de polarización aleatoria, encontrada para todos los PCs investigados, es consistente con las fluctuaciones de In como origen de tales centros de emisión. Los tiempos de decaimiento estaban en el rango de picosegundos para PC semi- y no polares y seguían la secuencia: $\tau_{NP} < \tau_{SP} < \tau_{polar}$. Se observó una tendencia a tiempos de vida más cortos para PCs más pequeños (que emitían a mayor energía). Además, los PCs semi-polares mostraron mayor dependencia con el tamaño que los no polares. Esta diferencia se explica por el menor efecto del campo piezoeléctrico en los PCs no polares, ya que en este caso el campo eléctrico interno está en el plano m y afecta sólo a la separación lateral de electrones y huecos, mientras que el confinamiento vertical está fijado por las barreras de GaN. La naturaleza no clásica de la luz emitida fue demostrada mediante interferometría HBT. Los valores de la función de correlación de segundo orden a retardo de tiempo cero corregidas estaban por debajo del umbral de dos fotones para PCs de todas las polaridades.

- Observaciones finales

  - ✓ Se obtuvo una fuente de fotones individuales (FFI) en estructuras de disco cuántico inmersas en una nanocolumna, polarizada linealmente emitiendo en el rango espectral visible, así como un FFI multicolor de capa lateral (core-shell), que abarcaba desde el ultravioleta hasta el visible, ambos operando en el rango de GHz. Los valores bajos de la función de correlación de segundo orden para estos FFIs abre una

oportunidad para la realización de dispositivos de procesamiento de información cuántica de alta velocidad. Además, su integración en las nanocolumnas facilita su transferencia y combinación con otros componentes de dispositivos optoelectrónicos sobre chip. El alto grado de polarización hace de estos FFIs una herramienta atractiva para la distribución de claves cuánticas, la criptografía cuántica y las aplicaciones de computación cuántica óptica lineal. Además, su combinación con la tecnología SAW abre la posibilidad del control dinámico bajo demanda de las propiedades ópticas del emisor de fotones individuales.

ACKNOWLEDGEMENTS

First of all I would like to acknowledge my supervisor Prof. Dr. Snežana Lazić for teaching me about the semiconductor quantum dots physics and its various experimental aspects, for patience, valuable advices and discussions.

Also, I would like to express my deepest gratitude to Prof. Dr. Jose Manuel Calleja for fruitful scientific discussions, critical revisions of results and valuable advices, for constant support, encouragement and taking care of all difficulties of my moving to Spain.

I thank Prof. Dr. Herko van der Muelen for help and support in the laboratory, and enjoyable discussions during coffee breaks.

My acknowledgments to Prof. Dr. Enrique Calleja and Prof. Dr. Žarko Gačević from ISOM-UPM for providing samples for this work. Also, thanks to Prof. Dr. Žarko Gačević for SEM and CL measurements. Many thanks to Maria del Carmen Sabido Siller and David López-Romero Moraleda for sample processing and bonding.

This work was done in collaboration with many groups. I would like to acknowledge Dr. Marcus Müller from group of Prof. Dr. Jürgen Christen at Otto-von-Guericke-University in Magdeburg, Germany, for providing STEM (HAADF) measurements. For TRPL and HBT experiments on semi-polar and non-polar QDs I thank Dr. Mark Holmes (group of Prof. Dr. Yasuhiko Arakawa) at the Institute of Industrial Science, The University of Tokyo, Japan. Many thanks for HRTEM measurements to Prof. Dr. Almudena Torres-Pardo from Prof. Dr. J.M. González-Calbet's group UCM-UPM, Madrid.

During PhD I had an opportunity to visit other laboratories, get involved in various scientific activities and meet new people. I would like to express my deepest gratitude to Prof. Dr. Paulo Santos, Dr. Alberto Hernandez-Mingez, Dr. Edgar Cerda, Jacob Buller and Collin Hubert for extending to me the facilities of Semiconductor Spectroscopy Department, kind and friendly atmosphere during my short stay in PDI. I've enjoyed our fruitful discussions and time we spent together. I am also grateful to Prof. Dr. Manfred Ramsteiner, Prof. Dr. Oliver Brandt, Dr. Pierre Corfdir and Dr. Sergio Fernández-Garrido. I would also like to thank the PDI Technical Department for sample processing and experimental setup modifications.

Many thanks to my UAM colleagues (Carlos, Lola, Pablo, Fabrice, Ueslen, Jorge, Dipi, Francesca) for the interesting discussions and enjoyable time we spent together. I am grateful to Prof. Dr. Luis Viña and Prof. Dr. Luisa Bausa for the extending to me their laboratory facilities. My acknowledgments to Prof. Dr. Carlos Tejedor for providing a fellowship for me. Thanks to Elias and Javier for technical support and helium delivery.

Finally, I would like to thank my family and friends for cheering up and just being there for me during these 4 years. I especially thank my husband, Pavel for support and great patience.

live and learn…

1 CONTENTS

1 CHAPTER. INTRODUCTION AND OBJECTIVES

A source of single photons is a fundamental building block for experiments in quantum optics. The common way to realize it is to use a two level system: first excited state and ground state. The excitation process transfers an electron from the ground state to the excited state, followed by the recombination and emission of one photon. After that no more photons can be emitted until the system is excited again. The first successful demonstration of single photon source (SPS) was achieved using single atoms *[Kim 1977]*. It was followed by the first solid state realization of SPS using diamond vacancies *[Kur 2000]*, colloidal CdSe quantum dots (QDs) *[Mic 2000]* and epitaxially grown InAs QDs *[Mic1 2000]*. Although atoms are perfect two level systems, handling of single atoms is very difficult, which results in complex experimental setups. Moreover, the typical atomic lifetimes of tens of ns limit the single photon generation rate. On the contrary, semiconductor QDs, sometimes also referred to as "artificial atoms", are more promising due to their exceptional properties: scalability, short lifetimes, narrow emission lines, possibility of electrical excitation, etc. Furthermore, epitaxially grown QDs are compatible with modern semiconductor technologies and can be easily integrated with other semiconductor structures. For example, embedding the QDs into nanowires allows to improve the SPS emission taking advantage of the increased structural quality of the wires. It also allows to control the QD polarization properties *[Des 2013]* and to enhance the emission efficiency and directionality *[Cla 2010; Gre 2008]*, which is a key requirement for long-distance quantum communications. The former effect is achieved through the strong attenuation of the electric field perpendicular to the nanowire c-axis due to large difference of dielectric constants between the surrounding air and NW material. As for the latter, an increased emission efficiency and directionality are achieved by tapering the wire top. Such a design is an interesting alternative to QD-microcavity structures removing restrictions on the QD emission wavelength associated to the cavity resonance. A highly directional radiation pattern is ideal for collection into a fiber for applications like quantum key distribution, as well as coupling to integrated waveguides, for on-chip quantum information management.

Significant progress in III-As based single photon sources has been recently demonstrated. Electrically *[Pat 2010; Ben 2000; Yua 2002]* and optically *[Shi 2002; Shi 2003; San 2001]* pumped emitters of single photons have been successfully achieved. However, this material system can only cover the infrared (IR) spectral region. The use of InP/GaInP *[Now 2009]* and CdSe QDs *[Lou 2000; Seb 2002]* allowed to broaden the operation regime up to ~ 520 nm. Further extension towards blue and ultraviolet (UV) wavelengths, which are desirable for free space communication, can be achieved by employing III-Nitride QDs based SPSs. Moreover, nitrides are very promising due to the possibility of high temperature operation, broad spectral range from UV to IR, high linear polarization degree and piezoelectricity *[Zhu 2016]*. A successful demonstration of room temperature operation of nitride-based SPSs has been recently published *[Hol 2014]*.

Apart from the usefulness to check fundamental aspects of quantum mechanics, SPSs are vital components for optical quantum computing *[Jen 2010; Kni 2001; Nie 2000; Obr 2007]*, quantum memories *[Lvo 2009]*, quantum communication *[Kuz 2003]*, quantum cryptography and quantum key distribution *[Yam 2005; Wak 2002]*, quantum teleportation *[Yam 2005; Fat 2004; Fat1 2004]*, metrology *[Gio 2006]*, etc. The main advantage of a quantum mechanical object for secure communications is its modification, upon any attempt to measure it. This property is at the base of many protocols for secure key distribution *[Wak 2002]* since any interception of the signal by an eavesdropper can be immediately detected. The ability to manipulate photon properties opens a possibility to construct the systems for exceptionally fast computing, high storage density and free space communication. For instance, a high degree of linear polarization is vital for linear optical quantum computing or quantum cryptography. Moreover, a tunable narrow linewidth SPSs is desired to allow the selection of an optimal wavelength for a particular application. Many research groups focused their attempts on searching the ways to control the QDs optical properties. Various methods of strain and electric engineering were successfully employed for the manipulation of the QD emission energy *[Zha 2015; Zha 2016, Zha 2014]*. In this context, a remarkable progress was achieved recently in III-As-based SPSs by successfully demonstrating an acoustically driven QD-SPSs *[Cou 2009; Her 2012; Gel 2008]*. That opened the possibility to obtain dynamically tunable single photon emitters without use of pulsed optical excitation. Furthermore, high speed operation, up to GHz range, was also achieved. Additionally, acoustic modulation allows to control the fine structure splitting of a QD exciton with the potential to cancel it. This makes it possible to obtain pairs of entangled photons, which are crucial for scalable quantum computing and communication with linear optics protocols *[Ver 2014; Pat 2010]*. However, the reports on implementation of similar techniques in nitride-based QD-SPSs are scarce.

The general purpose of this Thesis is to deepen on the knowledge of nitride-based QD-SPSs and to try to translate the dynamic control of some properties of arsenide-based SPSs onto III-N systems.

In particular, this Thesis is focused on the investigation of the optical properties of single photon sources based on InGaN/GaN QD-in-a-nanowire structures. It was possible to assess single photon emission by QDs formed on non-polar, semi-polar and polar planes of the nanowire heterostructures. A profound investigation of optical properties of nanowire-QDs formed on different crystallographic planes was conducted by means of micro-photoluminescence spectroscopy with time and polarization resolution. SPS action was attested by photon statistical measurements performed using Hanbury Brown and Twiss (HBT) interferometry. The influence of surface acoustic waves (SAWs) on the QD optical properties was investigated by means of optical spectroscopy. In particular the QD emission energy and intensity modulation by the SAW-induced strain and piezoelectric fields has been studied.

The Thesis structure is the following:

Chapter 2 gives a brief review of the structural, electronic and optical properties of III-Nitride based systems, followed by the more specific case of quantum dots. The basics of the photon-correlation theory are given. Finally, an introduction to surface acoustic waves in semiconductor heterostructures is presented with a brief insight on the recent progress in this area.

In *Chapter 3* the description of the experimental techniques is given. Details on the optical spectroscopy setup for micro-photoluminescence (μ-PL) with spatial, polarization and time resolution is presented, followed by the HBT interferometry and stroboscopic excitation and detection techniques.

Chapter 4 deals with the optical properties of QDs formed on polar planes of InGaN nanodisks embedded into site-controlled GaN nanowires. A detailed description of the growth of periodically ordered nanowire arrays is given. μ-PL measurements in both standing and dispersed samples reveal sharp intense and narrow emission lines up to 80 K in the visible spectral range. They were assigned to the exciton ground state transitions from QD-like centers formed by In concentration fluctuations. Most of the investigated QDs have a high degree of linear polarization, typical for the InGaN system. Exciton decay times in the ns range were obtained by time-resolved μ-PL. The photon statistics was studied by autocorrelation measurements. The zero time delay value of the second order correlation function $g^{(2)}(0)$ was obtained. This is well below the 0.5 threshold, which corresponds to the emission of the two independent photons, thereby proving the single photon performance of the nanowire-QDs under study. Finally the exciton decay rate ($\sim$ 1 GHz) and the absorption cross section ($\sim 10^{-14}$ cm^2) of the QDs were estimated from the power dependent autocorrelation measurement under continuous optical excitation.

Chapter 5 contains a detailed investigation of the optical properties of polar (P), semi-polar (SP) and non-polar (NP) QDs formed in the InGaN coreshell of GaN NW. Narrow emission lines in the visible (P QDs), the violet (SP QDs) and the ultra-violet (NP QDs) regions with high degree of linear polarization were observed. The emission lifetimes were varying from ns to ps range and followed the sequence $\tau_{NP} < \tau_{SP} < \tau_{polar}$. The single photon performance was attested by HBT interferometry under cw excitation for P QDs and pulsed optical excitation for SP QDs and NP QDs and the resulting values of $g^{(2)}(0)$ were below 0.5 threshold.

In *Chapter 6* the acoustically induced modulation of the optical properties of polar QD is investigated. The SAW-induced dynamic modulation of the exciton and biexciton peaks was studied for different acoustic powers and discussed in terms of the SAW strain field with a possible contribution of the transverse component of the SAW-induced piezoelectric field. The biexciton binding energy was also modulated by the SAW strain field. Finally, the simultaneous injection of electrons and holes into the QD from the surrounding InGaN disk was found and discussed in terms of the longitudinal component of the SAW-induced piezoelectric field.

In *Chapter 7* the general conclusions of this Thesis are presented.

References

[Ben 2000] Benson, O., Santori, C., Pelton, M. & Yamamoto, Y. Regulated and Entangled Photons from a Single Quantum Dot. *Phys. Rev. Lett.* **84,** (2000).

[Cla 2010] Claudon, J., Bleuse, J., Malik, N. S., Bazin, M., Jaffrennou, P., Gregersen, N., Sauvan, C., Lalanne, P. & Gérard, J.-M. A highly efficient single-photon source based on a quantum dot in a photonic nanowire. *Nat. Photonics* **4,** 174–177 (2010).

[Cou 2009] Couto, O. D. D., Lazić, S., Iikawa, F., Stotz, J. A. H., Jahn, U., Hey, R. & Santos, P. V. Photon anti-bunching in acoustically pumped quantum dots. *Nat. Photonics* **3,** 645–648 (2009).

[Des 2013] Deshpande, S., Heo, J., Das, A. & Bhattacharya, P. Electrically driven polarized single-photon emission from an InGaN quantum dot in a GaN nanowire. *Nat. Commun.* **4,** 1675 (2013).

[Fat 2004] Fattal, D., Inoue, K., Vučković, J., Santori, C., Solomon, G. & Yamamoto, Y. Entanglement Formation and Violation of Bell's Inequality with a Semiconductor Single Photon Source. *Phys. Rev. Lett.* **92,** 37903 (2004).

[Fat1 2004] Fattal, D., Diamanti, E., Inoue, K. & Yamamoto, Y. Quantum Teleportation with a Quantum Dot Single Photon Source. *Phys. Rev. Lett.* **92,** 37904 (2004).

[Gel 2008] Gell, J. R., Ward, M. B., Young, R. J., Stevenson, R. M., Atkinson, P., Anderson, D., Jones, G. A. C., Ritchie, D. A. & Shields, A. J. Modulation of single quantum dot energy levels by a surface-acoustic-wave. *Appl. Phys. Lett.* **93,** 81115 (2008).

[Gio 2006] Giovannetti, V., Lloyd, S. & Maccone, L. Quantum Metrology. *Phys. Rev. Lett.* **96,** 10401 (2006).

[Gre 2008] Gregersen, N., Nielsen, T. R., Claudon, J., Gérard, J.-M. & Mørk, J. Controlling the emission profile of a nanowire with a conical taper. *Opt. Lett.* **33,** 1693–1695 (2008).

[Her 2012] Hernández-Mínguez, A., Möller, M., Breuer, S., Pfüller, C., Somaschini, C., Lazić, S., Brandt, O., García-Cristóbal, A., de Lima, M. M., Cantarero, A., Geelhaar, L., Riechert, H. & Santos, P. V. Acoustically Driven Photon Antibunching in Nanowires. *Nano Lett.* **12,** 252–258 (2012).

[Hol 2014] Holmes, M. J., Choi, K., Kako, S., Arita, M. & Arakawa, Y. Room-temperature triggered single photon emission from a III-nitride site-controlled nanowire quantum dot. *Nano Lett.* **14,** 982–6 (2014).

[Jen 2010] Jennewein, T., Barbieri, M. & White, A. G. Single-photon device requirements for operating linear optics quantum computing outside the post-selection basis. *J. Mod. Opt.* **58,** 37–41 (2010).

[Kim 1977] Kimble, H. J., Dagenais, M. & Mandel, L. Photon antibunching in resonance fluorescence. *Phys. Rev. Lett.* **39,** 691–695 (1977).

[Kni 2001] Knill, E., Laflamme, R. & Milburn, G. J. A scheme for efficient quantum computation with linear optics. *Nature* **409,** 46–52 (2001).

[Kur 2000] Kurtsiefer, C., Mayer, S., Zarda, P. & Weinfurter, H. Stable Solid-State Source of Single Photons. *Phys. Rev. Lett.* **85,** 290–293 (2000).

[Kuz 2003] Kuzmich, A., Bowen, W. P., Boozer, A. D., Boca, A., Chou, C. W., Duan, L.-M. & Kimble, H. J. Generation of nonclassical photon pairs for scalable quantum communication with atomic ensembles. *Nature* **423,** 731–734 (2003).

[Lou 2000] Lounis, B., Bechtel, H. A., Gerion, D., Alivisatos, P. & Moerner, W. E. Photon antibunching in single CdSe/ZnS quantum dot fluorescence. *Chem. Phys. Lett.* **329,** 399–404 (2000).

[Lvo 2009] Lvovsky, A. I., Sanders, B. C. & Tittel, W. Optical quantum memory. *Nat. Photonics* **3,** 706–714 (2009).

[Mic 2000] Michler, P., Imamoglu, A, Mason, M., Carson, P., Strouse, G. & Buratto, S. Quantum correlation among photons from a single quantum dot at room temperature. *Nature* **406,** 968–70 (2000).

[Mic1 2000] Michler, P., Kiraz, A, Becher, C., Schoenfeld, W. V, Petroff, P. M., Zhang, L., Hu, E. & Imamoglu, A. A quantum dot single-photon turnstile device. *Science* **290,** 2282–5 (2000).

[Nie 2000] Nielson, M. A. & Chuang, I. L. *Quantum Computation and Quantum Information*. *Cambridge Univ. Press* (Cambridge University Press, 2000).

[Now 2009] Nowak, A., Gallardo, E., Sarkar, D., van der Meulen, H., Calleja, J., Ripalda, J., González, L. & González, Y. Thermal effects in InP/(Ga,In)P quantum-dot single-photon emitters. *Phys. Rev. B* **80,** 161305 (2009).

[Obr 2007] O'Brien, J. L. Optical Quantum Computing. *Science.* **318,** 1567–1570 (2007).

[Pat 2010] Patel, R. B., Bennett, A. J., Cooper, K., Atkinson, P., Nicoll, C. A., Ritchie, D. A. & Shields, A. J. Quantum interference of electrically generated single photons from a quantum dot. *Nanotechnology* **21,** 274011 (2010).

[San 2001] Santori, C., Pelton, M., Solomon, G., Dale, Y. & Yamamoto, Y. Triggered Single Photons from a Quantum Dot. *Phys. Rev. Lett.* **86,** 1502–1505 (2001).

[Seb 2002] Sebald, K., Michler, P., Passow, T., Hommel, D., Bacher, G. & Forchel, A. Single-photon emission of CdSe quantum dots at temperatures up to 200 K. *Appl. Phys. Lett.* **81,** 2920–2922 (2002).

[Shi 2002] Shields, A. J., Stevenson, R. M., Thompson, R. M., Yuan, Z. & Kardynal, B. E. chapter in *Nano-Physics Bio-Electronics A New Odyssey* 111–146 (Elsevier, 2002).

[Shi 2003] Shields, A. J., Stevenson, R. M., Thompson, R. M., Ward, M. B., Yuan, Z., Kardynal, B. E., See, P., Farrer, I., Lobo, C., Cooper, K. & Ritchie, D. A. Self-assembled quantum dots as a source of single photons and photon pairs. *Phys. status solidi* **238,** 353–359 (2003).

[Ver 2014] Versteegh, M. A. M., Reimer, M. E., Jöns, K. D., Dalacu, D., Poole, P. J., Gulinatti, A., Giudice, A. & Zwiller, V. Observation of strongly entangled photon pairs from a nanowire quantum dot. *Nat. Commun.* **5,** 5298 (2014).

[Wak 2002] Waks, E., Inoue, K., Santori, C., Fattal, D., Vuckovic, J., Solomon, G. S. & Yamamoto, Y. Secure communication: quantum cryptography with a photon turnstile. *Nature* **420,** 762 (2002).

[Yam 2005] Yamamoto, Y., Santori, C., Solomon, G., Vuckovic, J., Fattal, D., Waks, E. & Diamanti, E. Single photons for quantum information systems. *Prog. Informatics* 5–37 (2005).

[Yua 2002] Yuan, Z., Beata E. Kardynal, Stevenson, R. M., Shields, A. J., Lobo, C. J., Cooper, K., Beattie, N. S., Ritchie, D. A. & Pepper, M. Electrically Driven Single-Photon Source. *Science* **295,** 102–105 (2002).

[Zha 2014] Zhang, L., Teng, C.-H., Ku, P. C. & Deng, H. Electrically driven single-photon emission from site-controlled InGaN/GaN quantum dots. *CLEO 2014 Postdeadline Pap. Dig.* **1,** JTh5B.6 (OSA, 2014).

[Zha 2015] Zhang, J., Wildmann, J. S., Ding, F., Trotta, R., Huo, Y., Zallo, E., Huber, D., Rastelli, A. & Schmidt, O. G. High yield and ultrafast sources of electrically triggered entangled-photon pairs based on strain-tunable quantum dots. *Nat. Commun.* **6,** 10067 (2015).

[Zha 2016] Zhang, L., Teng, C.-H., Ku, P.-C. & Deng, H. Site-controlled InGaN/GaN single-photon-emitting diode. *Appl. Phys. Lett.* **108,** 153102 (2016).

[Zhu 2016] Zhu, T. & Oliver, R. A. Nitride quantum light sources. *Europhysics Letters* **113,** 38001 (2016).

2 CHAPTER. FUNDAMENTAL PROPERTIES OF III-NITRIDE SEMICONDUCTOR MATERIALS

2.1 CRYSTALLINE STRUCTURE

III-Nitrides have three different types of crystalline structure: wurtzite, zinc-blende and rock salt. The zinc-blende phase is metastable and requires specific growth conditions. The rock salt form is the rarest one and can be synthesized from wurtzite structure under high pressure. The most stable and, therefore, more commonly used is the wurtzite type (fig. 2.1.0.(a)) and it will be addressed in more details in this chapter and the following ones.

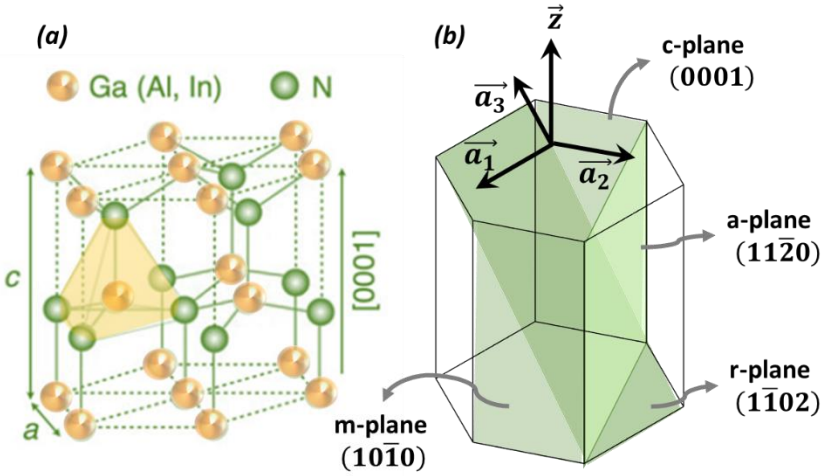

Fig. 2.1.0. (a) The wurtzite crystal unit cell. (b) Main directions and corresponding planes of the wurtzite structure.

The wurtzite nitrides possess hexagonal symmetry and are described by four main crystallographic directions, denoted by the Miller's indices [hkil]. The three first indices correspond to a_1, a_2 and a_3 axes lying in the hexagonal plane and thus are dependent: $h + k + i = 0$. The forth index corresponds to the direction (z) perpendicular to this plane, and is normally referred to as c-axis. The four main axes of the wurtzite crystal unit cell together with the corresponding planes are presented in fig. 2.1.0.(b).

Due to the hexagonal close-packed (hcp) structure III-Nitrides are anisotropic crystals, contrary to the cubic III-As systems, and thus have a significant difference in their properties. Their crystal structure is produced by insertion of two hcp sub-lattices corresponding to the two types of atoms with a relative shift between them along the z direction. Generally, hexagonal structures are characterized by three parameters: (i) *a*, which defines the edge length of basal hexagon, (ii) *c*, which, in turn defines the prism height and (iii) an internal parameter *u*, which stands for the

relative displacement of the two atomic sub-lattices along the c-axis. The geometric value of *u* is 0.375 (in units of c) and any deviations from this value in real structures are the origin of the spontaneous polarization typical for wurtzite materials. The corresponding values of the lattice parameters for GaN, InN and AlN at room temperature are presented in table 2.1.0.

Parameter (T=300K)	GaN	AlN	InN
a (Å)	3.189	3.112	3.545
c (Å)	5.185	4.982	5.703
u	0.3769	0.3814	0.3787

Table 2.1.0. Lattice parameters for GaN, AlN and InN at room temperature ***[Woo 2008]****.*

2.2 WURTZITE ELECTRONIC BAND STRUCTURE

The schematics of the wurtzite electronic band structure near the center of Brillouin zone, based on ***kp*** – Hamiltonian calculations ***[Aml 2013]*** is presented in fig. 2.2.0. In the absence of crystal field and spin-orbit interactions, there are three degenerate valence bands at ***k***=0. Once the crystal field interaction is included the valence band splits into two degenerated levels and one single state. The corresponding energy splitting is usually referred to as a crystal-field splitting, Δ_{CR}. The values of Δ_{CR} are 19 meV, 41 meV and -164 meV for GaN, InN and AlN, respectively ***[Vur 2001]***. The observed negative value for AlN results in the reverse order of two topmost VB levels ***[Wag 2002]***. Further introduction of spin-orbit interaction, splits the two remaining degenerate states. The respective energy difference is called spin-orbit split-off, Δ_{SO}. The corresponding values of Δ_{SO} are 14 meV, 19 meV and 1 meV for GaN, AlN and InN, respectively ***[Vur 2001]***. Thus, in the wurtzite structure there are three valence band levels, denoted as A, B and C bands following Amloy's notation.

The A, B and C valence band states are expressed as linear combination of the p-orbitals $|X\rangle$, $|Y\rangle$ and $|Z\rangle$:

$$
\begin{aligned}
|A\uparrow\rangle &= \tfrac{1}{\sqrt{2}}(|X\uparrow\rangle + i|Y\uparrow\rangle),\\
|A\downarrow\rangle &= \tfrac{1}{\sqrt{2}}(|X\downarrow\rangle - i|Y\downarrow\rangle),\\
|B\uparrow\rangle &= \tfrac{ia}{\sqrt{2}}(|X\downarrow\rangle + i|Y\downarrow\rangle - ib|Z\uparrow\rangle),\\
|B\downarrow\rangle &= \tfrac{a}{\sqrt{2}}(|X\uparrow\rangle - i|Y\uparrow\rangle + b|Z\downarrow\rangle),\\
|C\uparrow\rangle &= \tfrac{ib}{\sqrt{2}}(|X\downarrow\rangle + i|Y\downarrow\rangle + ia|Z\uparrow\rangle),\\
|C\downarrow\rangle &= \tfrac{b}{\sqrt{2}}(|X\uparrow\rangle - i|Y\uparrow\rangle - a|Z\downarrow\rangle),
\end{aligned}
\qquad \textbf{2.2.0.}
$$

Where up and down arrows represent spin and:

$$a = \frac{1}{\sqrt{x^2+1}},$$

$$b = \frac{x}{\sqrt{x^2+1}}, \qquad \textbf{2.2.1.}$$

$$x = \frac{-(3\Delta_{CR}-\Delta_{SO})+\sqrt{(3\Delta_{CR}-\Delta_{SO})^2+8{\Delta_{SO}}^2}}{2\sqrt{2}\Delta_{SO}},$$

A and B type states could be roughly compared to the ground (heavy) and first excited (light) hole states, respectively, whereas C type –to the split-off state. Considering the spin-orbit coupling, the conduction band state at k=0 is a mixture of s- and p-orbitals and given by:

$$|CB\uparrow\rangle = a\,|S\downarrow\rangle + b\,|Z\downarrow\rangle + c|\,(X+iY)\uparrow\rangle),$$
$$|CB\downarrow\rangle = a\,|S\uparrow\rangle + b\,|Z\uparrow\rangle - c|\,(X+iY)\uparrow\rangle), \qquad \textbf{2.2.2.}$$

where $|S\rangle$ stands for the s-orbital *[Bir 1959; Rod 2001; Rez 2006]*.

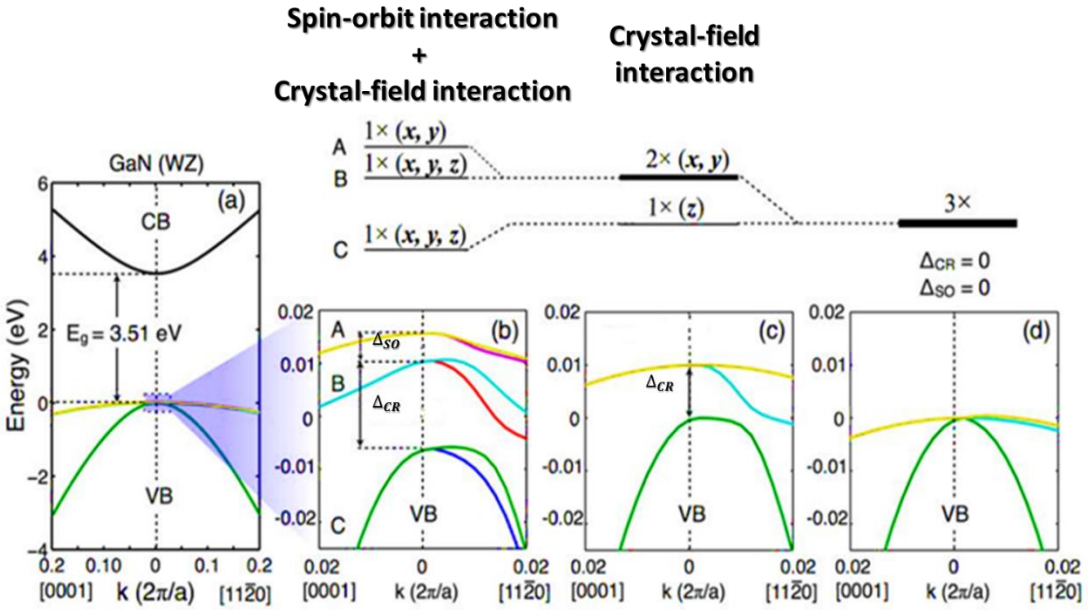

Fig. 2.2.0. The schematics of wurtzite electronic structure with and without spin-orbit and crystal field interactions ***[Aml 2013]****.*

The character of these transitions, i.e. the symmetry of the states involved, determines the polarization of the emitted light.

2.3 STRAIN EFFECT ON THE ELECTRONIC BAND STRUCTURE

The effect of strain results in energy shifts and mixing of energy levels. Moreover, it induces a piezoelectric polarization. In heterostructures the lattice mismatch, as well as difference in

thermal expansion coefficients of different layers cause the in-plane strain. Furthermore, the presence of impurities or native defects can introduce hydrostatic strain. In a more general context, the substrate orientation and the crystal symmetry are the main factors defining the strain tensor.

The Hooke's law sets the relation between the applied stress and resulting deformation of the hexagonal crystal as:

$$\sigma_{ij} = C_{ijkl}\epsilon_{kl}, \qquad \textbf{2.3.0.}$$

where σ_{ij} stands for components of stress tensor, ϵ_{kl} – components of strain tensor and C_{ijkl} are components of elastic stiffness tensor. Throughout this work tensors will be denoted in bold characters, while vectors with an arrow on top. For wurtzite in Voight notation ($xx \to 1, yy \to 2, zz \to 3, yz, zy \to 4, xz, zx \to 5, xy, yx \to 6$) the C_{ijkl} matrix could be written as *[Rom 2006]*:

$$\begin{matrix} C_{11} & C_{12} & C_{13} & 0 & 0 & 0 \\ C_{12} & C_{11} & C_{13} & 0 & 0 & 0 \\ C_{13} & C_{13} & C_{33} & 0 & 0 & 0 \\ 0 & 0 & 0 & C_{44} & 0 & 0 \\ 0 & 0 & 0 & 0 & C_{44} & 0 \\ 0 & 0 & 0 & 0 & 0 & \frac{C_{11}-C_{12}}{2} \end{matrix}, \qquad \textbf{2.3.1}$$

The corresponding values of the stiffness constants are listed in table 2.3.0.

Elastic constants	AlN	GaN	InN
$\boldsymbol{C_{11}}$ **(GPa)**	396	367	223
$\boldsymbol{C_{12}}$ **(GPa)**	137	135	115
$\boldsymbol{C_{13}}$ **(GPa)**	108	103	92
$\boldsymbol{C_{33}}$ **(GPa)**	373	405	224
$\boldsymbol{C_{44}}$ **(GPa)**	116	95	48

*Table 2.3.0. Elastic stiffness constants for AlN, GaN and InN **[Rom 2006]**.*

For the general case of uniaxial and biaxial strain (stress) parallel to the c-axis, preserving the unstrained symmetry group, the strain tensor becomes diagonal with non-vanishing components *[Wag 2002]*:

$$\epsilon_1 = \epsilon_2 = \frac{a-a_0}{a_0}, \qquad \textbf{2.3.2}$$

$$\epsilon_3 = \frac{c-c_0}{c_0}, \qquad \textbf{2.3.3}$$

where c_0 and a_0 are the unstrained lattice constants. The corresponding diagonal stress tensor is:

$$\sigma_1 = \sigma_2 = (C_{11} + C_{12})\epsilon_1 + C_{13}\epsilon_3, \quad \textbf{2.3.4}$$

$$\sigma_3 = 2C_{13}\epsilon_1 + C_{33}\epsilon_3, \quad \textbf{2.3.5}$$

For the case of uniaxial strain perpendicular to the c-axis, there is in-plane elastic relaxation, since external forces in this direction are zero. So the strain and stress tensors will result as *[Wag 2002]*:

$$\epsilon_1 = -\frac{C_{13}}{C_{11}+C_{12}}\epsilon_3,$$

$$\sigma_1 = \sigma_2 = 0, \quad \textbf{2.3.6}$$

$$\sigma_3 = \left(C_{33} + \frac{2C_{13}^2}{C_{11}+C_{12}}\right)\epsilon_3,$$

For biaxial strain perpendicular to the c-axis, there are constant in-plane forces and no force along c-axis *[Wag 2002]* leading to:

$$\epsilon_3 = -\frac{2C_{13}}{C_{33}}\epsilon_1,$$

$$\sigma_3 = 0, \quad \textbf{2.3.7}$$

$$\sigma_1 = \sigma_2 = \left(C_{11} + C_{12} - \frac{2C_{13}^2}{C_{33}}\right)\epsilon_1,$$

In order to have a full understanding of the electronic properties of Nitride-based materials, a careful analysis of the strain effect on the VB structure is indeed required. The compressive biaxial strain in the basal plane modifies the VB structure, but in wurtzite InN and GaN the already existing splitting between the two top VB states (A and B) is not significantly increased, contrary to the zinc-blende arsenides. As a result, A and B type hole states are energetically close to each other *[Win 2007]*. The effect of the same amount of compressive biaxial strain on the valence band structure for wurtzite GaN, InN and zinc-blende GaAs, for comparison *[Win 2007]* is presented in fig. 2.3.0. Furthermore, in nanostructures, the band-edge states show similar behavior along the direction of the strongest confinement.

The biaxial strain results in a shift of the VB. In particular, tensile strain will shift it up leading to an overall decrease of the band gap and the opposite holds for compressive strain (fig. 2.3.1.). Since the energy separation between the A and B levels is initially small, tensile strain can also result in the mixing of them *[Aml 2013; Win 2007]*.

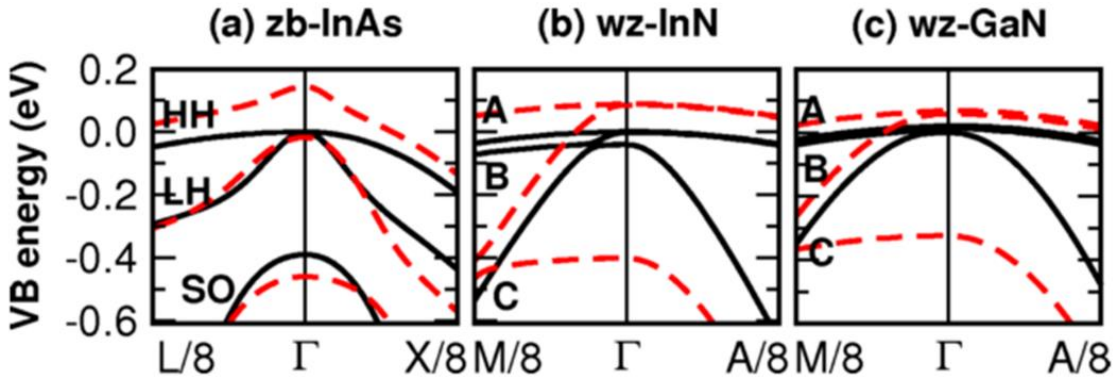

Fig. 2.3.0. Calculated structure of VB for (a) zinc-blende InAs, (b) wurtzite InN, (c) wurtzite GaN materials. Black solid lines correspond to unstrained case, while dashed red ones to biaxial strain in the basal plane. For InN and GaN A point corresponds to $\vec{k} = \frac{\sqrt{2}\pi}{\sqrt{3}a_0}(01\bar{1}0)$ *and M to* $\vec{k} = \frac{\pi}{c_0}(0001)$ ***[Win 2007]***.

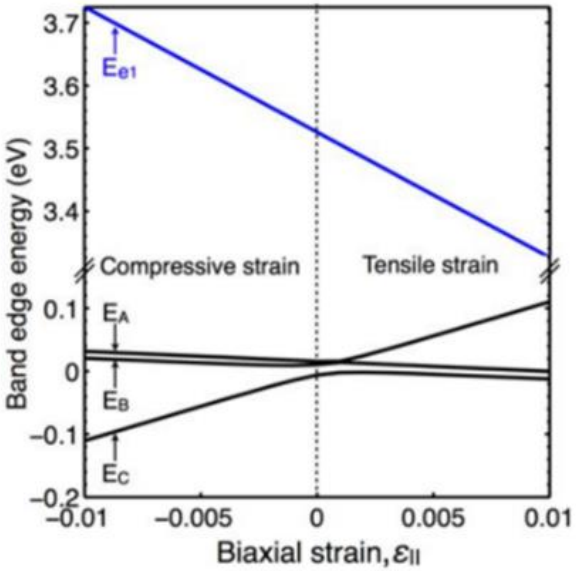

Fig. 2.3.1. GaN band edge energies vs biaxial strain ***[Aml 2013]***.

2.4 THE SPONTANEOUS AND PIEZOELECTRIC POLARIZATION

2.4.1 Spontaneous polarization

The wurtzite crystal structure has a spontaneous polarization, along c-axis, [0001], which results from the relative displacement of the two atomic sub-lattices (change in the internal parameter *u*). There are two possible polarities in the corresponding plane, due to the lack of inversion

symmetry. In fig. 2.4.0. the upper interface (0001) is presented as III-face, while the lower interface $(000\bar{1})$ – as N-face. The spontaneous polarization, P_{SP} is pointed from the Ga- to the N-face.

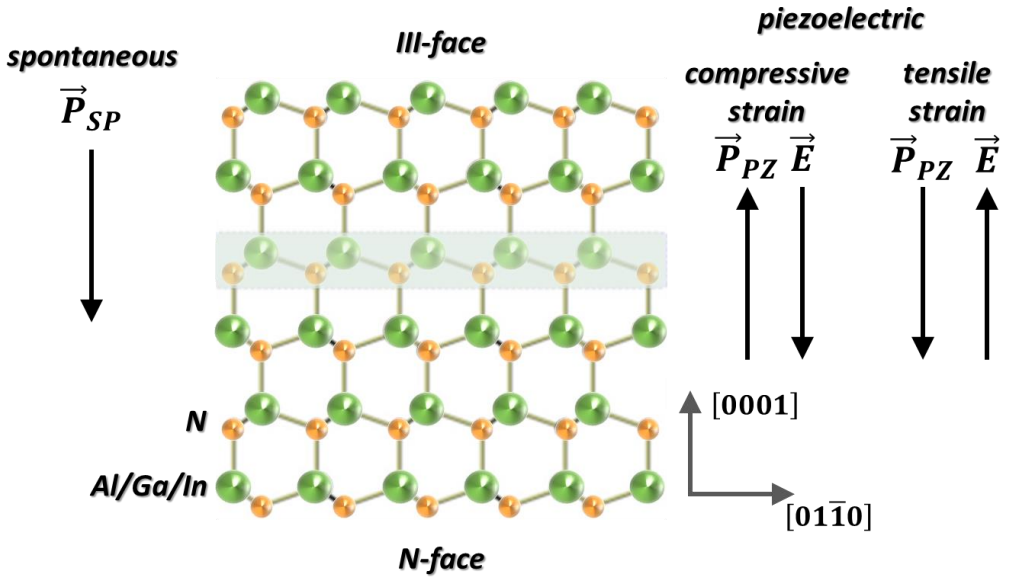

Fig. 2.4.0. Spontaneous and piezoelectric polarization in III-Nitrides crystal.

Typical values reported for III-Nitrides ***[Woo 2008]*** are presented in table 2.4.0.

Materials	GaN	AlN	InN
P_{SP} (C/m²)	-0.034	-0.090	-0.042

*Table 2.4.0. The values of the spontaneous polarization for III-Nitrides **[Woo 2008]**.*

It was also demonstrated, that for ternary alloys the spontaneous polarization cannot be approximated from the corresponding binary compounds using simple Vegard's law. It is necessary to introduce an additional bowing parameter, describing the second order nonlinearity (fig. 2.4.1.). The proposed reason ***[Woo 2008]*** for it is the difference of polarization response to the change of lattice parameter *a* in the corresponding binary compounds.

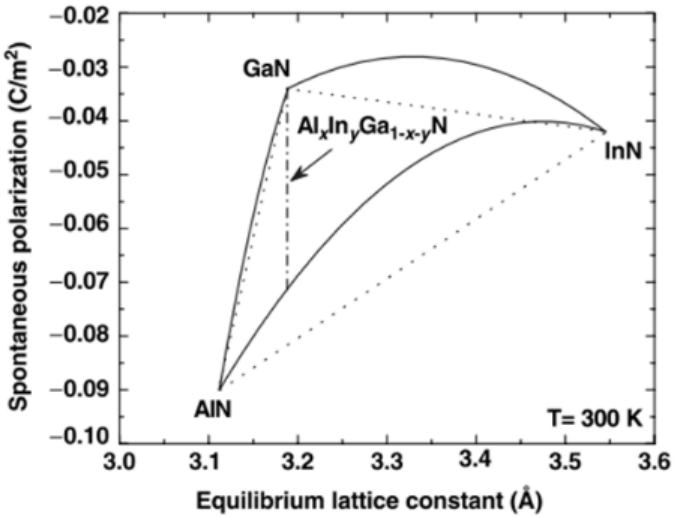

Fig. 2.4.1. Spontaneous polarization as a function of lattice parameter for III-Nitrides at room temperature ***[Woo 2008]****.*

2.4.2 Piezoelectric polarization

Generally semiconductors are grown under strain due to the difference in the crystal lattice with the substrate material. The external stress leads to variations in bond lengths resulting in the piezoelectric polarization (P_{PZ}). The difference between two types of polarization is that P_{PZ} is induced by a mechanical perturbation, while P_{SP} is the intrinsic property of material in its equilibrium state. The sum of the two will give a total built-in polarization, $\vec{P} = \vec{P}_{SP} + \vec{P}_{PZ}$, which represents an electrostatic surface charge at the material surfaces or interfaces. The built-in electric field can be written as $\vec{E} = -\vec{P}/\varepsilon_0\varepsilon_r$, where ε_0 is permittivity of vacuum and ε_r is the static dielectric constant. This built-in electric field was reported to be as much as few tens of MeV/cm^2 for nitride-based structures in the c-direction ***[Ade 2003; Hel 2003]***.

In a general case, piezo-polarization can be expressed as a function of strain as ***[Woo 2008]***:

$$P_{PZ_k} = \sum_l e_{kl}\epsilon_l, \qquad \textbf{2.4.0.}$$

Where ϵ_l and e_{kl} are components of strain and piezoelectric tensor, respectively, whose averaged values are presented in table 2.4.1.:

Hexagonal crystal property	InN	GaN	AlN
e_{31} [C/m^2]	-0.41	-0.34	-0.56
e_{33} [C/m^2]	0.81	0.67	1.53
e_{15} [C/m^2]		-0.26	-0.48

Table 2.4.1. Piezoelectric constants for III-Nitrides ***[Woo 2008]****.*

For the three main cases of strain: biaxial, uniaxial and hydrostatic, it can be rewritten as:

$$P_{biaxial}^{PZ} = 2\epsilon_1\left(e_{31} - e_{33}\frac{C_{13}}{C_{33}}\right),$$

$$P_{uniaxial}^{PZ} = \epsilon_1\frac{C_{11}-C_{12}}{C_{11}-\frac{C_{13}^2}{C_{33}}}\left(e_{31} - e_{33}\frac{C_{13}}{C_{33}}\right), \qquad \textbf{2.4.1.}$$

$$P_{hidrostatic}^{PZ} = \epsilon_1\left(2e_{31} + e_{33}\frac{C_{11}+C_{12}-C_{13}}{C_{33}-C_{13}}\right),$$

Note, that for GaN the piezoelectric polarization is always positive for compression and negative for tension indifferently of the type of the strain: biaxial, uniaxial or hydrostatic (fig. 2.4.2.).

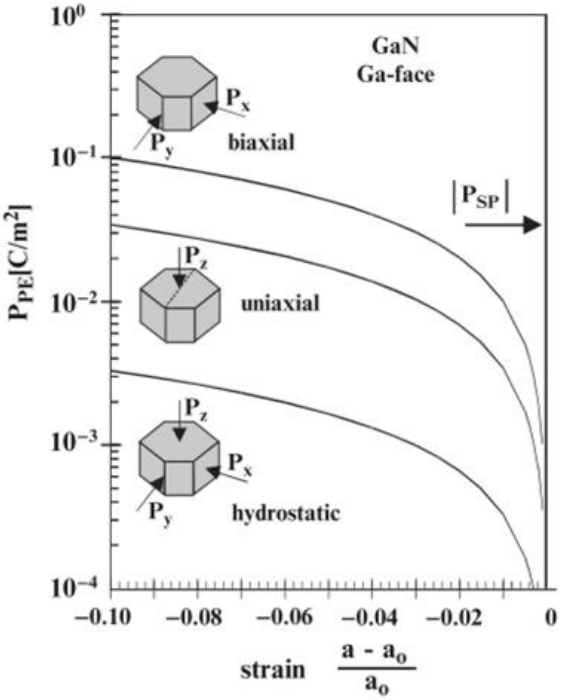

Fig. 2.4.2. Piezoelectric polarization as a function of strain in GaN ***[Woo 2008]****.*

Contrary to the spontaneous polarization case, the piezo-polarization of ternary alloys follows reasonably well Vegard's law (fig. 2.4.3.). Thus P_{PZ} can be written ***[Woo 2008 and Ref where in]*** for case of binary compounds:

$$P_{GaN}^{PZ} = -0.918\epsilon + 9.541\epsilon^2,$$

$$P_{InN}^{PZ} = -1.373\epsilon + 7.559\epsilon^2, \qquad \textbf{2.4.2.}$$

$$P_{AlN}^{PZ} = -1.808\epsilon + 5.624\epsilon^2, \epsilon < 0,$$

$$P_{AlN}^{PZ} = -1.808\epsilon - 7.888\epsilon^2, \epsilon > 0,$$

and for ternary alloys:

$$P^{PZ}_{A_xB_{1-x}N}(x) = xP^{PZ}_{AN}\epsilon(x) + (1-x)P^{PZ}_{BN}\epsilon(x), \qquad \textbf{2.4.3}.$$

where A and B stand for Al, Ga or In and $\epsilon(x)$ is the basal strain for composition *x*.

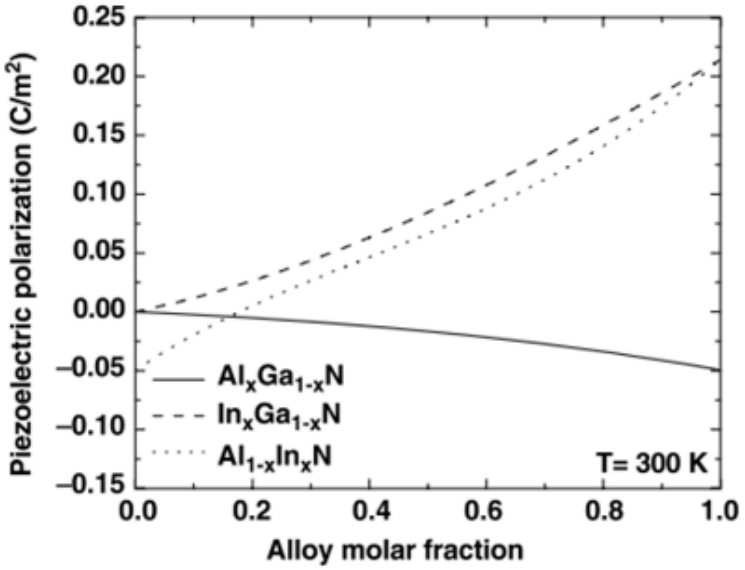

Fig. 2.4.3. Piezoelectric polarization for some ternary compounds as a function of alloy composition x at room temperature ***[Woo 2008]****.*

2.5 OPTICAL PROPERTIES

Over the years, optical spectroscopy was proven to be a reliable tool to obtain a detailed knowledge of semiconductor electronic structure, in particular: energy bands, electronic states associated to structural defects, density of states, recombination lifetimes and so on.

The absorption process is the transition of electrons from the VB to the CB with excess energy, due to photoexcitation. The recombination process, on the contrary, is the process involving electrons decaying from CB to VB while releasing energy in the form of photons (radiative process) or, most generally, phonons (non-radiative process) or exciting other electrons (Auger process).

If both initial and final states are in the same band, the transition is called intraband, otherwise interband transition. The allowed optical transition must obey energy and momentum conservation law and its probability is determined by Fermi golden rule. For the case of absorption of a photon it looks:

$$W_{nm} = \frac{2\pi}{\hbar}\left(\frac{qE_0}{m_0\omega}\right)^2 \left|\langle cn\vec{k}'\left|\vec{e}\hat{\vec{p}}\right|vm\vec{k}\rangle\right|^2 \delta(E_n - E_m - \hbar\omega), \qquad \textbf{2.5.0.}$$

where W_{nm} is a transition probability, m denotes the initial state with energy E_m, n is the final state with energy E_n, q is electron charge with mass m_0, E_0 is the amplitude of incident photon electric field and $\hbar\omega$ is the photon energy.

If the initial or final states are localized at crystal defects, only energy conservation is required, as momentum is not defined for a localized state. In this case, the transition probability is commonly described by the oscillator strength *[Hil 1982]*. For a general case it could be written as:

$$f_{12} = \frac{g_2}{g_1}\frac{2\pi\epsilon_0 mc^3}{w_{21}^2 e^2}A_{21}, \qquad \textbf{2.5.1.}$$

where g_i is the degeneracy factor of the level *i*, w_{21} is the resonance frequency of the transition, $A_{21} = 1/\tau_{spon}$ is the Einstein coefficient for spontaneous emission, ϵ_0 is the free space permittivity.

2.5.1 Excitonic complexes

A photoexcited electron can be bound with the hole left in the VB due to attractive Coulomb interaction, resulting in the formation of a neutral exciton (X). X usually are observed at energies lower than the band gap, by an amount known as the exciton binding energy, E_B^X. There are, generally, two types of excitons in solid state: Wannier-Mott and Frenkel excitons. The radius of a Frenkel exciton is around the value of lattice constant, while for Wannier-Mott excitons it is much larger, of the order of few lattice constants. The latter is usually observed in semiconductors. In three (3D), two (2D) and one-dimensional (1D) structures the average size of X is of the order of the Bohr radius. While for 0D structures, like quantum dots, the confinement potential puts strict constrains on the spatial separation between electron and hole, resulting in the increase of the *e-h* Coulomb attraction and the X binding energy *[Aml 2013; Ram 1998]*.

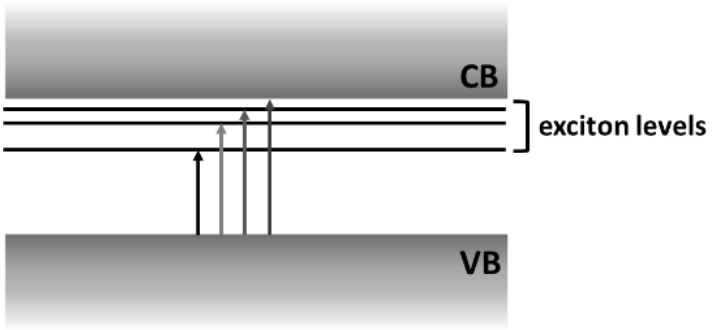

Fig. 2.5.0. Excitonic levels in a semiconductor.

As mentioned, the energy of an exciton is less than that of an unbound electron and hole. It can be described by hydrogen-atom like discrete levels together with the kinetic term *[Ami 2009; Yu 2010]*. Thus the E_B^X can be written as:

$$E_B^X = \frac{R_y}{n^2} - \frac{\hbar^2 k^2}{2(m_h + m_e)}, \qquad \textbf{2.5.2.}$$

where R_y is the effective Rydberg constant, m_h is the hole effective mass, m_e is the electron effective mass and *n* is a positive integer (principal quantum number).

Excitons are unstable complexes and spontaneously recombine producing photons at low temperature. At room temperature the emitted light is usually much weaker or even absent due to non-radiative recombination by the increased phonon population. Also high concentration of carriers can screen the *e-h* interaction, preventing the X formation. The presence of structural defects can cause a broadening of the excitonic lines. In direct (indirect) band gap semiconductors X are referred to as direct (indirect) excitons. In addition to the free excitons, there are also bound excitons, which are formed by binding of free exciton to defects. Such complexes are weakly bounded. Consequently, in the absorption spectra they appear below the free excitons.

Besides the neutral exciton, there can be multi-excitonic complexes, such as trions and neutral or charged biexcitons (XX), etc. They are especially relevant in low dimensional systems, where carrier confinement significantly increases the binding energy. A positive trion (X^+) consists of 2 holes bound to one electron, while a negative trion (X^-) is formed by 2 electrons and 1 hole. A neutral biexciton has two carriers of both species. The energy of the first emitted photon during the XX cascade differs from the second one by the biexciton binding energy (E_b^{XX}), which results from the extra Coulomb interaction produced by the second *e-h* pair.

2.6 PHOTON CORRELATION

The degree of coherence of light is generally described by the normalized first-order correlation function ***[Ger 2005]***:

$$g^{(1)}(z_1, t_1, z_2, t_2) = \frac{\langle E^*(z_1,t_1)E(z_2,t_2)\rangle}{\sqrt{\langle|E(z_1,t_1)|^2\rangle\langle|E(z_2,t_2)|^2\rangle}}, \qquad \textbf{2.6.0.}$$

where $E(z_i, t_i)$ is the complex electric field amplitude, measured at time t_i at a point z_i in space. For the case of statistically stationary fields, the correlation function only depends on the time difference between two detections: $\tau = t_2 - t_1 - \frac{z_2 - z_1}{c}$. Hence the stationary light fields can be classified by their degree of first-order optical coherence into three groups:

I. completely coherent (first-order coherent), if $\left|g^{(1)}(\tau)\right| = 1$,
II. completely incoherent, if $\left|g^{(1)}(\tau)\right| = 0$,
III. partially coherent, if $0 < \left|g^{(1)}(\tau)\right| < 1$.

Natural light emission (or thermal light) is produced by a sequence of decays from randomly excited atoms in the source. The emitted wave trains will exist during a characteristic time τ_c (coherence time), and have a characteristic length $l_c = c\tau_c$ (coherence length). From its definition $g^{(1)}(0) = 1$ and light remains nearly coherent for delay times $\tau \ll \tau_c$, while for $\tau \gg$

τ_c $g^{(1)}(\tau) \to 0$ *[Lou 1983]*. This is only valid for thermal light, where no fixed phase relation between emission events exist (e.g. light from a bulb). In turn deterministic light, (e.g. ideal laser light) is first-order coherent at any space-time point ($g^{(1)}(\tau) = 1$ at any τ). The physical meaning of $g^{(1)}$ can be easily understood in terms of Young's type interference pattern. The visibility of the interference fringes is directly proportional to $g^{(1)}$ *[Scu 1997]*.

So the first-order correlation function allows to determine the coherence length and time, or in the other words to which degree light is monochromatic. But the statistical nature of the light source yet cannot be distinguished. Whether two beams are coming from two independent sources or from the same one is unknown, as long as they have equal spectral properties. Thus it is necessary to introduce the second-order correlation function, also known as intensity-intensity correlation function.

One of the first experimental techniques employed for this purpose was Hanbury Brown and Twiss (HBT) interferometry, developed in 1950s *[Bro 1956]*. It focuses on the correlation of intensities rather than fields and measures the photon coincidence rate as a function of delay. If the time delay is less than the coherence time, then the statistical information of the light beam is revealed. The coincidence rate is proportional to the averaged intensity of the collected signal *[Ger 2005]*:

$$C(t, t+\tau) = \langle I(t) I(t+\tau) \rangle, \qquad \textbf{2.6.1.}$$

where $I(t)$ and $I(t+\tau)$ are measured instantaneous intensities and angular brackets mean time averaging. Assuming a stationary field, one can obtain the normalized probability to detect a coincidence as:

$$g^{(2)}(z_1, t_1, z_2, t_2) = \frac{\langle I(z_1,t_1) I(z_2,t_2) \rangle}{\langle I(z_1,t_1) \rangle \langle I(z_2,t_2) \rangle} == \frac{\langle E^*(z_1,t_1) E^*(z_2,t_2) E(z_2,t_2) E(z_1,t_1) \rangle}{\langle |E(z_1,t_1)|^2 \rangle \langle |E(z_2,t_2)|^2 \rangle}, \qquad \textbf{2.6.2.}$$

That is a classical definition of the second-order correlation function. It represents the joint probability of detecting one photon at time t_1 at position z_1 and another at time t_2 at position z_2. For a stationary field and fixed spatial position, $g^{(2)}$ is again only dependent on the time difference: $\tau = t_2 - t_1$. Note, that contrary to the first-order correlation function, $g^{(2)}$ has a broader range: $0 \leq g^{(2)}(\tau) < \infty$. For thermal light the relation between the two correlation functions is: $g^{(2)}(\tau) = 1 + \left| g^{(1)}(\tau) \right|^2$. By substituting the limit values of $g^{(1)}$ one obtains following limits for $g^{(2)}$: $g^{(2)}(0) = 2$ (case of super-Poissonian distribution (fig. 2.6.0.(a)) and $g^{(2)}(\tau) \to 1$ for $\tau \gg \tau_c$. For a deterministic wave source $g^{(2)}(\tau) = 1$ independently of the value of τ (case of Poissonian distribution (fig. 2.6.0.(b)).

The quantum theory of light gives a similar description of the second-order correlation function, but instead of intensities one uses the photon number *n*:

$$g^{(2)}(\tau) = \frac{\langle n(n-1)\rangle}{\langle n\rangle^2}, \qquad \textbf{2.6.3.}$$

Consequently, for chaotic light (i.e. thermal emission) $g^{(2)}(0) > g^{(2)}(\tau)$, meaning that the probability of detecting a second photon after delay time τ decreases. So photons tend to group rather than being randomly distributed. Such effect is called "photon bunching" (fig. 2.6.0.(a)). In fact, for all classical light sources the second-order correlation function cannot exceed its value at zero time delay *[Lou 1983; Pau 1982]*. On the contrary, when $g^{(2)}(0) < g^{(2)}(\tau)$, the situation is reversed and such effect is called "photon antibunching" (fig. 2.6.0.(c)). This is a purely non-classical effect and can be described only by means of the quantum theory of light. Thus the second-order correlation function plays a crucial role in determination of the quantum nature of a light source.

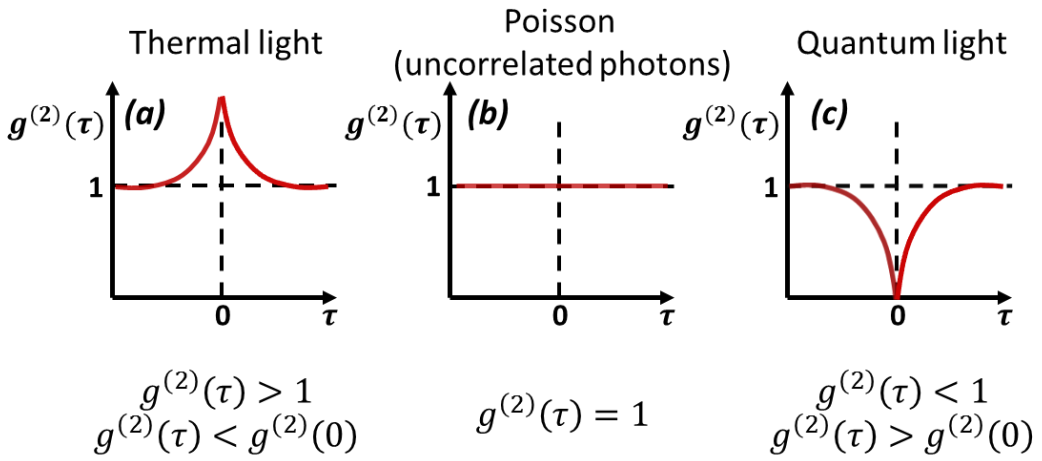

Fig. 2.6.0. Examples of light statistics for (a) thermal light, (b) uncorrelated photons and (c) quantum light.

The key difference between the classical and quantum descriptions lies in the $g^{(2)}$ numerators. In HBT experiments the measured quantity is a light intensity (classical theory) or a photon number (quantum theory). In the first case the intensity value is unchanged after the first detection, while in the second case there are $n-1$ photons left after the first detection. Thus in the quantum description two distinct ranges are observed for $g^{(2)}(0)$:

$$g^{(2)}(0) = \begin{cases} 0 \; if \; n = 0,1 \\ 1 - \frac{1}{n} \; if \; n \geq 2 \end{cases} \qquad \textbf{2.6.4.}$$

So $g^{(2)}(0) < 1$ (sub-Poissonian distribution) and for an ideal single photon source (SPS) $g^{(2)}(0) = 0$ (fig. 2.6.0.(c)), while for the case of two independent photons $g^{(2)}(0) = 0.5$. In a real experiment, though, there can be deviations from these values due to the contribution of the background emission or instrumental imperfections. Generally an experimental correlation function for a SPS is well described by (cw excitation) *[Rei 2008]*:

$$g^{(2)}(\tau) = 1 - \beta e^{-\frac{|\tau|}{\tau_R}}, \qquad \textbf{2.6.5.}$$

where β accounts for the SPS performance and τ_R is the antibunching time (width of the antibunching dip).

2.7 III-NITRIDES NANOSTRUCTURES

III-Nitride semiconductors have proven to have a great deal of applications in various fields, ranging from solid state lighting to high power/high speed electronics. All that became possible because of the unique combination of their basic properties: wide range of bandgaps, strong piezoelectricity and high saturation velocities. Notwithstanding the importance of bulk layers, the low dimensional structures (quantum wells, wires and dots) open the possibility to further improve device characteristics due to increased localization of *e-h* pairs followed by increased probability of their radiative recombination rate (allowing for high speed operation) and increase of binding energy in the excitonic complexes (allowing for high temperature operation).

2.7.1 Nanowires

The interest for arrays of nitride-based nanowires (NWs) burst out in 90s when several groups reported on successful realization of self-assembled (SA) arrays of NWs ***[San 1998; Yos 1997; Hoo 1995]***. One of the advantages of the wire geometry is the high crystalline quality and uniformity for relatively large sample volumes. This is especially important for InGaN alloys, where the problem of structural uniformity is a great issue in bulk materials ***[Kuy 2007]***. The formation of vast chains of threading dislocations due to the lattice mismatch between nitride bulk layer and commercially available substrates usually manifested itself in the PL spectra as a broad band emission below the band gap, commonly referred to as yellow band. Changing to 1D NW geometry results in complete suppression of the yellow band, and significant increase of the near band gap emission. Typically reported values of near band gap emission from NWs is 2 to 4 orders of magnitude more intense than from bulk ***[Gac 2015]***. A considerable enhancement of emission from wires makes them more attractive to optoelectronic applications.

Another important advantage of NWs is a significant reduction of strain due to higher surface-to-volume ratio. Substrate induced effects are removed, thus expanding the choice of substrates ***[Cal 2000; Kuy 2007; Ase 2016]***. The latter is of paramount importance due to the lack of commercially available and cheap substrates compatible with the realization of high quality III-Nitrides.

However, control over the SA arrays structural properties (location, size and shape) is limited. It is worth noting that since most of SA arrays are heteroepitaxially grown (i.e. on Si substrates), the additional randomness of tilt and twist of NWs can produce edge dislocations, followed by degradation of the material quality ***[Gac 2015]***. These problems were overcome by employing various homoepitaxial selective area growth (SAG) techniques. This allows to achieve a high

uniformity in size/shape as well as to determine a precise spatial location. Homoepitaxy results in a significantly improved control of wires orientation. Further, embedding quantum wells (QWs) and quantum dots (QDs) into NWs and combining their properties opens interesting opportunities not only for solid state lighting but also for quantum communications and information processing. The relatively easy transfer of such structures from native substrates facilitates their integration with already existing components for on-chip technologies. Moreover, 1D geometry is a promising alternative to the planar technology, as it allows to produce novel architectures, resulting in the increase of device density. Recently, ordered arrays of InGaN/GaN light emitting diodes (LED) were reported *[Sek 2010]*. These authors were able to achieve wavelength tunability on one substrate by varying the wire diameter through a Ti mask. The use of SAG NW was also successfully demonstrated for the realization of field effect transistors *[Gac 2016; Mot 2007; Hua 2002]*.

2.7.2 Quantum dots

A quantum dot (QD) is a structure, in which carriers are confined in all three directions. Owing to the 3D confinement, the energy levels become discrete. Due to this specific property QDs are frequently referred to as artificial atoms. In semiconductors, QDs are formed by two materials A and B, where $E_g^A > E_g^B$ and B is fully surrounded by A. There are generally three types of QDs (fig. 2.7.0.), referring to their band alignment, which is also valid for 2D and 1D systems. In type I (GaAs/AlAs; GaN/AlN) both electrons and holes are confined in B because both the CB minimum and the VB maximum are located in B. In type II (AlAs/AlSb), only one type of charges; either electrons, or holes, is confined in B, while the other one is delocalized in the barrier, material A. And finally type III (InAs/GaSb), sometimes referred as subcase of type II, also called as zero band gap structure because the CB of material B is lower than the VB of material A, as in semimetals. In this case electrons or holes enter directly from the barrier into the QD.

In addition to the confining potential due to the different gaps, in nitride QDs also the piezoelectric field plays an important role. Theoretical models *[Win 2006]* have shown that the total built-in potential for InGaN/GaN QDs is dominated by the piezoelectric potential, since the small difference in the spontaneous polarization constants of InN and GaN weaken the spontaneous component. It also does not change the symmetry of the structure in the basal plane. Instead, for GaN/AlN QDs the built-in potentials, resulting from both spontaneous and piezoelectric polarization, has been found of the same order of magnitude *[And 2000]*. It was shown that in nitride-based systems the total built-in polarization produces modifications to the confinement potential of the same order of magnitude as a band offset between the different materials, which is contrary to the As-based systems *[Win 2006]*. In fig. 2.7.1. (a-b) the band edge profile along the *z* direction around the center of InGaN QD with and without spontaneous and piezoelectric effects is presented.

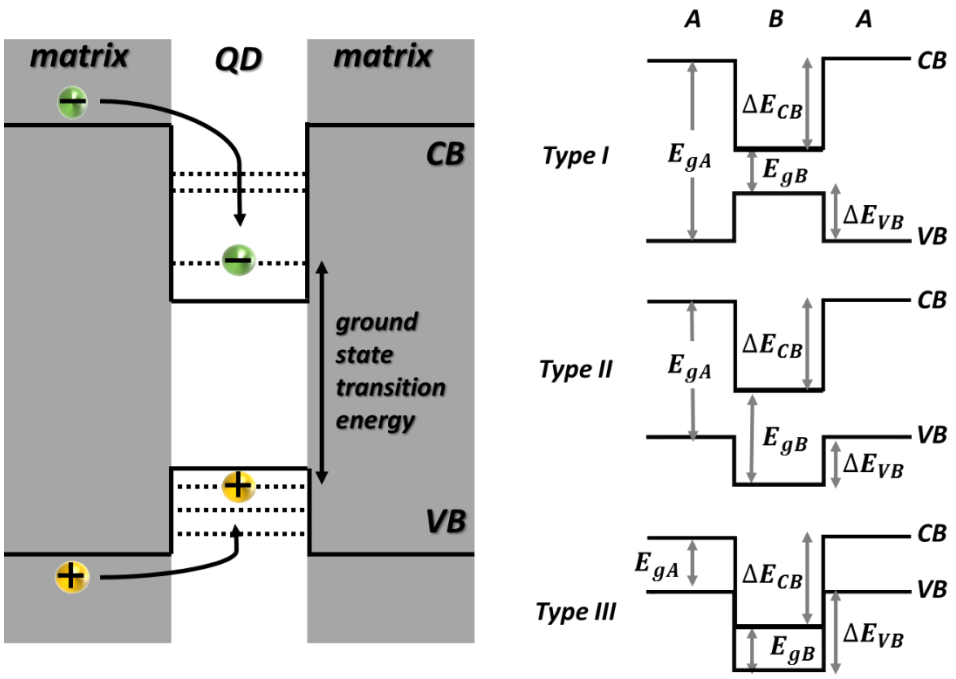

Fig. 2.7.0. On the left: a simplified schematics of a QD band structure. On the right: the three most common types of e-h confinements in semiconductor heterostructures formed by materials A and B.

For the case of no built-in potential, the band edge profile is rather symmetric along the QD center as expected and produces confinement for both types of charges. The biaxial strain due to lattice mismatch doesn't split A and B energy levels and shifts C level. Thus first two hole levels should be of type A, B or their combination. Once the total built-in potential is included, a spatial separation of electrons and holes occurs followed by a strong mixing of the three hole energy levels. Now the holes are confined in the lower part of the QD, while electrons are in the upper part of the QD *[Win 2008]*. The resulting red shift of the emission energy (fig. 2.7.1.c-d) is the well-known Quantum Confined Stark Effect (QCSE).

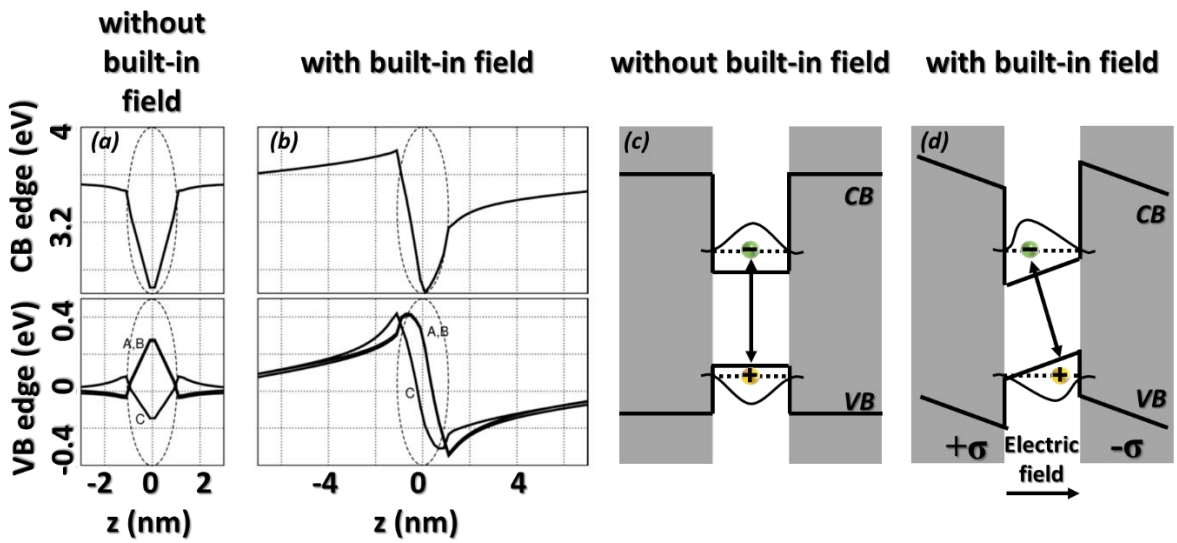

Fig. 2.7.1. The band edge profile for InGaN QD without (a) and with (b) built-in electric potential. The dashed circle determines the QD position ***[Win 2006]****. (c)-(d)The red shift of the emission energy due to the built-in potential, QCSE.*

In nitride QDs the splitting between the two first hole levels (A, B) has been reported to be of the order of 10 meV and seems to be only dependent on crystal-field and split-off energies. Instead, the splitting between first and second excited hole states is QD shape dependent and of the order of few tens of meV ***[Win 2008]***. The schematics of bulk-wurtzite valence band structure without and with biaxial strain is presented on the fig. 2.7.2.(a)

The effect of strain and its symmetry on the VB structure is evident. In particular, the strain (or shape) anisotropy drastically changes the polarization of the X emission, from circular to linear (fig. 2.7.2.(b)). Several research groups have shown that transitions between the electron ground state and the first two holes states have substantial oscillator strengths, so even a small structural anisotropy leads to pronounced polarization in orthogonal directions ***[Win 2007; Aml 2012]***. Also lowering the in-plane anisotropy results in the decrease of the polarization degree ***[Win 2007]***. The effect of in-plane elongation of wurtzite nitrides-based QDs is indeed very dramatic as shown on fig. 2.7.3.

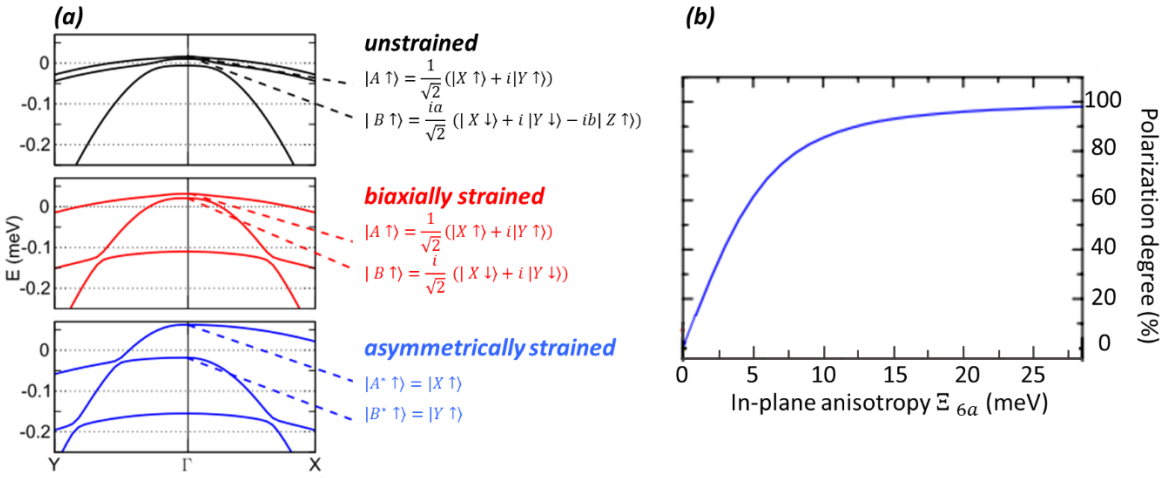

*Fig. 2.7.2. (a) Wurtzite valence band structure for unstrained case (black), applied biaxial strain (red) and asymmetrically strained case (blue) **[Win 2008]**.(b) Polarization degree as a function of in-plane anisotropy **[Bar 2008]**.*

Thus even small external electric and/or strain fields can change the polarization of X emission. This is a useful property since it enables a dynamic control of emission polarization by external stress **[Aml1 2013]**.

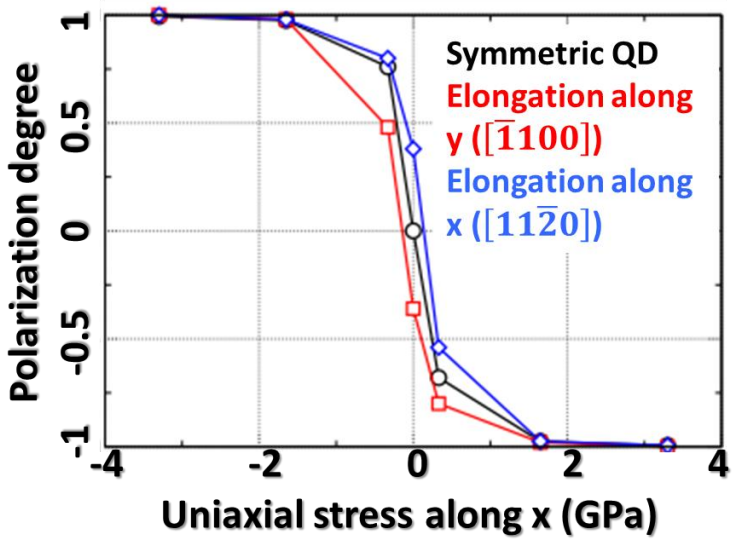

*Fig. 2.7.3. Polarization degree of the light emitted by a QD as a function of uniaxial strain along different directions **[Win 2008]**.*

Bardoux and co-workers proposed a theoretical model, claiming that the key parameter for controlling the polarization degree in Nitride-based QDs is the ratio between the in-plane anisotropy and the in-plane part of the spin-orbit splitting, (which mostly accounts for the splitting between the first two valence bands) **[Bar 2008]**.

One of the general consequences of the asymmetric exchange Coulomb interaction in QD is the appearance of a splitting of the (otherwise degenerate) fundamental exciton transition. Such splitting is called fine structure splitting (FSS). In wurtzite QDs, following Amloy's notation there are two types of excitons in symmetric QDs: type 1 corresponds to the A-hole band. It has two optically allowed transitions with in-plane polarization, perpendicular to the c-axis. Type 2 corresponds to B and C hole bands and presents three exciton states: two are optically active and one dark (fig. 2.7.4.). Out of the optically active transitions, one is polarized in the *xy* plane and one – vertically ***[Aml 2011]***. In asymmetric QDs the exciton level structure is more complicated (right panel in fig. 2.7.4.) as a result of the degeneracy lifting by the symmetry lowering. There are reports of FSS in GaN/AlN QDs in the order of few meV for transitions polarized in all three directions ***[Kin 2010]***, while for InGaN QDs FSS was resolved only for z-polarized transitions and no in-plane splitting was detected ***[Aml 2011]***. The lack of FSS in the fundamental exciton transition in InGaN QDs is the consequence of the anisotropy-induced VB mixing, and is reflected by high degree of linear polarization mentioned above.

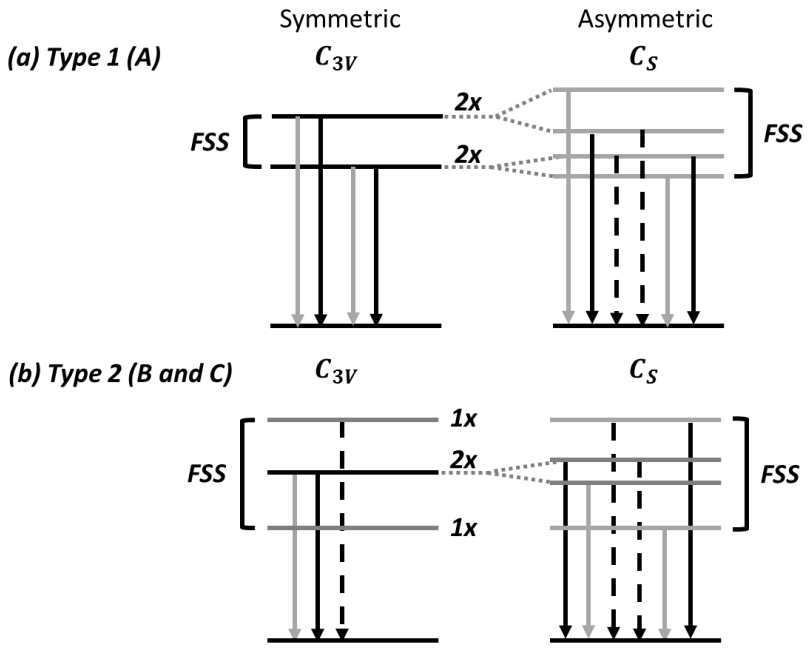

Fig. 2.7.4. The schematics of (a) type 1, A exciton, and (b) type 2, B and C excitons for symmetric (left panel) and asymmetric (right panel) wurtzite QDs. Grey arrows indicate x-polarized, black – y-polarized and dashed – z-polarized transitions ***[Aml 2011]****.*

The 3D confinement favors the formation of excitonic complexes (biexcitons) by increasing their binding energy (fig. 2.7.5.). Several research groups studied the possibility to control the binding energies by controlling the QD size and shape ***[Ram 1998; Aml 2011; Aml 2014]***. The simplest way to describe the biexciton binding energy ***[Aml 2011 and Ref wherein]*** is

$$E_b^{XX} = 2J_{eh} - J_{ee} - J_{hh}, \qquad \textbf{2.7.0.}$$

where J_{eh} is the *e-h* Coulomb attraction, J_{ee} and J_{hh} are *e-e* and *h-h* Coulomb repulsions, respectively. In a 0D structure the XX binding energy can be either positive or negative due to the strong 3D confinement, contrary to 1-3D structures. In the latter cases, biexcition with $E_b^{XX} < 0$ would not form a bound state.

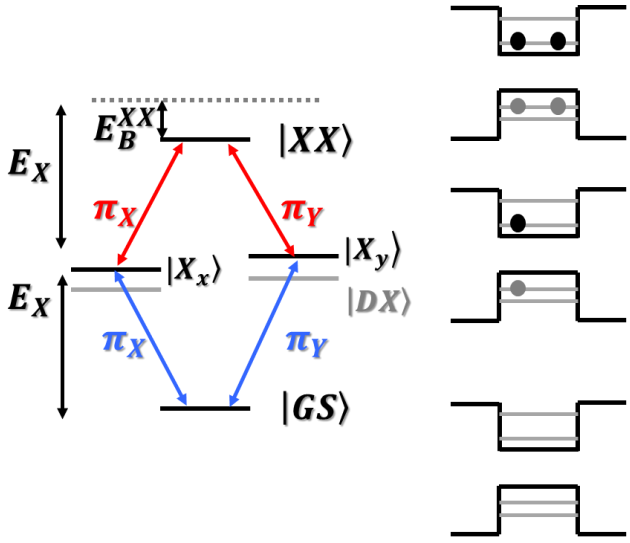

Fig. 2.7.5. A schematics of X and XX levels in QD.

2.8 FABRICATION

QDs can be synthesized by sophisticated growth techniques (III-N, III-As) or by colloidal methods (CdSe *[Lea 2002]*). Out of various deposition techniques, epitaxial growth gives better structural quality as well as better ability to control QD size, shape and position. The two mainly competing technologies are Metal-Organic-Chemical-Vapor Deposition (MOCVD) and Molecular Beam Epitaxy (MBE). The first one works at high growth temperatures, which results in relatively poor crystalline quality for In based compounds, while the other one produces best material quality but is quite inefficient for thick structures due to relatively low growth rates. Nevertheless both techniques are employed in the successful fabrication of various QD structures.

The first epitaxial grown arrays of QDs were achieved by self-assembled nucleation, resulting in the random distribution of both size and shape as well as the spatial localization on the substrate.

Recently, dictated by industrial necessity, the growth of ordered arrays has gained significant progress. The main fabrication strategies are (i) top-down or (ii) bottom-up methods. The choice of the method is strongly dependent on the desired application. In the (i) case posterior techniques are used to define a QD structure from the extended (bulk) layers. The most common method makes use of lithographically designed masks followed by etching. Different shapes and patterns can be achieved in controllable manner like, for example, pyramids *[Zha 2013]*, rings *[For 1996]* or nanowires *[Zha 2016]*. The controllability of size/shape could be easily achieved by the mask

orientation as well as the etchant type. Most etchants act only in specific crystallographic directions thus allowing to a precise control of the process. Being historically first, top-down methods have some advantages for precise size/shape control, but also there are some fundamental limitations in the size due to the mask size limitations.

The bottom-up method uses epitaxial growth with varying growth parameters, which allows to form nearly defect free QDs. The most commonly used growth mode is Stranski-Krastanow (SK). In this mode the layer is growing under stress due to the lattice mismatch with the substrate material. Once reaching critical thickness it becomes energetically favorable to form islands on top of wetting layer. The Volmer-Weber (VW) growth mode is a variant of SK, which activates when the difference between the lattice parameters of the substrate and the growing layer is significantly large, so the island nucleation starts immediately without forming wetting layer. However, the spatial control for bottom-up methods is mostly achieved via different masks patterned on the substrate prior to the growth, in order to determine the QD nucleation sites.

There are several reports on vertically ordered arrays of QDs *[Mul 2013; Lev 2011; Wan 2004; Ara 2002]* showing the possibility to control QD position through vertical alignment. The samples generally consist of two or more layers of QDs separated by a spacer (a layer of a different material, normally same as the barrier). Depending on the thickness of the spacer, QDs are either correlated for relatively thin spacer or anticorrelated for thick separation layers *[Wan 2004]*. In this method no additional patterning of the substrate was needed but the lateral control is somehow still difficult.

Another way to control the spatial localization of QDs is to use vicinal (intentionally misoriented) substrates. It was reported that the morphology of a growing layer of QDs was adapted to the one of the substrate, resulting in ordered chain-arrays of quite uniform QDs along the preferential step edge of the wafers *[Hub 2013; Pos 2003; Zha 2003]*. A certain degree of size/shape control was also achieved via this method *[Pos 2003 and Ref wherein]*.

Patterning of the substrate together with the carefully chosen growth parameters could result in perfectly ordered QD arrays with well controlled size. The SAG technique was achieved by different ways: optical or electron-beam lithography combined with etching *[Tat 2000; Mar 2005; Hsu 2011; Ara 2002]*. The preferential growth takes place in the mask's holes, while almost nothing was growing on the mask itself. An interesting perspective of SAG is to embed QDs into ordered arrays of nanowires *[Hol 2014; Alb 2012]* and pyramids *[Hsu 2011, Ara 2002]*. In this approach, arrays of 1D structures were achieved by electron-beam or colloidal lithography. Such structures open a possibility to combine their properties as well as facilitate their posterior integration with other on-chip components for already existing photonic and optoelectronic devices.

2.9 SURFACE ACOUSTIC WAVES

In late 19th century the Curie brothers discovered that applying an external force produces a surface charge distribution in some materials like quartz. On the other hand, applying an electric field results in the mechanical deformation of the material. This effect was called a piezoelectric effect. Further investigations determined that it is possible only in anisotropic materials, with spontaneous polarization. If the initial charge equilibrium is broken by an external mechanical force, the created internal electric field will redistribute positive and negative charges inside the material to restore equilibrium. This field can be detected as a voltage on external electrodes. An external voltage applied across the material, in turn, will cause the crystal to shrink or expand, corresponding to the mechanical strain: compressive and tensile, respectively. If the applied voltage is periodic in time, a mechanical wave propagating near the surface will be produced. This type of wave is known as a Rayleigh wave *[Ray 1885]* and often referred to as surface acoustic wave (SAW).

Almost a century later, in 1965, a renewed interest in SAW field was burst out with the invention of interdigital transducers (IDTs) by Voltmer and White *[Whi 1965]*, as an efficient technique for generation and detection of acoustic waves in piezoelectric materials. Novel and promising applications in solid state electronics, like electrical filters and sensors operating up to GHz frequencies, became possible. Furthermore, it opened a possibility to modulate the electronic, optical and mechanical properties of low dimensional semiconductor structures.

In the following sections a more detailed description of SAW-related phenomena will be given together with common generation and detection techniques and recent application achievements.

2.9.1 Description of surface acoustic waves

Motion in elastic materials in general is described by the wave equitation:

$$\vec{\nabla}\boldsymbol{\sigma} = \rho\frac{\partial^2\vec{u}}{\partial t^2}, \qquad \textbf{2.9.0}$$

where $\boldsymbol{\sigma}$ is the stress tensor, ρ is the material density, and $\vec{u}$ is the displacement. In piezoelectric materials Hook's law is modified as:

$$\begin{aligned}\boldsymbol{\sigma} &= \boldsymbol{C\epsilon} - \boldsymbol{e}\vec{F},\\ \vec{D} &= \boldsymbol{e\epsilon} + \boldsymbol{\varepsilon}\vec{F},\end{aligned} \qquad \textbf{2.9.1.}$$

where $\boldsymbol{\epsilon}$ is the strain tensor, $\vec{F} = -\vec{\nabla}\Phi_{SAW}$ is the piezoelectric field, expressed in terms of the piezoelectric potential Φ_{SAW}, $\boldsymbol{C}$ is the elastic stiffness tensor, $\boldsymbol{e}$ is the piezoelectric tensor, $\vec{D}$ is the electric displacement field and $\boldsymbol{\varepsilon}$ is the static dielectric tensor. As followed from these formulas, mechanical waves in piezoelectric materials are accompanied by electrical ones. The general

solution for a given propagation direction includes three independent bulk elastic modes with angular frequency (w_i), phase velocity ($\overrightarrow{v_i}$) and wave vector ($\overrightarrow{q_i}$) satisfying the condition: $w_i = \overrightarrow{v_i} \cdot \overrightarrow{q_i}$, where $i = 1,2,3$. Out of those, two modes exhibit particle displacement in approximately transverse direction and are called quasi-transverse (qTA) modes, while the third one produces displacement nearly along the propagation direction and, correspondingly, is called quasi-longitudinal (qLA) mode. Phase velocities are determined by the square root of the ratio between elastic stiffness constants and mass density of a given material. Since this section is focused on a specific type of waves we will proceed only with the detailed description of plane waves confined near the surface. So stress and electromagnetic boundary conditions must be satisfied:

$$\begin{aligned} \sigma_{yj}(y = 0^-) &= \sigma_{yj}(y = 0^+), \\ D_y(y = 0^-) &= D_y(y = 0^+), \end{aligned} \qquad \textbf{2.9.2}$$

where the plane y=0 defines the surface of the material, and (+) and (-) refer to regions above and below it, respectively. The propagation of SAWs is associated with two motion components: transverse and longitudinal, oscillating out of phase. Moreover, the displacement normal to the surface is larger than the one along the propagation direction. The energy profile of surface acoustic waves is proportional to $e^{-2\pi\frac{y}{\lambda}}$, where *y* is the depth and λ is the acoustic wavelength. Consequently, the SAWs amplitude is considerably reduced at the depth$\sim \lambda$, while attenuation along the surface is rather small and varies as $\sim\frac{1}{\sqrt{r}}$ (*r* is in-plane radial distance). Although SAWs can propagate in any direction, for certain applications a careful choice of the crystallographic orientation is indeed required. Most commonly used orientations are the ones which have a strongest piezoelectric coupling.

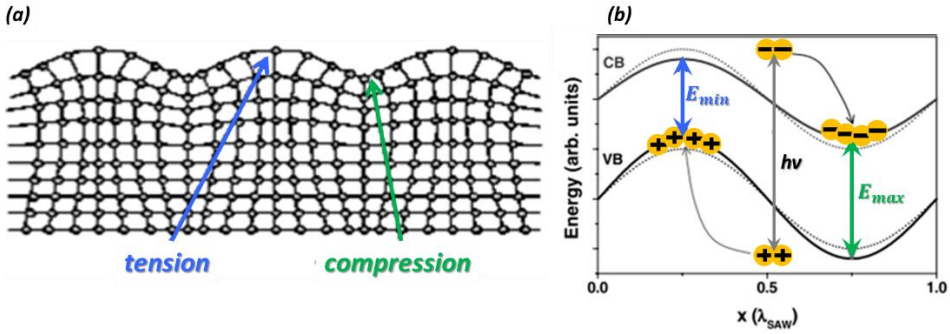

Fig. 2.9.0. A schematics of SAW induced local volume variation (a) and modulation of energy band gap ***[Lim 2005]*** *(b).*

SAWs strain field induce a type I modulation of the electronic transitions, oscillator strength and refractive index. Due to local volume variations, the energy band gap varies from its minimum (E_{gmin}) to maximum (E_{gmax}) values (fig. 2.9.0.(b)), corresponding to regions of maximum tension and compression (fig. 2.9.0.(a)), respectively. In piezoelectric materials, apart of the strain field, SAWs also produce a piezoelectric field. The later causes a sinusoidal modulation of the energy

bands (fig. 2.9.0.(b) dashed lines). The combination of the two (piezoelectric and strain fields) allows the possibility for an effective dynamic control of semiconductor's optical properties.

2.9.2 Interdigital transducer for generation of surface acoustic wave

The typical SAW device consists of a piezoelectric substrate and a pair of electrodes (input and output), interdigital transducers (IDTs). More sophisticated devices could also contain more than one pair of IDTs in order to be able to control the SAW propagation directions and its spatial profile. The space between IDTs, along the SAW path, is called a delay line (fig. 2.9.1.(a)).

Typical IDT design consists of metal fingers periodically aligned and connected to a bus-bar (fig. 2.9.1.(b-d)). The shape and periodicity of the IDT fingers are strongly dependent on the intended applications. For SAW excitation a sinusoidal electrical signal, of radio frequency (RF), is applied to the IDTs, creating the regions with alternating electric fields between the fingers. According to the piezoelectric effect this fields will create regions of tension and compression, which will propagate as a mechanical wave in both directions from the input IDT. In some devices an absorber or reflector is placed between the electrodes and the edge of the substrate to reduce insertion losses. Once the mechanical wave reaches the second IDT, it creates an alternating electric field, which could be detected as the output signal. Comparison of input and output signals characterizes the SAW coupling with the propagation medium. The length of the metal fingers determines the width of the SAW propagation region and IDTs electrical impedance. The latter is usually matched to the impedance of conventional RF sources.

One of the simplest type of IDTs is a single-finger IDTs (fig. 2.9.1.(b)). Its period consists of 2 fingers, connected to opposite bus-bars. Once created, the SAW propagates through the IDTs metal grid and partially reflects and scatters to the bulk modes. These losses are especially pronounced if the gap between fingers and its width are equal to $\lambda_{SAW}/_4$, because it leads to the constructive sum of all reflections. The losses also increase with the acoustic frequency and power and lead to essential limits of the allowed RF powers on IDTs. Thus the single-finger design is usually replaced by double-finger or split finger (fig. 2.9.1.(d)) one in order to reduce such losses. This configuration is achieved by splitting fingers into two, so the grating period would consist of four fingers: where the first two fingers are connected to one bus-bar and the second two to the other. Although, this design significantly reduces back reflections, it is also limited by lithographically achievable widths of the metal stripes, since for generation of acoustic beams of the same frequency it needs twice as narrow fingers as for single-finger IDTs. The fundamental frequency in this case is doubled. For some applications strong acoustic beams are required. Since the RF voltage, applied to the IDT is limited, an alternative solutions are required ***[Lim 2003; Gre 1980; Wil 1985]***. The most commonly used is focusing IDTs (fig. 2.9.1.(c)), which produce strong acoustic beams concentrated on small areas. Alternative designs to reduce reflection losses can be found in Refs ***[Lim 2004; Has 2000]***.

The IDTs manufacture is done by standard microfabrication techniques: optical or electron-beam lithography. The choice of technique is dictated by the desired resolution and cost. Moreover, to achieve the required SAW frequencies the lithography precision and accuracy must be high.

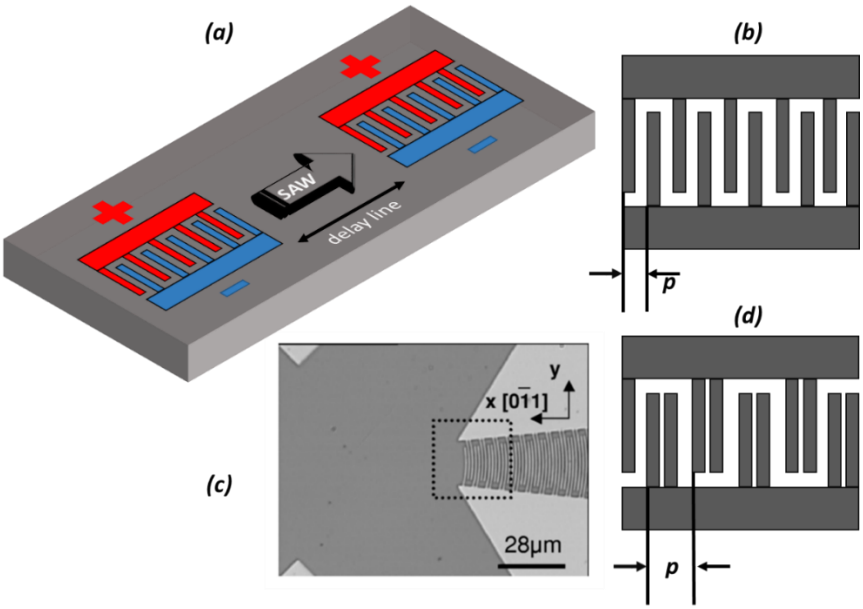

*Fig. 2.9.1. (a) A typical design of a SAW device. Different types of IDTs: (b) single finger electrodes, (c) focusing electrodes **[Lim 2003]**, (d) double finger electrodes.*

The synchronous frequency, or SAW frequency, is determined as **[Kir 2010]** $f_0 = \frac{v_p}{2p}$, where v_p is the wave velocity in the substrate and p is the pitch (fig. 2.9.1.(b,d)). Since fingers connected to different electrodes are under alternating electric fields of the same value, corresponding to the regions of maximum compression and tension, the double of the pitch is equal to the SAW wavelength. To determine the SAW frequency one needs to take into account not only the IDT design, but also the substrate material. Apart of the main synchronous frequency, or first harmonic, IDTs can also operate at integer multiples of it. Changing the width ratio between finger and the adjoining space, so called metallization ratio, results in a change of power distribution, keeping the fundamental frequency unchanged.

Another important parameter for IDT design is the bandwidth (BW), the span of SAW frequencies, where the signal is attenuated by 3 dBm (50%) from the maximum amplitude. Thus a small BW is desired to create a distinct wave with well-defined synchronous frequency, while increasing the BW will widen the operating frequency range. It can be written as **[Kir 2010]**:

$$BW = \frac{2f_0}{N} = \frac{2v_p}{L_{IDT}}, \qquad \textbf{2.9.3.}$$

where *N* is a number of IDT fingers, and L_{IDT} is the electrode length. So, in order to obtain smaller BW, one needs to increase the electrode length, which requires increasing the physical size of the device.

The material used for SAW applications should have a good electromechanical coupling ***[Kir 2010]***:

$$k^2 = \frac{mechanical\ energy\ stored}{electrical\ energy\ applied} = \frac{electrical\ energy\ stored}{mechanical\ energy\ applied} = \frac{e_{ij}^2}{C_{ij}\varepsilon}, \qquad \textbf{2.9.4.}$$

where e_{ij} are the piezoelectric coefficients, C_{ij} are the elastic constants and ε is the dielectric permittivity. k^2 describes the efficiency of energy conversion in the given piezoelectric material for a given crystallographic direction, since, in general, piezoelectric substrates are anisotropic. A large electromechanical coupling is desirable because it allows to decrease the number of metal fingers and thus reduce the size of the electrode. The values of k^2, wave velocity and piezoelectric direction for typically used piezoelectric materials is listed in table 2.9.0.:

Material	Crystal Cut	SAW axis	Velocity, m/s	K^2, %
Quartz	ST	X	3158	0.11
$LiNbO_3$	Y	Z	3488	4.5
$LiNbO_3$	128°	X	3992	5.3
$Bi_{12}GeO_{20}$	110	001	1681	1.4
$LiTaO_3$	Y	Z	3230	0.72
GaAs	<001>	(110)	<2841	<0.06

Table 2.9.0. Main parameters of most commonly used piezoelectric materials ***[Cam 1989]****.*

The IDT performance is evaluated by the conventional S-parameters, or scattering parameters. The S-parameter is the ratio of two signal quantities (i.e. voltages) and follows the notation S_{ij}, where index i determines the output signal and j the input signal from the device under testing (DUT). Thus for two port DUT there are four scattering parameters ***[Has 2000]***:

$$\begin{pmatrix} b_1 \\ b_2 \end{pmatrix} = \begin{pmatrix} S_{11} & S_{12} \\ S_{21} & S_{22} \end{pmatrix} \begin{pmatrix} a_1 \\ a_2 \end{pmatrix}, \qquad \textbf{2.9.5.}$$

where a_1 and a_2 are incident voltage waves, while b_1 and b_2 are reflected voltage waves (fig. 2.9.2.). S_{11} and S_{22} are reflection parameters and S_{21} and S_{12} are transmission parameters. SAW devices are reciprocal, meaning that input and output ports are equal, so $S_{21} = S_{12}$. Although, in reality, every system has some power dissipation and reciprocity may be broken.

Fig. 2.9.2. A representation of S-parameters for two port device under testing.

Once knowing all S-parameters, one could calculate return losses (RL) and insertion losses (IL) as *[Has 2000]*:

$$RL = -20\log|S_{11}| \text{ and } = -20\log|S_{22}|, \quad \textbf{2.9.6.}$$
$$IL = -20\log|S_{12}| \text{ and } = -20\log|S_{21}|. \quad \textbf{2.9.7.}$$

2.9.3 Acoustically induced transport

The rapidly growing field of communications requires high speed signal processing. Thus a tremendous research is conducted for new approaches. One of them is the acoustically induced transport of carriers, which not only can transport carriers at high speed, but also allows to increase the radiative lifetimes by orders of magnitude. The latter opens the possibility to manipulate recombination times in direct band gap semiconductors without any appreciable degradation of its optical properties. Additionally, this method allows to widen the dynamic range into the GHz region. Moreover, it is compatible with modern semiconductor technologies along with easily implementation with other components of on-chip optoelectronic devices.

SAWs could be used as an effective tool to transport carriers over hundreds of μm distances at sound velocities. Due to the type II modulation of the band gap, induced by SAW piezoelectric potential, electrons and holes can be stored in the corresponding potential minima, while a sufficient SAW amplitude will produce enough spatial separation to keep them away from recombination. Such trapped charges could be transported as positive and negative packets, so called ambipolar transport. Note that a sufficient mobility of carriers is required in order to follow the moving acoustic potential. The existence of potential fluctuations, acting as a traps for charges, can introduce significant transport time variations and reduce the transport efficiency for relatively small acoustic amplitudes. Such distribution of times can act as an additional source of noise for single carrier transport and thus reducing the efficiency of the signal processing schemes. Finally, just placing a layer of thin metal on the SAW pathway will screen the acoustic field and force recombination in a remote place from the generation point. Such technique could be used as an optical delay line with operation speed equal to the speed of sound.

The first successful realization of the acoustic transport concept was done in III-V semiconductor bulk layers *[Hos 1982]*. Free carriers were injected electrically or optically, than trapped in SAW potentials and extracted electrically or forced to recombine by screening the SAW field. Next step was to achieve similar results in heterostructures. And it was successfully implemented few years

later in III-V systems *[Tan 1988]*. Nowadays, various reports on acoustic transport in QW *[Roc 1997; San 2004; Rud 2007]* and wires *[Als 2002; Ebb 2008; Mol 2012; Laz 2014]* are published.

Transport efficiency in QWs has been found to be strongly dependent on the acoustic amplitudes *[San 2004]* and on the quality of the material. In high power regime an observed efficiency reduction was attributed to a decrease of the hole mobility. Two main mechanisms were suggested to be responsible: (i) light hole and heavy hole level crossing; (ii) the vertical component of the SAW piezoelectric field pushes electron and hole wave functions towards the surface, so the carrier transport path, being closer to the interface, is more sensitive to variations of the potential induced by surface roughness (fig. 2.9.3.(a)). It was experimentally determined that the hole capture probability is enhanced at high acoustic powers. Moreover, screening of the piezoelectric field by a stopping metal stripe is less efficient at high power and carrier leakage underneath can occur, resulting in an overall decrease of the remote PL emission. While under moderate acoustic powers charge transport is efficient. For this power regime an interplay between capture and release of electrons from interface traps dominate and is assisted by vertical SAW piezoelectric field component *[Als 2006]*.

On the other hand, by launching the SAW along non-piezoelectric directions in GaAs *[Rud, 2007]*, only type I modulation of the band gap is produced (fig. 2.9.3.(b)). This makes possible to transport excitons, since in this case electrons and holes are not spatially separated. Indirect excitons, as longer living ones, could be transported over hundreds of μm.

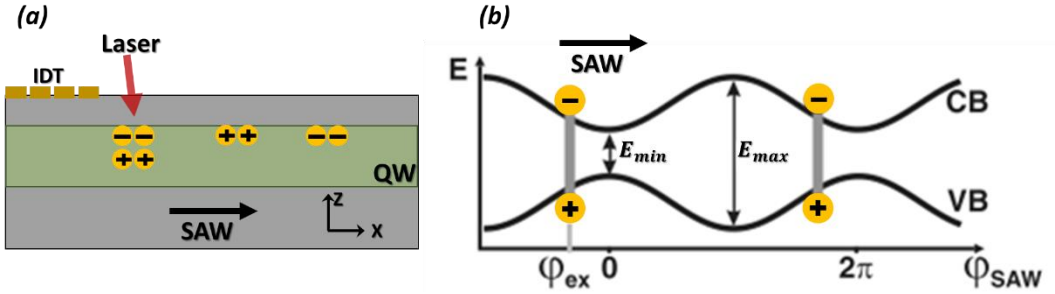

Fig. 2.9.3. (a) Representation of SAW-induced transport ***[San 2004]****.(b) Lateral type I modulation of band gap energy by SAW* ***[Rud 2007]****.*

Combining QWs with quantum wires *[Als 2002]* or QDs *[Bod 2001]* opens an opportunity to periodically inject to or extract carriers from them through acoustical transport in the surrounding well. Also, wires, embedded in wells, as in Ref *[Als 2002]* could act as efficient transport channels. That is a promising alternative to the etching techniques since it does not cause any damage of interface, thus reducing possible carrier traps.

SAW not only allows to periodically pump QDs embedded into QWs, but also to control capture and recombination rates. The latter was employed to realize triggered single photon sources operating at high frequency *[Cou 2009]*. It has also been shown that by carefully choosing the

acoustic amplitude it is possible to choose specific QD from the array and achieve a certain emission wavelength tunability.

2.9.4 Acoustically induced dynamics of carriers

Under influence of SAW, PL emission exhibits quenching due to the spatial separation of electrons and holes by the lateral component of the piezoelectric field. Further increase of the RF power leads to the splitting of the initial peak in two components, corresponding to minimum (E_{min}) and maximum (E_{max}) energy. The large time-averaged joint density of states at these positions is believed to be responsible for the splitting. The relative intensity of two components appears to be dependent on the SAW propagation direction *[San 2004]*. This dependence was explained in terms of variations of electron capture efficiency due to phase difference of strain and piezoelectric induced band gap modulations. In ensembles of QDs such intensity relation between two split doublet components can be used as an alternative identification method for differently charged excitonic complexes *[Gel 2008]*. It is interesting to note, that not only the SAW propagation direction, but also the relative alignment of the preferential axis of 1D structures, i.e. nanowires *[Kin 2011]*, resulted in difference in the optical response. Thus structural geometry combined with SAW technology allows to obtain full dynamical and directional control of the optical properties of heterostructures.

Strain induced modulation of the transition energies can be used as an effective tool to dynamically tune the emission wavelength of a device *[Gel 2008; Pus 2015]*. A properly chosen narrow spectral window ensures that collection of photons is possible only while QD emission is inside this energy range. By carefully adjusting the SAW parameters and using output spectral filtering one can achieve a high frequency tunable single photon emission with low temporal jitter and without need of pulsed excitation.

Furthermore, studies of SAW-induced spectral changes of single QDs embedded into coreshell nanowires showed pronounced anti-correlated intensity oscillations as a direct consequence of acoustically induced carrier tunneling *[Wei 2014]*. The spectral shifts were discussed in terms of deformation potential coupling, ΔE_{strain}, and QCSE, ΔE_{stark}. The first component scaled linearly with the acoustic amplitude and produced a sinusoidal oscillation at the SAW frequency, while the second was quadratic and oscillated at double frequency. The superposition of deformation potential coupling and electrical field induced Stark effect together with specifically engineered band gap structure resulted in the extraction of electrons from 0D confined states into 2D and 3D continuum. By applying stroboscopic techniques, i.e. synchronizing the optical excitation to a given SAW phase, one can generate carriers at precise points of the SAW cycle and, thus, study the acoustically induced temporal dynamics. In this way a successful programming of single QD emission intensities and excitonic occupancy state were achieved *[Sch 2013]*. Such deterministic injection/extraction of carriers to/from QDs is a desired property for quantum information processing.

References

[Ade 2003] Adelmann, C., Sarigiannidou, E., Jalabert, D., Hori, Y., Bouvière, J. L., Daudin, B., Fanget, S., Bru-Chevallier, C., Shibata, T. & Tanaka, M. Growth and optical properties of GaN/AlN quantum wells. *Appl. Phys. Lett.* **82,** 4154–4156 (2003).

[Alb 2012] Albert, S., Bengoechea-Encabo, A., Lefebvre, P., Barbagini, F., Sanchez-Garcia, M. A., Calleja, E., Jahn, U. & Trampert, A. Selective area growth and characterization of InGaN nano-disks implemented in GaN nanocolumns with different top morphologies. *Appl. Phys. Lett.* **100,** 231906 (2012).

[Als 2002] Alsina, F., Santos, P. V., Schönherr, H.-P., Seidel, W., Ploog, K. H. & Nötzel, R. Surface-acoustic-wave-induced carrier transport in quantum wires. *Phys. Rev. B* **66,** 165330 (2002).

[Als 2006] Alsina, F., Stotz, J. A. H., Hey, R. & Santos, P. V. Radiative recombination during acoustically induced transport in GaAs quantum wells. *J. Vac. Sci. Technol. B Microelectron. Nanom. Struct.* **24,** 2029 (2006).

[Ami 2009] Amirtharaj, P. M. & Seiler, D. G. *Handb. Semicond. Opt. Prop. Vol. II Devices, Meas., Prop. Chapter 36.* (eds. Bass, M., Stryland, E. W. V., Williams, D. R. & Wolfe, W. L.) McGraw Hill, New York, NY (2009).

[Aml 2011] Amloy, S., Chen, Y. T., Karlsson, K. F., Chen, K. H., Hsu, H. C., Hsiao, C. L., Chen, L. C. & Holtz, P. O. Polarization-resolved fine-structure splitting of zero-dimensional $In_xGa_{1-x}N$ excitons. *Phys. Rev. B* **83,** 201307 (2011).

[Aml 2012] Amloy, S., Karlsson, K. F., Andersson, T. G. & Holtz, P. O. On the polarized emission from exciton complexes in GaN quantum dots. *Appl. Phys. Lett.* **100,** 21901 (2012).

[Aml 2013] Amloy, S. Polarization-resolved photoluminescence spectroscopy of III-nitride quantum dots. (PhD thesis, 2013).

[Aml1 2013] Amloy, S., Karlsson, K. F. & Holtz, P. O. III-nitride based quantum dots for photon emission with controlled polarization switching. 1–6 (2013). arxiv.org/abs/1311.5731v1

[Aml 2014] Amloy, S., Karlsson, K. F., Eriksson, M. O., Palisaitis, J., Persson, P. O. Å., Chen, Y. T., Chen, K. H., Hsu, H. C., Hsiao, C. L., Chen, L. C. & Holtz, P. O. Excitons and biexcitons in InGaN quantum dot like localization centers. *Nanotechnology* **25,** 495702 (2014).

[And 2000] Andreev, A. D. & O'Reilly, E. P. Theory of the electronic structure of GaN/AlN hexagonal quantum dots. *Phys. Rev. B - Condens. Matter Mater. Phys.* **62,** 15851–15870 (2000).

[Ara 2002] Arakawa, Y. Progress in GaN-based quantum dots for optoelectronics applications. *IEEE J. Sel. Top. Quantum Electron.* **8,** 823–832 (2002).

[Ase 2016] Aseev, P., Gačević, Ž., Torres-Pardo, A., González-Calbet, J. M. & Calleja, E. Improving optical performance of GaN nanowires grown by selective area growth homoepitaxy: Influence of substrate and nanowire dimensions. *Appl. Phys. Lett.* **108,** 253109 (2016).

[Bar 2008] Bardoux, R., Guillet, T., Gil, B., Lefebvre, P., Bretagnon, T., Taliercio, T., Rousset, S. & Semond, F. Polarized emission from GaN/AlN quantum dots: Single-dot spectroscopy and symmetry-based theory. *Phys. Rev. B* **77,** 235315 (2008).

[Bir 1959] Birman, J. L. Some Selection Rules for Band-Band Transitions in Wurtzite Structure. *Phys. Rev.* **114,** 1490–1492 (1959).

[Bod 2001] Bödefeld, C., Wixforth, A., Toivonen, J., Sopanen, M. & Lipsanen, H. Pumping of Quantum Dots with Surface Acoustic Waves. *Phys. Status Solidi* **224,** 703–706 (2001).

[Bro 1956] Brown, R. H. & Twiss, R. Q. Correlation between Photons in two Coherent Beams of Light. *Nature* **177,** 27–29 (1956).

[Cal 2000] Calleja, E., Sánchez-García, M. A., Sánchez, F. J., Calle, F., Naranjo, F. B., Muñoz, E., Jahn, U. & Ploog, K. Luminescence properties and defects in GaN nanocolumns grown by molecular beam epitaxy. *Phys. Rev. B* **62,** 16826–16834 (2000).

[Cam 1989] Campbell, C. *Surface Acoustic Wave Devices and Their Signal Processing Applications*. (ACADEMIC PRESS, INC., 1989).

[Cou 2009] Couto, O. D. D., Lazić, S., Iikawa, F., Stotz, J. A. H., Jahn, U., Hey, R. & Santos, P. V. Photon anti-bunching in acoustically pumped quantum dots. *Nat. Photonics* **3,** 645–648 (2009).

[Ebb 2008] Ebbecke, J., Maisch, S., Wixforth, A., Calarco, R., Meijers, R., Marso, M. & Lüth, H. Acoustic charge transport in GaN nanowires. *Nanotechnology* **19,** 275708 (2008).

[For 1996] Forchel, A., Steffen, R., Koch, T., Michel, M., Albrecht, M. & Reinecke, T. L. Optical studies of free-standing single InGaAs/GaAs quantum dots. *Semicond. Sci. Technol.* **11,** 1529–1533 (1996).

[Gac 2015] Gačević, Ž., Bengoechea-Encabo, A., Albert, S., Torres-Pardo, A., González-Calbet, J. M. & Calleja, E. Crystallographically uniform arrays of ordered (In)GaN nanocolumns. *J. Appl. Phys.* **117,** 35301 (2015).

[Gac 2016] Gačević Ž., López-Romero, D., Juan Mangas, T. & Calleja, E. A top-gate GaN nanowire metal-semiconductor field effect transistor with improved channel electrostatic control. *Appl. Phys. Lett.* **108,** 33101 (2016).

[Gel 2008] Gell, J. R., Ward, M. B., Young, R. J., Stevenson, R. M., Atkinson, P., Anderson, D., Jones, G. A. C., Ritchie, D. A. & Shields, A. J. Modulation of single quantum dot energy levels by a surface-acoustic-wave. *Appl. Phys. Lett.* **93,** 81115 (2008).

[Ger 2005] Gerry, C. & Knight, P. *introductory quantum optics*. *Cambridge Univ. Press* **1,** (2005).

[Gre 1980] Green, J. B., Kino, G. S. & Khuri-Yakub, B. T. Focused surface wave transducers on anisotropic subtrates : a theory developed for the waveguided storage correlation. *Ultrason. Symp. 1980* 69–73 (1980).

[Has 2000] Hashimoto, K. *Surface Acoustic Wave Devices in Telecommunications*. (Springer Berlin Heidelberg, 2000).

[Hel 2003] Helman, A., Tchernycheva, M., Lusson, A., Warde, E., Julien, F. H., Moumanis, K., Fishman, G., Monroy, E., Daudin, B., Le Si Dang, D., Bellet-Amalric, E. & Jalabert, D. Intersubband spectroscopy of doped and undoped GaN/AlN quantum wells grown by molecular-beam epitaxy. *Appl. Phys. Lett.* **83,** 5196–5198 (2003).

[Hil 1982] Hilborn, R. C. Einstein coefficients, cross sections, f values, dipole moments, and all that. *Am. J. Phys.* **50,** 982 (1982).

[Hol 2014] Holmes, M. J., Choi, K., Kako, S., Arita, M. & Arakawa, Y. Room-temperature triggered single photon emission from a III-nitride site-controlled nanowire quantum dot. *Nano Lett.* **14,** 982–6 (2014).

[Hoo 1995] Hooper, S., Foxon, C. & Cheng, T. Some aspects of GaN growth on GaAs (100) substrates using molecular beam epitaxy with an RF activated nitrogen-plasma source. *J. Cryst. Growth* **155,** 157–163 (1995).

[Hos 1982] Hoskins, M. J., Morkoç, H. & Hunsinger, B. J. Charge transport by surface acoustic waves in GaAs. *Appl. Phys. Lett.* **41,** 332 (1982).

[Hsu 2011] Hsu, C.-W., Lundskog, A., Karlsson, K. F., Forsberg, U., Janzén, E. & Holtz, P. O. Single Excitons in InGaN Quantum Dots on GaN Pyramid Arrays. *Nano Lett.* **11,** 2415–2418 (2011).

[Hua 2002] Huang, Y., Duan, X., Cui, Y. & Lieber, C. M. Gallium Nitride Nanowire Nanodevices. *Nano Lett.* **2,** 101–104 (2002).

[Hub 2013] Hubbard, S. M., Podell, A., Mackos, C., Polly, S., Bailey, C. G. & Forbes, D. V. Effect of vicinal substrates on the growth and device performance of quantum dot solar cells. *Sol. Energy Mater. Sol. Cells* **108,** 256–262 (2013).

[Kin 2011] Kinzel, J. B., Rudolph, D., Bichler, M., Abstreiter, G., Finley, J. J., Koblmüller, G., Wixforth, A. & Krenner, H. J. Directional and Dynamic Modulation of the Optical Emission of an Individual GaAs Nanowire Using Surface Acoustic Waves. *Nano Lett.* **11,** 1512–1517 (2011).

[Kin 2010] Kindel, C., Kako, S., Kawano, T., Oishi, H., Arakawa, Y., Hönig, G., Winkelnkemper, M., Schliwa, A., Hoffmann, A. & Bimberg, D. Exciton fine-structure splitting in GaN/AlN quantum dots. *Phys. Rev. B* **81,** 241309 (2010).

[Kir 2010] Kirschner, J. Surface Acoustic Wave Sensors (SAWS): Design for Application. *Microelectromechanical Syst.* 1–11 (2010).

[Kuy 2007] Kuykendall, T., Ulrich, P., Aloni, S. & Yang, P. Complete composition tunability of InGaN nanowires using a combinatorial approach. *Nat. Mater.* **6,** 951–956 (2007).

[Laz 2014] Lazić, S., Hey, R. & Santos, P. V. Acoustic carrier transport in GaAs nanowires. *Top. Appl. Phys.* **128,** 259–292 (2014).

[Lea 2002] Leatherdale, C. A., Woo, W. K., Mikulec, F. V & Bawendi, M. G. On the absorption cross section of CdSe nanocrystal quantum dots. *J. Phys. Chem. B* **106,** 7619–7622 (2002).

[Lev 2011] Lévesque, A., Desjardins, P., Leonelli, R. & Masut, R. A. Temperature dependence of the photoluminescence spectra from InAs(P)/InP multilayers containing thick quantum dots: Dot-size-dependent carrier dynamics. *Phys. Rev. B* **83,** 235304 (2011).

[Lim 2003] Lima, M. M., Alsina, F., Seidel, W. & Santos, P. V. Focusing of surface-acoustic-wave fields on (100) GaAs surfaces. *J. Appl. Phys.* **94,** 7848 (2003).

[Lim 2004] Lima, M. M., Seidel, W., Kostial, H. & Santos, P. V. Embedded Interdigital transducers for high-frequency surface acoustic waves on GaAs. *J. Appl. Phys.* **96,** 3494–3500 (2004).

[Lim 2005] Lima, M. M. & Santos, P. V. Modulation of photonic structures by surface acoustic waves. *Reports Prog. Phys.* **68,** 1639–1701 (2005).

[Lou 1983] Loudon, R. *The Quantum Theory of Light*. (Oxford University Press Inc, 1983).

[Mar 2005] Martin, R. W., Edwards, P. R., Taylor, R. A., Rice, J. H., Na, J. H., Robinson, J. W., Smith, J. D., Liu, C. & Watson, I. M. Luminescence properties of isolated InGaN/GaN quantum dots. *Phys. Status Solidi* **202,** 372–376 (2005).

[Mot 2007] Motayed, A., Vaudin, M., Davydov, A. V, Melngailis, J., He, M. Q. & Mohammad, S. N. Diameter dependent transport properties of gallium nitride nanowire field effect transistors. *Appl. Phys. Lett.* **90,** 43104 (2007).

[Mol 2012] Möller, M., Hernández-Mínguez, A., Breuer, S., Pfüller, C., Brandt, O., de Lima, M. M., Cantarero, A., Geelhaar, L., Riechert, H. & Santos, P. V. Polarized recombination of acoustically transported carriers in GaAs nanowires. *Nanoscale Res. Lett.* **7,** 247 (2012).

[Mul 2013] Müller, K., Bechtold, A., Ruppert, C., Kaldewey, T., Zecherle, M., Wildmann, J. S., Bichler, M., Krenner, H. J., Villas-Bôas, J. M., Abstreiter, G., Betz, M. & Finley, J. J. Probing ultrafast carrier tunneling dynamics in individual quantum dots and molecules. *Ann. Phys.* **525,** 49–58 (2013).

[Pau 1982] Paul, H. Photon antibunching. *Rev. Mod. Phys.* **54,** 1061–1102 (1982).

[Pos 2003] Poser, F., Bhattacharya, A., Weeke, S. & Richter, W. Growth of spatially ordered InAs quantum dots on step-bunched vicinal GaAs (100) substrates. *J. Cryst. Growth* **248,** 317–321 (2003).

[Pus 2015] Pustiowski, J., Müller, K., Bichler, M., Koblmüller, G., Finley, J. J., Wixforth, A. & Krenner, H. J. Independent dynamic acousto-mechanical and electrostatic control of individual quantum dots in a LiNbO3-GaAs hybrid. *Appl. Phys. Lett.* **106,** 13107 (2015).

[Ram 1998] Ramvall, P., Tanaka, S., Nomura, S., Riblet, P. & Aoyagi, Y. Observation of confinement-dependent exciton binding energy of GaN quantum dots. *Appl. Phys. Lett.* **73,** 1104–1106 (1998).

[Ray 1885] Rayleigh, Lord. On Waves Propagated along the Plane Surface of an Elastic Solid. *Proc. London Math. Soc.* **s1-17,** 4–11 (1885).

[Rei 2008] Reischle, M., Beirne, G. J., Schulz, W.-M., Eichfelder, M., Roßbach, R., Jetter, M. & Michler, P. Electrically pumped single-photon emission in the visible spectral range up to 80 K. *Opt. Express* **16,** 12771 (2008).

[Rez 2006] Rezaei, B., Asgari, A. & Kalafi, M. Electronic band structure pseudopotential calculation of wurtzite III-nitride materials. *Phys. B Condens. Matter* **371,** 107–111 (2006).

[Roc 1997] Rocke, C., Zimmermann, S., Wixforth, A., Kotthaus, J. P., Böhm, G. & Weimann, G. Acoustically Driven Storage of Light in a Quantum Well. *Phys. Rev. Lett.* **78,** 4099–4102 (1997).

[Rod 2001] Rodina, A., Dietrich, M., Göldner, A., Eckey, L., Hoffmann, A., Efros, A., Rosen, M. & Meyer, B. Free excitons in wurtzite GaN. *Phys. Rev. B* **64,** 11–14 (2001).

[Rom 2006] Romanov, A. E., Baker, T. J., Nakamura, S. & Speck, J. S. Strain-induced polarization in wurtzite III-nitride semi-polar layers. *J. Appl. Phys.* **100,** 23522 (2006).

[Rud 2007] Rudolph, J., Hey, R. & Santos, P. Long-Range Exciton Transport by Dynamic Strain Fields in a GaAs Quantum Well. *Phys. Rev. Lett.* **99,** 47602 (2007).

[San 1998] Sanchez-Garcia, M. A., Calleja, E., Monroy, E., Sanchez, F. J., Calle, F., Munoz, E. & Beresford, R. The effect of the III/V ratio and substrate temperature on the morphology and properties of GaN- and AlN-layers grown by molecular beam epitaxy on Si(1 1 1). *J. Cryst. Growth* **183,** 23–30 (1998).

[San 2004] Santos, P. V., Alsina, F., Stotz, J. A. H., Hey, R., Eshlaghi, S. & Wieck, A. D. Band mixing and ambipolar transport by surface acoustic waves in GaAs quantum wells. *Phys. Rev. B* **69,** 155318 (2004).

[Sch 2013] Schülein, F. J. R., Müller, K., Bichler, M., Koblmüller, G., Finley, J. J., Wixforth, A. & Krenner, H. J. Acoustically regulated carrier injection into a single optically active quantum dot. *Phys. Rev. B* **88,** 85307 (2013).

[Scu 1997] Scully, M. O. & Zubairy, M. S. Quantum Optics. *Cambridge Univ. Press* 630 (1997).

[Sek 2010] Sekiguchi, H., Kishino, K. & Kikuchi, A. Emission color control from blue to red with nanocolumn diameter of InGaN/GaN nanocolumn arrays grown on same substrate. *Appl. Phys. Lett.* **96,** 231104 (2010).

[Tan 1988] Tanski, W. J., Merritt, S. W., Sacks, R. N., Cullen, D. E., Branciforte, E. J., Carroll, R. D. & Eschrich, T. C. Heterojunction acoustic charge transport devices on GaAs. *Appl. Phys. Lett.* **52,** 18 (1988).

[Tat 2000] Tatebayashi, J., Nishioka, M., Someya, T. & Arakawa, Y. Area-controlled growth of InAs quantum dots and improvement of density and size distribution. *Appl. Phys. Lett.* **77,** 3382 (2000).

[Vur 2001] Vurgaftman, I., Meyer, J. R. & Ram-Mohan, L. R. Band parameters for III–V compound semiconductors and their alloys. *J. Appl. Phys.* **89,** 5815 (2001).

[Wag 2002] Wagner, J.-M. & Bechstedt, F. Properties of strained wurtzite GaN and AlN: Ab initio studies. *Phys. Rev. B* **66,** 115202 (2002).

[Wan 2004] Wang, X.-D., Liu, N., Shih, C. K., Govindaraju, S. & Holmes, A. L. Spatial correlation-anticorrelation in strain-driven self-assembled InGaAs quantum dots. *Appl. Phys. Lett.* **85,** 1356 (2004).

[Wei 2014] Weiß, M., Kinzel, J. B., Schülein, F. J. R., Heigl, M., Rudolph, D., Morkötter, S., Döblinger, M., Bichler, M., Abstreiter, G., Finley, J. J., Koblmüller, G., Wixforth, A. & Krenner, H. J. Dynamic Acoustic Control of Individual Optically Active Quantum Dot-like Emission Centers in Heterostructure Nanowires. *Nano Lett.* **14,** 2256–2264 (2014).

[Whi 1965] White, R. M. & Voltmer, F. W. Direct piezoelectric coupling to surface elastic waves. *Appl. Phys. Lett.* **7,** 314 (1965).

[Wil 1985] Wilcox, J. Z. & Brooks, R. E. Frequency-dependent beam steering by a focusing array of surface acoustic wave transducers: Experiment. *J. Appl. Phys.* **58,** 1160 (1985).

[Win 2006] Winkelnkemper, M., Schliwa, A. & Bimberg, D. Interrelation of structural and electronic properties in $In_xGa_{1-x}GaN$ quantum dots using an eight-band k·p model. *Phys. Rev. B* **74,** 155322 (2006).

[Win 2007] Winkelnkemper, M., Seguin, R., Rodt, S., Schliwa, A., ReiBmann, L., Strittmatter, A., Hoffmann, A. & Bimberg, D. Polarized emission lines from A-and B-type excitonic complexes in single InGaN/GaN quantum dots. *J. Appl. Phys.* **101,** 113708 (2007).

[Win 2008] Winkelnkemper, M., Seguin, R., Rodt, S., Hoffmann, A & Bimberg, D. GaN/AlN quantum dots for single qubit emitters. *J. Phys. Condens. Matter* **20,** 454211 (2008).

[Woo 2008] Wood, C. & Jena, D. *Polarization Effects in Semiconductors. From Ab Initio Theory to Device Applications*. (Springer, 2008).

[Yos 1997] Yoshizawa, M., Kikuchi, A., Mori, M., Fujita, N. & Kishino, K. Growth of Self-Organized GaN Nanostructures on Al_2O_3(0001) by RF-Radical Source Molecular Beam Epitaxy. *Jpn. J. Appl. Phys.* **36,** L459–L462 (1997).

[Yu 2010] Yu, P. Y. & Cardona, M. *Fundamentals of Semiconductors*. **7,** (Springer Berlin Heidelberg, 2010).

[Zha 2003] Zhang, X. B., Heller, R. D., Noh, M. S., Dupuis, R. D., Walter, G. & Holonyak, N. Growth of InP quantum dots on vicinal GaAs (100) substrates by metalorganic chemical vapor deposition. *Appl. Phys. Lett.* **83,** 476 (2003).

[Zha 2013] Zhang, L., Teng, C.-H., Hill, T. A., Lee, L.-K., Ku, P.-C. & Deng, H. Single photon emission from site-controlled pyramidal quantum dots. *Appl. Phys. Lett.* **84,** 648–650 (2013).

[Zha 2016] Zhang, L., Teng, C.-H., Ku, P.-C. & Deng, H. Site-controlled InGaN/GaN single-photon-emitting diode. *Appl. Phys. Lett.* **108,** 153102 (2016).

3 CHAPTER. EXPERIMENTAL TECHNIQUES

Optical spectroscopy is a powerful tool for exploring fundamental properties of semiconductor heterostructures and it was the main one used throughout this work. The optical properties were investigated by means of micro-photoluminescence (μ-PL) with spatial, temporal and polarization resolution. Statistical properties of the emitted light were studied by Hanbury-Brown and Twiss interferometry. Acoustical modulation was achieved by the use of surface acoustic waves (SAWs), including stroboscopic excitation and detection. Although additional techniques (optical microscopy, scanning electron microscopy, transmission electron microscopy cathodoluminescence) were employed for more detailed structural investigation, this chapter will mainly focus on the optical characterization and its instrumental realization, including the use of surface acoustic waves.

3.1 PHOTOLUMINESCENCE SPECTROSCOPY

The primary task was to identify single QD-like emission centers in NW heterostructures. Low temperature μ-PL spectroscopy was chosen for that purpose since it allows to excite only small areas (up to ~ 3 μm^2) thus facilitating optical excitation and emission detection from a single wire–QD structure. Pulsed diode ($\lambda = 442$ nm) and continuous wave (cw) He-Cd ($\lambda_1 = 325$ nm and $\lambda_2 = 442$ nm) lasers were used as excitation sources. The excitation energy as well as the operational mode were chosen depending on the band gap of the investigated structures and type of experiment. In order to access emission properties of the QD structures it was necessary to cool down the sample to liquid He temperatures. This was achieved in a continuous flow CryoVac cryostat (Konti-Cryostat Mikro-Spektro). The samples were mounted on the copper cold-finger holder by means of silver paste, which ensured proper thermal contact. A Si sensor (DT670A) inside the cryostat and the temperature control unit (TIC 304-MA) were employed to monitor and control the temperature. A typical temperature range was 10 – 300 K. The cryostat was mounted on a XYZ linear translation stage (Newport) to allow rough position adjustments with μm precision. Fine position adjustments were achieved by moving the microscope objective by computer controlled DC servo motors (Newport TRA25CC, Convex-CC controller) with 100 nm incremental step. A visible 100x microscope objective Nikon (CF SLWD Plan EPI M VIS) or ultraviolet 50x Mitutoyo (M Plan UV) were used to focus the laser on the sample as well as to collect the signal emitted from it.

Laser power was controlled by a neutral density filter wheel (Thorlabs) providing continuously adjustable attenuation via wheel rotation. Power monitoring was done with a digital optical power meter (Thorlabs) with Si photodiode.

3.1.1 Time-averaged micro-photoluminescence

The experimental setup is schematically presented in fig. 3.1.0. For time-averaged experiments both UV and VIS lines of He-Cd laser were used. The selected laser wavelength was cleaned from

plasma lines by the corresponding laser line filter (table 3.1.0.), and then directed onto the beam-splitter (BS). The BS was mounted on the XYZ linear translation stage (Standa) for the rough positioning, together with the tip, tilt & rotational stage (Altechna) for the final optical adjustment. The reflected laser beam was sent to the sample, while the transmitted beam was sent to the power meter (not shown in the figure). In this way the laser power was constantly monitored during the experiment. The signal from the sample was collected by the microscope objective and transmitted by the same BS onto a single grating spectrometer. A razor edge filter, placed in front of the spectrometer entrance slit, served to block the laser reflection. All optical components were chosen with appropriate coating (visible, ultraviolet or uncoated) in order to minimize optical losses. Broad band highly reflective mirrors (Semrock) were used to guide the laser and the signal throughout the setup.

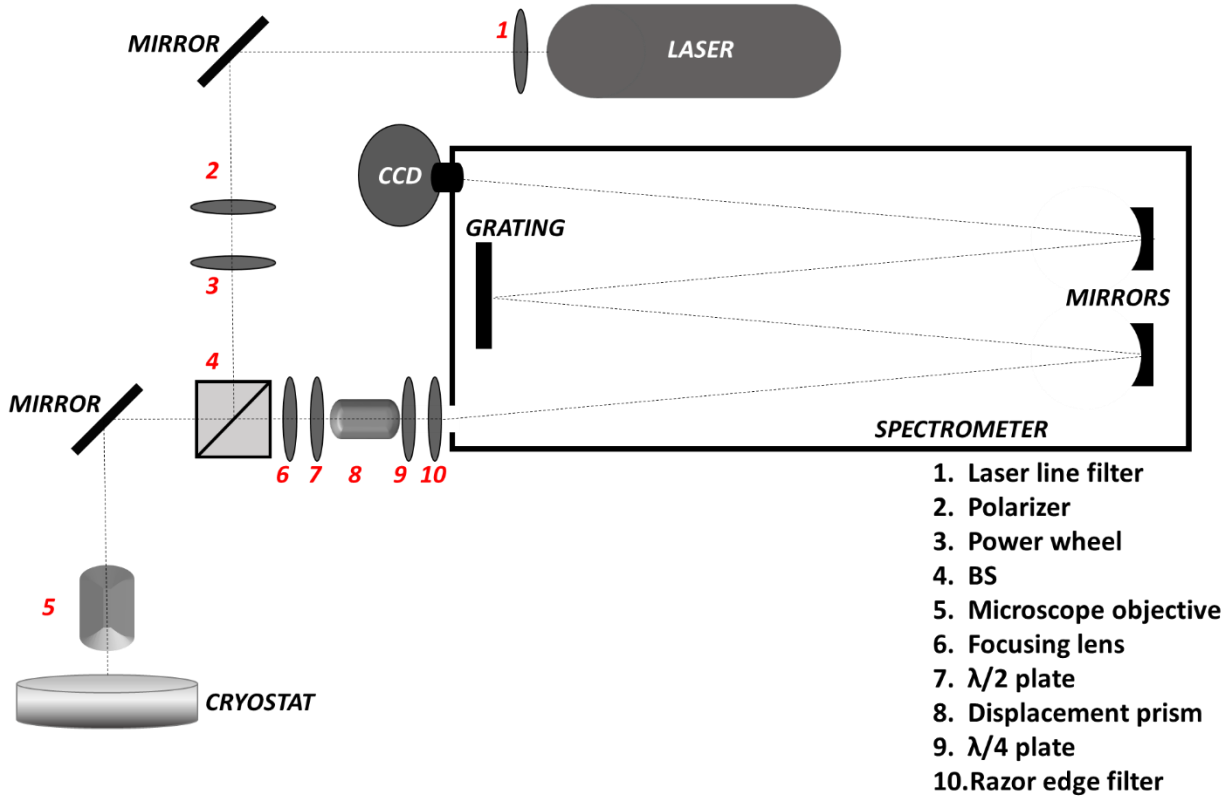

Fig. 3.1.0. Schematics of the experimental setup used for μ-PL measurements.

A single grating spectrometer SPEX 1000M with vertical slits was used to disperse the emitted light. The signal was detected by a liquid nitrogen cooled Si charged coupled device (CCD) camera. Control of the CCD as well as the processing of the acquired data was made through SynerJY software. A more detailed information about the setup components can be found in tables 3.1.0-1.

The spectrometer spectral resolution for a given slit width can be estimated as:

$$\Delta\lambda = \frac{d}{F}\Delta x, \qquad \textbf{3.1.0.}$$

where Δx is the slit width, F is the spectrometer focal length and d is the grating period. Since F and d are fixed parameters given by the spectrometer configuration, for a given wavelength range only the slit width can be changed to obtain a desired resolution. The input slit was typically 100-150 µm in order to obtain both fine spectral resolution and best signal to background ratio.

An uncoated lens with $F = 35$ cm, placed on XYZ linear translation stage (Standa), (see 6 in fig. 3.1.0.) was used to focus the signal on the entrance slit of the spectrometer.

Optical components	**Specifications**
Laser filters	
Laser line filters	Semrock LL01-325-12.5, CWL 325 nm, FWHM 2.3 nm, T>80%; Thorlabs FB405-10, CWL 405 ± 2 nm, FWHM 10 ± 2 nm; Semrock LL01-407-12.5, CWL 407 nm, FWHM 2.8 nm, T>90%; Semrock LL01-442-12.5, CWL 441.6 nm, FWHM 3.1 nm, T>90%;
Razor edge filters	Semrock LP03-325RU-25, edge wavelength 327.5 nm, T>90%; Semrock FF02-409/LP-25, edge wavelength 415 nm, T>93%; Semrock LP02-442RU-25, edge wavelength 445 nm, T>93%;
Beam-splitters	
BS019	Thorlabs, cube 25.4 mm, 30:70 (R:T), range 400 –700 nm, non-polarizing;
BS013	Thorlabs, cube 25.4 mm, 50:50 (R:T), range 400 –700 nm, non-polarizing;
BSW10	Thorlabs, UVFS plate, 50:50 (R:T), range 400 – 700 nm;
BS S1-UV	Esco Optics, cube 25.4 mm, 50:50 (R:T), range 200 – 700 nm, non-polarizing;
Polarization optics	
Linear polarizers	Newport 10LP-VIS-B, 25.4 mm, range 430 – 670 nm; Newport 10LP-UV, 25.4 mm, range 300 – 450 nm;
Displacement prism	Thorlabs BD27, range 0.35 – 2.3 µm, beam separation 2.7 mm;
λ/2 retardation plates	Newport achromatic 10RP52-1, 25.4 mm, range 400 – 700 nm;

	Thorlabs achromatic AHWP05M-340, mounted, range 260 – 410 nm;
λ/4 retardation plates	Newport achromatic 10RP52-1, 25.4 mm, range 400 – 700 nm; B.Halle Nachfl. GmbH RSU1.4.10, 25 mm, super-achromatic, range 310 – 1100 nm;
Other optics	
Mirrors	Semrock MM2-311-25.4, range 350 – 1100 nm, R>99%;
lenses	Plano-convex, uncoated, F = 35 cm; Thorlabs AC127-025-A-ML, achromatic doublet, range 400 – 700 nm, F=2.5 cm; Thorlabs AC254-060-A-ML, achromatic doublet, range 400 – 700 nm, F=6 cm;
Microscope objectives	Nikon CF SLWD Plan EPI M, 100x, NA=0.73, WD= 4.7 mm, F=2 mm; Mitutoyo M Plan UV 50x/0.41 ∞/0, F=4 mm;
Band pass filter	Thorlabs FES0650, short pass filter, cut-off wavelength 650 nm;

Table 3.1.0. Specifications for optical components. CWL – central wavelength, FWHM – full width half maximum, NA – numerical aperture, WD – working distance, R – reflection, T – transmission, F – focal length.

In order to facilitate the search for nanowires with the desired properties an imaging system (not shown in fig. 3.1.0.) formed by a video camera (Qimaging QICAM) and a white light source (Intralux 4100) was used to visualize the sample surface. The achieved magnification (MA) for 100x Nikon objective was 175.

For polarization-resolved spectroscopy a half-wave (λ/2) retardation plate and a beam displacer prism (see 7 and 8, respectively in fig. 3.1.0.) were inserted in front of the slit. The λ/2 plate was mounted on a rotational stage controlled by a step motor (Thorlabs TDC001). The beam displacer prism (see 8 in fig. 3.1.0.) vertically separated the input beam into two orthogonally polarized components, thus allowing to simultaneously record both vertical and horizontal polarizations in different pixel rows. This significantly speeds up polarization-resolved measurements. The polarization of the excitation source was monitored by a linear polarizer (see 2 in fig. 3.1.0.). The linear polarization of the emitted light was converted to circular by a quarter-wave plate placed in front of the slit. In this way the polarization sensibility of the spectrometer grating was eliminated.

name	**specifications**
Laser sources	
He-Cd	Kimmon, dual wavelength (325/442) continuous wave operation;
Pulsed diode	P-C-405B, minimum pulse width 50 ps; P-C-440B, minimum pulse width 70 ps;

Pulsed laser controller	PDL 800B, repetition frequency up to 40 MHz;
Spectrometer	
SPEX 1000M	F = 1 m, spectral limit 0-15000 Å, resolution 0.008 nm, blazed grating 1800 grooves/mm;
Detectors	
CCD camera	Horiba Jobin Ybon, 1LS-1024x256-BD, pixel size = 26 µm, range UV-NIR, back-illuminated, detection efficiency at 450 nm ~ 90%;
APD	PerkinElmer SPCM-AQR-16, dead time 50 ns, dark count rate <25 counts/s, detection efficiency at 450 nm ~ 30%, active area diameter 175 µm, time resolution 350 ps, afterpulsing probability 0.5 %; MicroPhotonDevices silicon avalanche photodiode (SPAD), dead time 77.8 ns, dark count rate <25 counts/s, detection efficiency at 450 nm ~ 35%, active area diameter 50 µm, time resolution <50 ps, afterpulsing probability <3 %;
TCSPC	PicoQuant: PicoHarp300, dead time <95 ns, time resolution 4 ps;

Table 3.1.1. Specifications for lasers, detectors and spectrometer.

3.1.2 Time-resolved micro-photoluminescence

Time-resolved PL (TRPL) allows to study the dynamical aspects of recombination processes. The PL emission at a fixed wavelength is monitored as a function of time after a short excitation pulse. The generated electron-hole pairs decay to the lower states, then recombine and emit photons. The time evolution of the emitted light intensity gives access to the recombination dynamics (lifetime and eventual recharging processes) of the QD states.

Since the amount of the emitted light is usually very low (few photons per excitation cycle) and the emission time scale is very fast (of the order of hundreds of picoseconds to tens of nanoseconds for semiconductor QDs) a conventional detection system cannot provide the required time-resolution. A general solution is to reconstruct the photon decay profile from the data collected over many excitation cycles. To this end we use a time-correlated single photon counting (TCSPC) system, also used in photon correlation measurements (see below) ***[Wah 2009; Bec 2004]***. The laser pulse serves as a time reference: the measurement starts upon receiving an excitation pulse and stops once receiving a photon, or, otherwise, restarts when next excitation pulse arrives. The photon registration in our case is achieved by photomultiplier tubes (PMTs) and avalanche photodiodes (APDs) for UV and VIS QD emission ranges. The electronics and detectors have a dead time typically of the order of tens- to hundreds of nanoseconds. During this time the instrument is processing previously acquired data. So, if there are two or more

photons emitted per excitation cycle, only the first one would be detected, while the next ones would be missed, leading to the over-representation of early photons and the subsequent distortion of the decay profile. Therefore keeping the multiphoton detection probability low is a crucial condition. Also there could be many cycles without any photon detection. The histogram (fig. 3.1.1.), acquired in such conditions is a reasonable representation of photon decay *[Bec 2005]*.

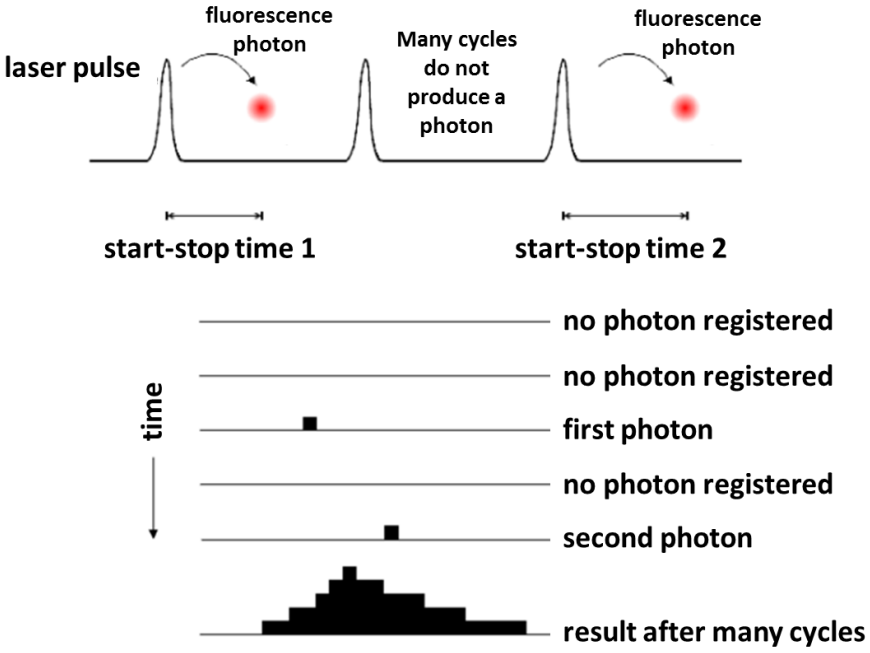

Fig. 3.1.1. An illustration of the histogram formation principle [PicoQ].

Usually the most critical component of a TCSPC setup in terms of time resolution is the detector, because it has a timing uncertainty in the conversion of photon into electrical signal. The second important part is the excitation source. The synchronous start/stop electrical signal that it produces should have as lower jitter as possible. The time jitter from other electronic components of the TCSPC setup is usually quite low, but it is still important to use properly shielded coaxial cables to keep electrical noise pickup as low as possible. The total time uncertainty due to all components of a TCSPC setup can be accounted for by the overall instrument response function (IRF) width: $e_{total}^{IRF} \cong \sqrt{\sum (e_i^{IRF})^2}$, e_i^{IRF} stands for IRF width for each component *[Wah 2009]*. In this Thesis silicon avalanche photodiodes (APD) were used for time-resolved measurements for polar QDs (Chapters 4 and 6) and PMTs for semi-polar and non-polar QDs (Chapter 5). The APD is a semiconductor analog of PMTs and, thus, have similar operating principle. Their main advantage over PMTs is essentially the higher quantum efficiency, i.e. the probability of a photon to release a photoelectron. For single photon counting applications the APD should operate in a "Geiger-mode", biased slightly above the breakdown voltage, so a single photon detection would generate up to 10^8 carriers. The electrical output produced in this way

contains not only the information about the successful detection event but also the time when it occurred. The latter is achieved in following steps: (i) the time difference between a successful photon event and the closest excitation pulse is measured, by converting the time difference into an electrical signal; (ii) the obtained value is assigned to one memory cell, i.e. time bin; (iii) a histogram is created. Such histogram memory can be read out once sufficient counts have been collected *[Wah 2007]*.

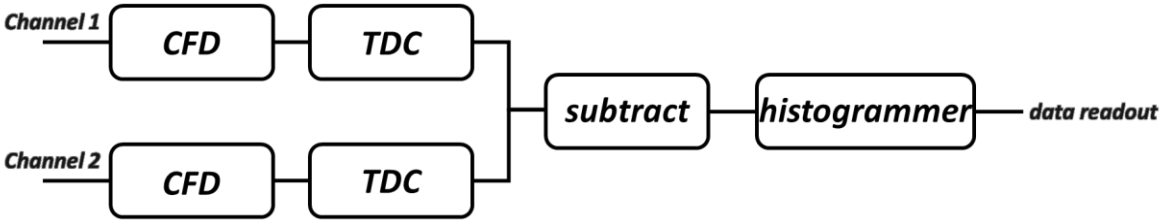

Fig. 3.1.2. A diagram of a conventional TCSPC system.

A conventional TCSPC system is presented in fig. 3.1.2. as a block-diagram. A constant fraction discriminator (CFD), is used to set the noise level rejection to filter electrical pulses of low amplitudes *[Bec 2005]*. In this way a precise time information can be extracted from the electrical pulses, delivered by the detectors. An electrical signal, supplied by the laser is connected to the Channel 0 and triggers the TCSPC unit. A TCSPC unit from PicoQuant, used in this Thesis, has CFD on both channels, making both inputs identical. Signals from both channels adjusted independently to the suitable level are fed to the corresponding Time to Digital Converter (TDC) which provides a digital representation of the time at which an event on the corresponding channel took place. The timing difference between the events registered on both input channels is then obtained by simple arithmetic in the hardware. And, finally, fast digital logic is used for histogramming: it increments each histogram memory cell in the Histrogrammer.

A scheme of the experimental setup used for TRPL is presented in fig. 3.2.0. Once the QD under study was found in time-averaged spectra on the CCD a swapping mirror placed on the second exit slit of the spectrometer was used to direct the emission to the APD. For TRPL the beam-splitter (see 3 in fig. 3.2.0.) was removed in order to gain more counts on the detector and only the detector in the transmission arm was used. A removable mirror allowed to easily exchange excitation sources from cw to pulsed lasers without the need for optical realignment. On both input channels of the TCSPC unit additional attenuators with fixed attenuation level of 10 dBm were inserted to prevent any possible electrical crosstalk between the channels.

The optical alignment of the detectors was done with a strongly attenuated laser. Firstly, the laser spot was positioned on a given pixel (corresponding to the image of the entrance slit) near the center of the CCD matrix. Then the focusing lens in front of the APD (see fig. 3.2.0.) were adjusted in order to center and focus the signal onto the detectors. Finally, the emission from the targeted QD-NW was positioned on the same CCD pixel by rotating the spectrometer grating. The width of the exit slit was determined for each QD separately. The FWHM of the emission line,

obtained on the CCD was multiplied by 26 μm (size of the CCD pixel) to obtain the slit value. In this way only the desired emission was collected and sent to the APDs and the influence of the background signal was significantly suppressed.

3.2 PHOTON-CORRELATION SPECTROSCOPY

To study the photon correlations, an HBT interferometer was constructed and integrated into the μ-PL setup (fig. 3.2.0.). Emission from the QD under consideration was filtered by the spectrometer and directed through the spectrometer exit slit to a 50/50 non-polarizing beam-splitter and photon counting detectors (see 3 and 5 in fig. 3.2.0., respectively). Two Perkin-Elmer SPADs were used as detectors for the QDs, emitting in visible range. For the QDs, emitting in UV Hamamatsu PMTs were used. A pulse inverter with attenuation (PicoQuant SIA400) was inserted on the output of these detectors to match their signal to the inputs of TCSPC electronics input requirements. A lens (see 2 in fig. 3.2.0.), inserted just after the spectrometer exit slit collimates the signal beam. Lenses mounted on XYZ linear translation stages (Mitutoyo) in front of single photon countitng detectors (see 4 in fig. 3.2.0.) allowed for precise position control and focusing of the signal on the detector chip. Both detectors were connected by coaxial cables of equal length (2 m) to channels 0 and 1 of the TCSPC unit. An additional band pass filter (Thorlabs FES0650) was inserted on one of the detectors in order to remove the afterpulsing effect (a Si diode reemits light, once an incoming photon is detected, which can be detected by the second detector and cause a distortion in the acquired data). Afterpulsing effect is a common issue for semiconductor diodes and is due to the filling of deep level states by avalanche-created charges and its consequent reemission after a characteristic time. For Si based diodes the afterpulsing probability varies typically up to 10 % and decay times from 1 ns to 1 μs. This effect can be detected by illuminating the APDs with white light and measuring photon correlation between the two detectors. The insertion of the bandpass filter together with a slight tilt of the collimating lens resulted in the complete suppression of counts coming from afterpulsing. For more detailed technical data of the detectors used see table 3.1.1.

The photon correlation measurements were performed in time-tagging time-resolved (TTTR) T2 mode *[Wah 2007]*. In this mode photon arrivals are stored as separated events. Additionally a time-tagging is performed on each event with respect to the experiment start time. Both channels of the TCSPC unit are treated equally and their events are recorded independently. Each event record contains information about the arrival time since the experiment start time and the arrival channel. Thus dead times, which exist only within each channel but not across them, are no longer a problem for the correlation measurements.

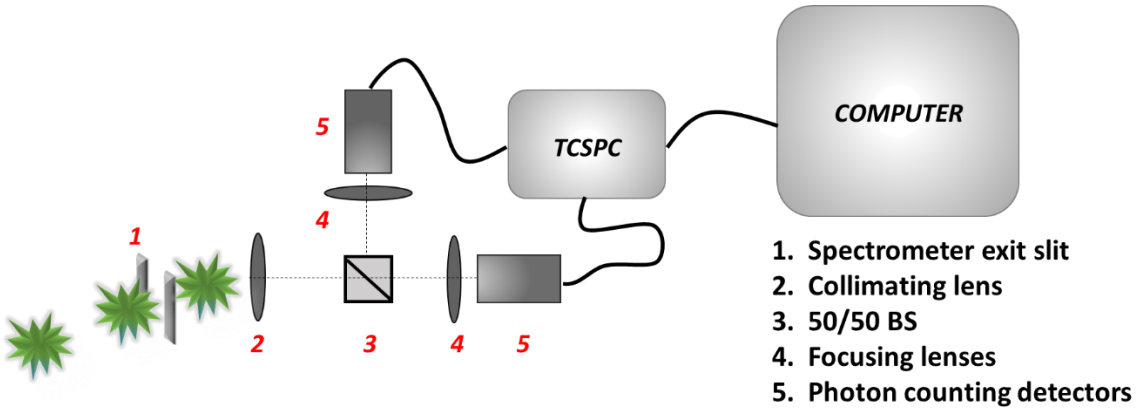

Fig. 3.2.0. A schematic of the HBT setup. For TRPL only one photon counting detector was used and the BS was removed.

3.3 STROBOSCOPIC TECHNIQUES

For the experiments with the SAW a similar cryostat was used, but equipped with additional electrical inputs to bring the RF signal to the sample. A special sample holder was designed and made at the UAM workshop. It consisted of a chip holder with 8 pins (4 on each side) which were connected to the electrical inputs of the cryostat (fig. 3.3.0.).The sample was glued with silver paste to the metal plate in the middle of the chip to ensure a good thermal contact. Bonding of the IDT pads to the chip metal pads was done by Mrs. M.C. Sabido Siller at *ISOM-UPM*. The bonding scheme is presented in fig. 3.3.0.(a).

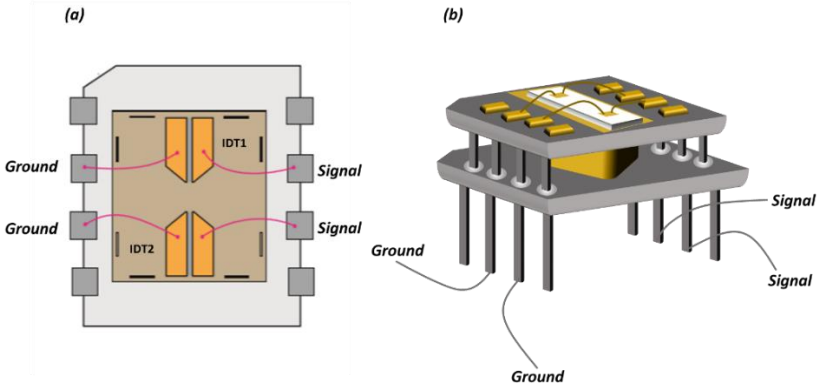

Fig. 3.3.0. Schematics of the sample mount and bonding (a) top view (b) side view.

A preliminary optical characterization was done in the same μ-PL setup as in Section 3.1.1. The cryostat was connected to the RF output of the radio-frequency generator through the amplifier and step attenuator connected by coaxial cables. The latter allowed to perform RF power dependence measurements with 1 dBm step without the need of changing settings of the RF generator itself, which was crucial for the maintenance of stable synchronization between the laser source and the SAW (see Section 3.3.1.). It is important to note, that the output signal from the RF generator is calibrated only until 13 dBm (according to its specifications). Thus, strictly

speaking values above that level cannot be correctly converted to volts or watts by using the conventional formulas:

$$V_{P_V} = 10^{\frac{P_{dBm}-10}{20}}, \quad \textbf{3.3.0.}$$

$$P_{mW} = 1mW \times 10^{\frac{P_{dBm}}{10}}, \quad \textbf{3.3.1.}$$

where V_{P_V} is the peak voltage in volts, P_{dBm} is the power in dBm and P_{mW} is the power in mW. These conversions are valid for the case of a sine wave in a 50 Ω impedance matched system. Thus, the use of the amplifier with the fixed amplification value of 23 dBm allowed to widen the calibrated range of the RF generator.

The performance of the IDTs was monitored by a Vector Network Analyzer (Rohde & Schwarz ZND 100348). It allowed to measure the *S*-parameters for each IDT and thus, the exact resonance frequency at room and low temperature were obtained.

3.3.1 Stroboscopic excitation

The stroboscopic excitation technique allowed to excite a chosen nanowire at a precise phase of the SAW cycle. A pulsed diode laser with wavelength 442 nm was used as an excitation source. The synchronization setup is presented in fig. 3.3.1. The RF output of RF generator (see 1 in fig. 3.3.1.(b)) was connected to the source input of the power splitter (see 2 in fig. 3.3.1.(b)). Its two outputs deliver the same electrical signal reduced by roughly 3 dBm with respect to the input signal (half of the input power). One output was connected to the cryostat, while the other to the laser controller. The initial amplitude of the acoustic signal was fixed and set by the RF generator to 12 dBm as a maximum allowed by the input power limits of all other electrical components and sufficient to produce a stable synchronization pulse. This value is also inside the RF generator calibration range, thus allowing correct dBm to W or V conversion. The attenuator with the fixed attenuation level of 10 dBm (see 3 in fig. 3.3.1.(b)) was inserted in the cryostat arm before the amplifier (see 4 in fig. 3.3.1.(b)) and the step attenuator (see 5 in fig. 3.3.1.(b)) in order not to exheed the input power limit of the IDTs as well as of the amplifier itself.

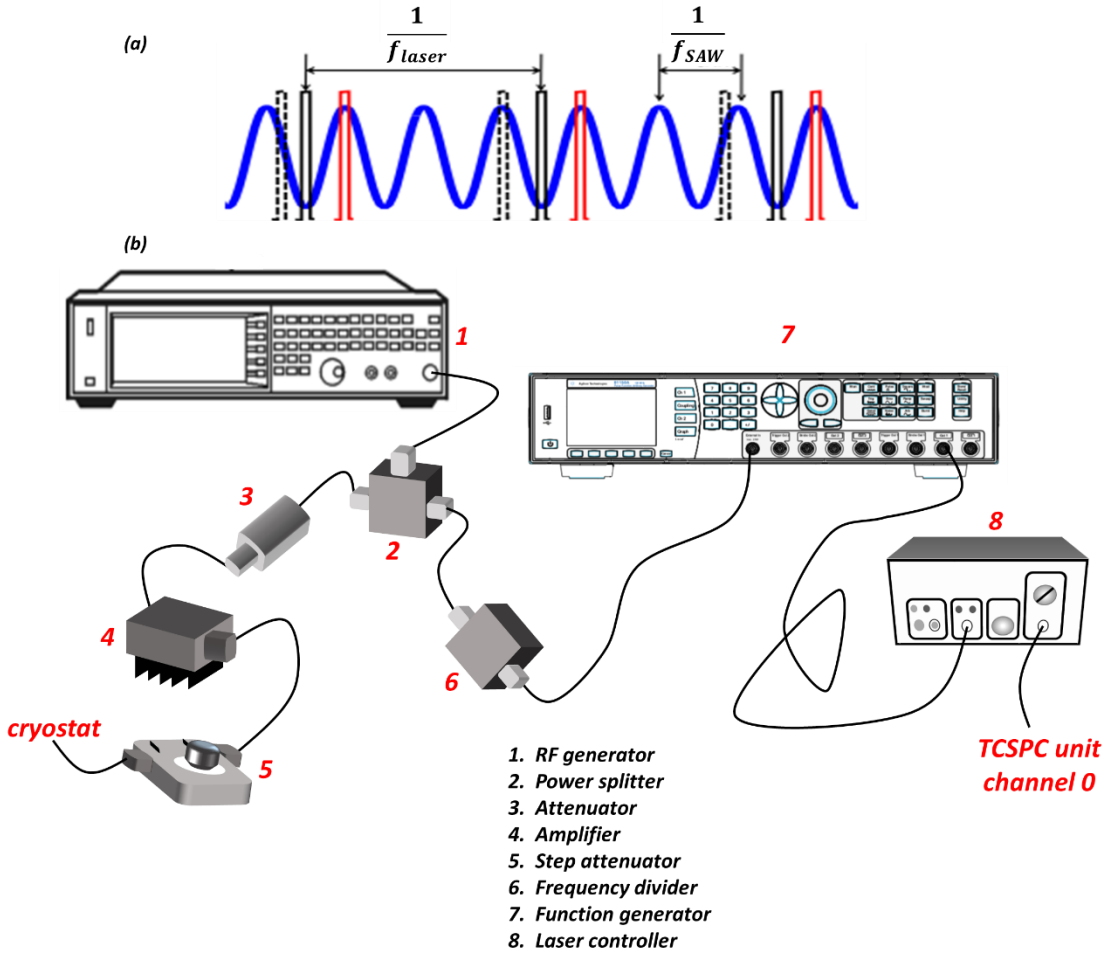

Fig. 3.3.1. (a) A scheme of SAW (solid blue) and laser pulses (solid black) locking. Red and black rectangles represent laser locking at 0 and π SAW phase, while dashed rectangles stand for random (averaged) phases **[Vol 2011]**. *(b) Block diagram of the synchronization setup.*

Since the RF generator used in this Thesis produced only a sine waveform, while the laser controller only accepted a square signal (TTL-like) with specific width and amplitude as an external reference, it became necessary to introduce a function generator (see 7 in fig. 3.3.1.(b)). It was connected to the second output of the power splitter through the frequency divider (see 6 in fig. 3.3.1.(b)). The purpose of the latter was to match the RF frequency range (usually hundreds of MHz) to the external input of the function generator (up to 120 MHz). In this way a square signal with adjustable amplitude and width was produced on the output of the function generator. Finally it was connected to the external trigger input of the laser controller box (see 8 in fig. 3.3.1.(b)) by means of the coaxial cable. More detailed specifications of each component and their technical parameters can be found in tables 3.3.0. and 3.3.1., respectively. Additionally the function generator was provided with the option to tune the delay between the input acoustic signal and the output laser trigger, thus allowing to control the excitation time within the acoustic period with minimum step of 1 ps.

In time-averaged detection the synchronization of the laser and the SAW allowed to obtain the spectral variation of the emission as a function of the SAW phase. In TRPL experiments an electrical signal provided by the laser controller is connected to Chanel 0 input and is used to trigger for the TCSPC unit, thus allowing to measure decays for a fixed excitation phase and detection wavelength.

Experimental component	**Company**	**Specifications**
RF generator	Keysight EXG Analog Signal Generator N5171B	9kHz-3GHz; Impedance matched to 50Ω; Output connector type N female; Amplitude range -144 dBm - +30 dBm; Output signal form sine wave;
Power splitter	Mini-Circuits ZFSC-2-11-S+	10 – 2000 MHz; Maximum input power 1 W;
Attenuator	Mini-Circuits BW-S10W2+	1 – 18000 MHz; Maximum input power 2 W; Fixed attenuation of 10 dBm;
Attenuator/inverter	PicoQuant SIA400	Fixed attenuation of 20 dBm; Inverts signal TTL to NIM;
Amplifier	Mini-Circuits ZFL-2500VH+	10 - 2500 MHz; Maximum input power +10 dBm; Maximum output power +23 dBm; Input voltage range 12 - 16 V; Maximum input current 300 mA;
Step attenuator	Fairview Microwave FMAT4004	1 – 2700 GHz; Maximum input power 2 W; Attenuation range 1 – 31 dBm with step 1 dBm;
Frequency divider	RF Bay Inc. FPS-8-18	0.2 – 18 GHz; Input power range for 0.2 – 2 GHz +3 dBm - +10 dBm; Typical output power -4 dBm; Input voltage range 7 - 12 V; Typical input current 105 mA; Fixed divide ratio 8;
Function generator	Keysight, Pulse Function Arbitrary Generator 81150A	Pulse generation with 1µHz - 120 MHz; External Input limits ±15 V;
RF cables	Thorlabs CA2948	

	CA2848	Length 1.2 m, connector type SMA – SMA; Length 1,2 m, connector SMA – BNC;

Table 3.3.0. Specifications of all electrical components used for the acoustical experiments.

Electrical component	**Technical parameters**
Amplifier	12 V, 200 mA;
Frequency divider	12 V, 105 mA;
Function generator	External In: Threshold 0 V, Impedance 50 Ω, Triggered pulse; Triggered pulse: External In, Rising edge, TTL, TTL; External Trigger: Patt Mode off, Delay adjustable, Width 15 ns, Lead edge=Trail edge=16.7%, Amplitude 1 Vpp, Offset 0 Vdc, Load Impedance=Output Impedance=50 Ω, Polarity normal;

Table 3.3.1. Technical parameters for amplifier, frequency divider and function generator.

3.3.2 Stroboscopic detection

The stroboscopic detection technique was quite similar to the stroboscopic excitation. Only now an independent cw excitation was used and the synchronization was established between SAW and TCSPC unit. In other words the counter started on receiving the reference signal from the RF generator and stopped on receiving photons. Chanel 0 input of the TCSPC was synchronized with SAW in the way described in the previous section, through the pulsed laser controller. By choosing an appropriate width of the spectrometer exit slit and grating position one obtained an oscillation of the emission intensity for a given wavelength in time, as a result of the SAW action.

3.4 THE IDTS PERFORMANCE

In order to correctly evaluate the IDTs performance it is necessary to take into account the changes in the signal, produced by all electronic components used in the setup. The most common procedure consists of measuring different types of calibration standards and comparing the results with corresponding ideal responses. The difference estimated in this way is used to correct for the system errors according to the chosen model (calibration type). These correction factors are then used to correct the measured data from the real device.

There are four commonly used standards: Open, Short, Through and Match (Load) circuits. For correction of reflection S-parameters the Open and Short standards are used. They are used to compensate for errors due to reflections. The transmission S-parameters are corrected with a Through standard, which gives a transmission error term. And, finally, a Match standard is used to correct for the directivity error (how well the forward and reversed signal can be separated).

In our case the calibration of the vector network analyzer (VNA) and the cables was necessary. The full 2-port calibration was used, which effectively removes all system's errors from the measured data for a 2-port device in forward and reversed directions and for both reflection and transmission measurements. A homemade (at PDI) sample holder and a set of the calibration standards were specifically designed and depicted on fig. 3.3.0. The entire calibration procedure was done at room temperature.

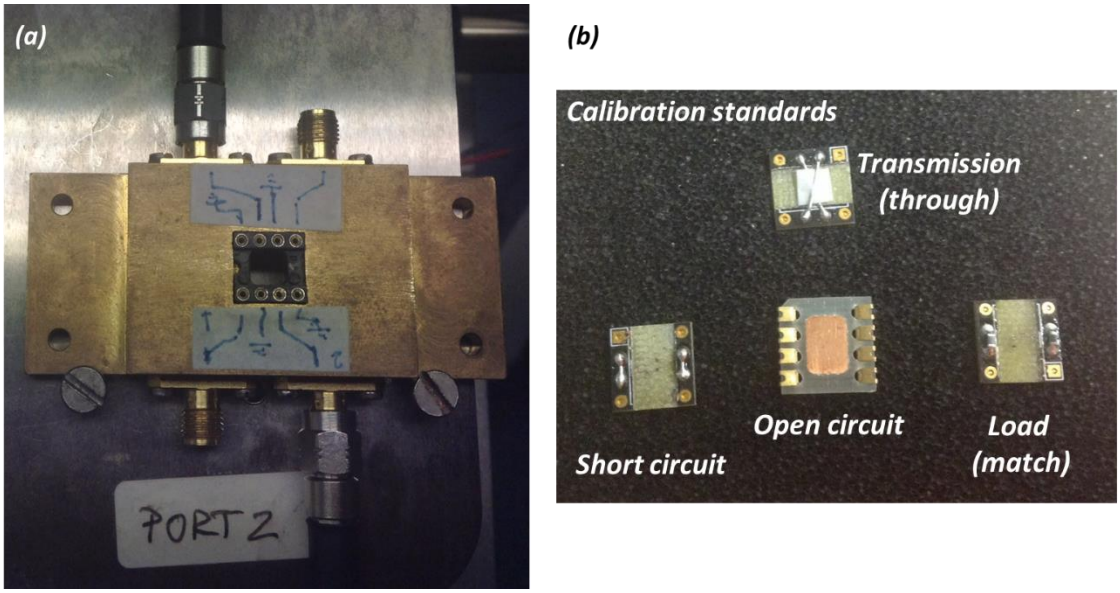

Fig. 3.4.0. (a) A photo of the handmade sample holder. (b) A set of handmade calibration standards for the sample holder in (a).

References

[Bec 2004] Becker, W., Bergmann, A., Biscotti, G. & Rueck, A. Advanced time-correlated single photon counting technique for spectroscopy and imaging of biological systems. *Proc. SPIE 5340, Commer. Biomed. Appl. Ultrafast Lasers IV, 104* **5340,** 1–9 (2004).

[Bec 2005] Becker, W. *Advanced Time-Correlated Single Photon Counting Techniques*. **81,** (Springer Berlin Heidelberg, 2005).

[PicoQ] *Time-Correlated Single Photon Counting System User's Manual and Technical Data*.

[Vol 2011] Völk, S., Knall, F., Schülein, F. J. R., Truong, T. A., Kim, H., Petroff, P. M., Wixforth, A. & Krenner, H. J. Direct observation of dynamic surface acoustic wave controlled

carrier injection into single quantum posts using phase-resolved optical spectroscopy. *Appl. Phys. Lett.* **98,** 23109 (2011).

[Wah 2007] Wahl, M., Rahn, H.-J., Gregor, I., Erdmann, R. & Enderlein, J. Dead-time optimized time-correlated photon counting instrument with synchronized, independent timing channels. *Rev. Sci. Instrum.* **78,** 33106 (2007).

[Wah 2009] Wahl, M. *Time-Correlated Single Photon Counting*. (2009).

4 CHAPTER. SINGLE PHOTON EMISSION FROM POLAR INGAN QUANTUM DOTS EMBEDDED IN GAN NANOWIRES

This chapter presents our results on optical properties of InGaN QDs inserted in GaN nanowires. The growth conditions and specific sample preparation will be addressed here. The detailed discussion of μ-PL measurements with time and polarization resolution will be presented. Also, cathodoluminescence experiments will give a structural overview, clarifying the spatial origin of the emitted light. The final objective is to show experimentally photon antibunching in the InGaN QDs inserted in GaN nanowires. Also estimations of the absorption cross-section and the exciton decay rate are given.

The QDs optical properties can vary due to the morphology and anisotropy of the confining potential. For many applications in quantum information processing the ability to produce highly polarized light, as well as to control the polarization degree is required. The easiest and most common solution is to pass unpolarized light through polarization filters and waveguides, resulting in inevitable efficiency losses. One way to reduce these losses is to employ an emission source, which directly generates photons with the desired polarization direction. Although, no perfect solution has been presented yet, several groups reported on attempts to control the QD polarization through prefabricated pyramidal *[Lun 2014; Edw 2004; Hsu 2011]* and nanowire templates *[Des 2013]* or with a dot–in–a–microcavity design *[Uni 2005]*. In the latter approach, the QD emission energy has to be tuned to match the cavity mode and thus the emission enhancement is restricted to the narrow bandwidth of the cavity resonance. Alternatively to this concept, the use of nanowires is very promising due to the light guiding effect, which operates in a broader spectral range than the cavity system.

An additional advantage of the dot-in-a-wire structure is that it allows an easy transfer of such heterostructures from their native substrate, which facilitates their posterior integration in photonic and optoelectronic devices.

4.1 SAMPLE DESCRIPTION

4.1.1 Growth of dot-in-a-wire structure

The samples under study were grown by Prof. Dr. E. Calleja's group *at Instituto de Sistemas Optoelectronicos y Microelectronica (ISOM) in Universidad Politecnica de Madrid (UPM)*. The plasma-assisted molecular-beam epitaxy (PAMBE) system, Riber Compact 21, used for growth was equipped with radio frequency plasma source providing active nitrogen and standard Knudsen cells for Ga and In. A thermocouple was used to monitor and control sample temperature. All samples were grown using nanohole titanium masks fabricated by colloidal lithography on (0001) GaN-on-sapphire templates. Details on the lithographic procedure can be

found in Ref. *[Ben 2012]* and a schematics is presented in fig. 4.1.0. In short, c-plane GaN templates were covered by a colloidal solution of polyestirene nanobeads by spin-coating. That resulted in large areas of closely-packed monolayer of nanobeads with rather uniform distribution. Then, oxygen plasma reactive ion etching was used to reduce the diameter of the nanobeads and, consequently, to isolate them. A Ti layer was evaporated followed by a lift-off process. That resulted in a hexagonally-ordered array of nanoholes (with ~200 nm diameter and ~270 nm pitch) on the Ti layer covering the GaN template. Prior to the growth process an additional nitridation step was performed to prevent the Ti mask from degradation at the high growth temperatures *[Kis 2009]*.

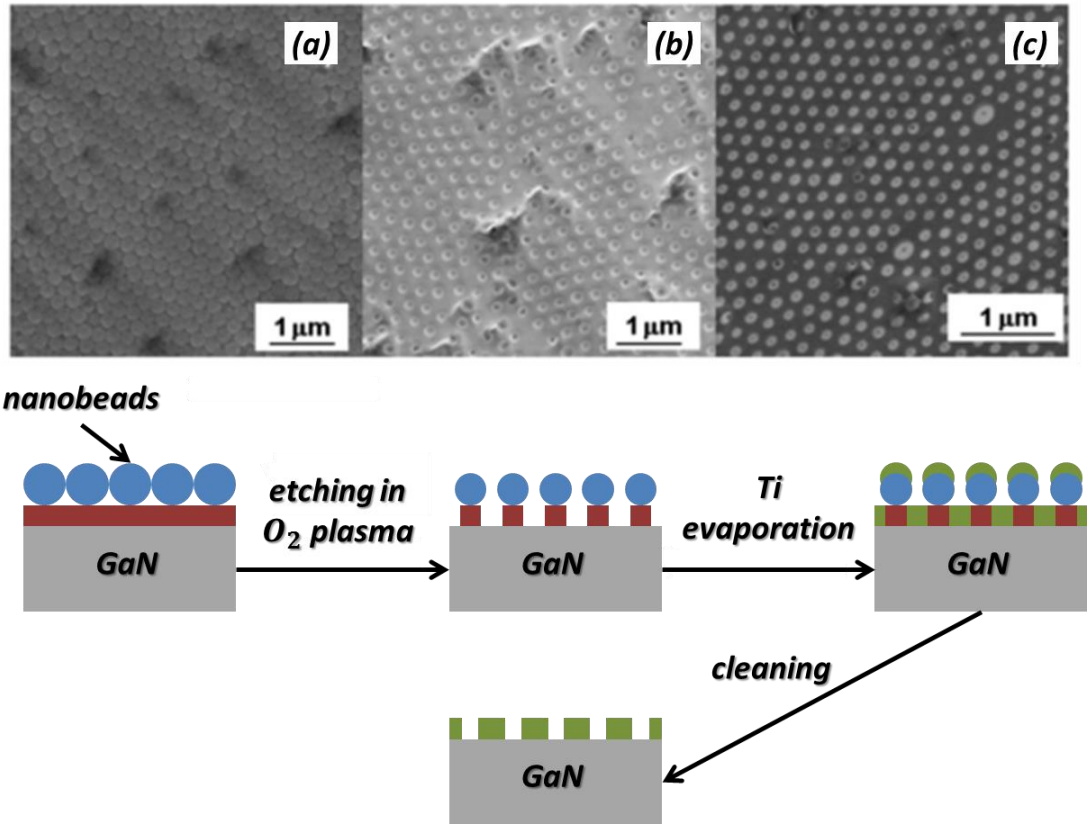

Fig. 4.1.0. Colloidal lithography procedure (lower panel). SEM images (upper panel) of the sample surface (a) with a layer of closely-packed nanobeads, (b) after plasma etching and (c) of the resulting Ti mask ***[Ben 2012]****.*

For the samples used in this Thesis, nanoholes were arranged into the lattice with an average pitch of ~ 280 nm, a diameter of ~ 200 nm and a density of ~ 1.6×10^9 cm^{-2}. Both pitch and diameter size can be easily controlled by changing the initial nanobeads size and etching time, respectively. The use of such mask resulted in selective area growth (SAG) of ordered arrays of high quality GaN nanowires *[Alb 2012]*.

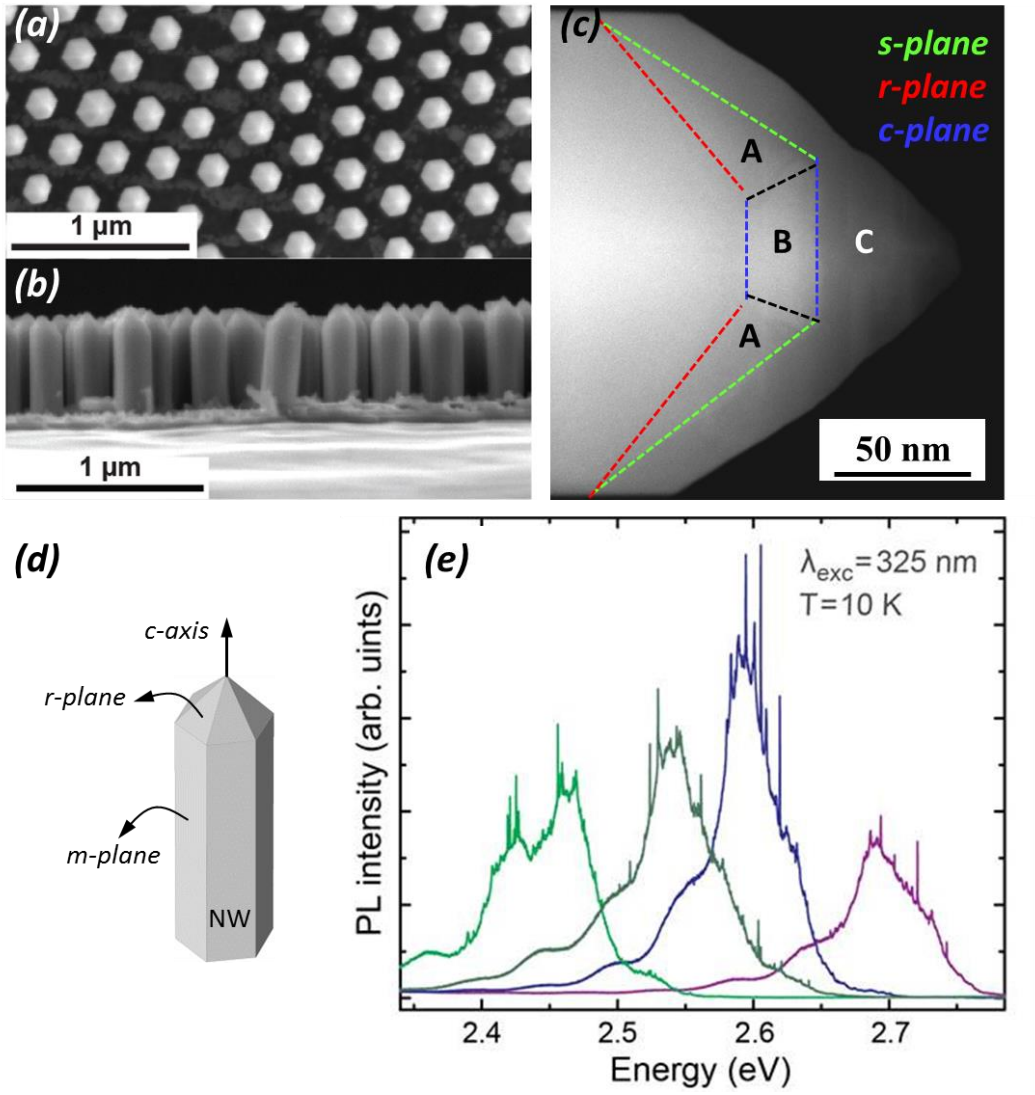

Fig. 4.1.1. Top (a) and side (b) SEM view of a representative sample area. (c) High resolution transmission electron microscope (HRTEM) image revealing the formation of the InGaN nanodisk with its peculiar shape together with the crystallographic planes (dashed lines) of the intra-wire interfaces. Letters "A" and "B" corresponds to the semi-polar and polar parts of the InGaN region respectively. Letter "C" – to the GaN capping. (d) Schematics of the single nanowire with the corresponding crystallographic planes. (e) PL spectra showing the tunability of the emission originated from the polar region of the InGaN inclusion for different growth conditions.

In the case of SAG on c-plane GaN templates the growth front is generally formed by semi-polar r-planes, yielding a hexagonal structure with a pencil-like top profile of the GaN nanowire. To allow for a better In incorporation the growth temperature for the InGaN nanodisk and final GaN capping was decreased. The resulting nanowires have a typical height of the order of 500 nm and a diameter of ~200 nm ***[Alb 2012]***. A scanning electron microscope (SEM) image of the as-grown sample, together with a cross-sectional scanning transmission electron microscope (STEM) bright field image of the single nanowire apex, revealing the InGaN inclusion is presented in fig. 4.1.1. The formation of the InGaN nanodisk (B) in the polar region at the top of the GaN nanowire with

higher In concentration, (~20%), and thickness, (~30 nm) is observed together with the semi-polar regions, (~10%) and (≤30 nm) (A) (fig. 4.1.1.(c)).

The light originating from the polar region of the InGaN inclusion can be tuned over the entire blue-to-green spectral region by varying the growth temperature and In flux (fig. 4.1.1.(e)) ***[Alb 2013; Laz 2015; Che 2015]***.

4.1.2 Sample preparation

For single nanowire spectroscopy, wires were mechanically removed from their native substrates and dispersed on a silicon wafer covered with a Ti metal mask patterned by electron-beam lithography. The mask layout was designed by Prof. Dr. S. Lazić using the Lasi7 computer software. It consists of enumerated arrays of square apertures of 3 µm x 3 µm and 4 µm x 4 µm in order to facilitate easy reassess to targeted nanowires (fig. 4.1.2. (a)).

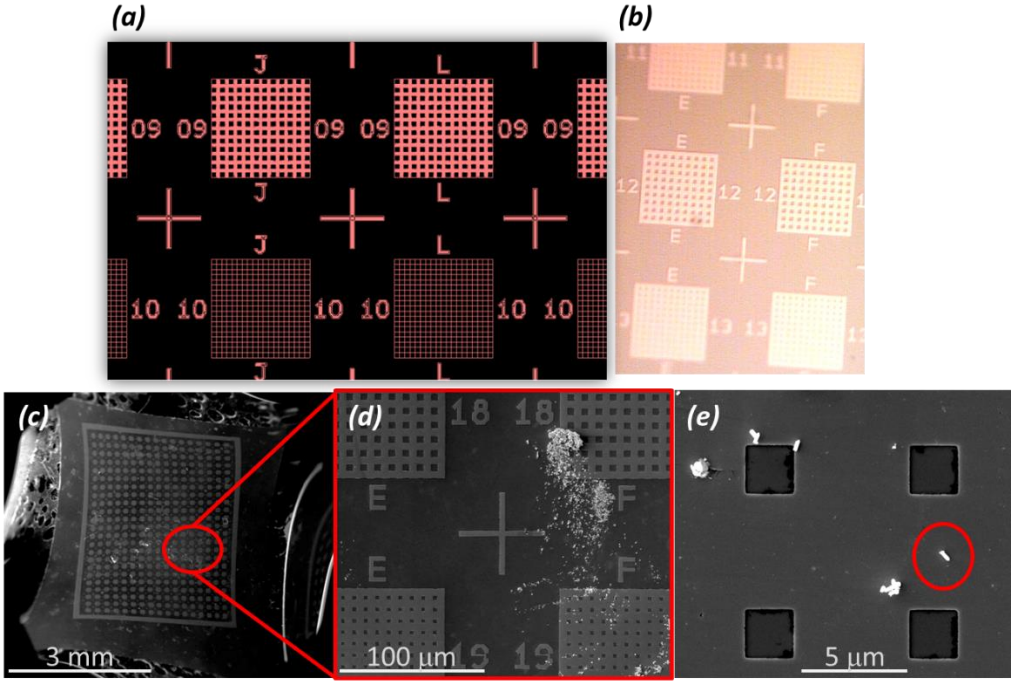

Fig. 4.1.2. (a) Mask layout designed in Lasi7 program. (b) A top view of the processed and cleaned metal mask in the optical microscope. (c) Top SEM view of a representative sample showing arrays of patterned metal grids. (d) Enlarged view of the Ti mask from (c) showing bunches of dispersed nanowires. (e) Low density of dispersed wires allows optical access to a single one. The red circle in (e) represents a typical detection area of ~3 µm².

For lithographic mask deposition, a CRESTEC CABL 9500 high resolution e-beam lithography system was used. A 0.5 µm PMMA (polymethyl methacrylate) resist was employed to cover the Si wafer, then a 50 nm titanium layer was deposited on the surface by an e-beam evaporator Varian VHC. Finally, the PMMA layer was removed resulting in the structure shown in fig.

4.1.2.(b). The lithographic processing was done by Mr. D. López-Romero Moraleda at the *ISOM UPM*.

The wires were scratched out of the as-grown sample onto the processed Si wafer. Such dispersion procedure resulted in nanowire bunches, forming rather conglomerates than separately lying wires. Nevertheless, in this way we were able to obtain occasionally low density of wires within the collection area (fig. 4.1.2.(d-e)), so as to perform single nanowire experiments.

4.2 OPTICAL CHARACTERIZATION

The initial task was to characterize the samples and look for QDs with the desired properties. That was achieved via optical spectroscopy (see Chapter 3 for more details on the experimental setup). The energy of photons emitted by the QDs is strongly dependent on the QD composition, size and shape. Hence the emission of the ensemble of QDs is a broad spectrum resulting from the superposition of the emission lines originated from different wires. Studying the spectral shape of a single QD emission and its excitation power and temperature dependence one can get an insight into the electronic states, as well as on the influence of the surrounding environment. Temporal resolution of the optical emission allows to study the recombination dynamics of the carriers involved.

After thoughtful characterization, only few QDs with the best spectral properties were chosen for photon correlation studies by HBT interferometry.

4.2.1 Cathodoluminescence

Low temperature spatially and spectrally resolved cathodoluminescence (CL) measurements of disk-in-a-wire heterostructures was done by Dr. M. Müller (from the group of Prof. Dr. J. Christen) at the *Otto-von-Guericke-University in Magdeburg, Germany*. This technique allowed to study simultaneously the structural and optical properties of these heterostructures on a nanometer scale. The CL unit was integrated in a FEI (S) TEM Tecnai F20 system equipped with a liquid helium stage, which allowed to make temperature dependent measurements in the range of 10 – 300 K. The emitted signal was directed through the retractable parabolic mirror to a grating monochromator (MonoCL4, Gatan). A liquid nitrogen cooled silicon CCD camera was used as a detector. A high-angle annular dark-field detector (HAADF from Fischione 3000) permitted to record the material contrast simultaneously to the detection of the CL-signal. The acceleration voltage was set to 80 kV to avoid sample damage.

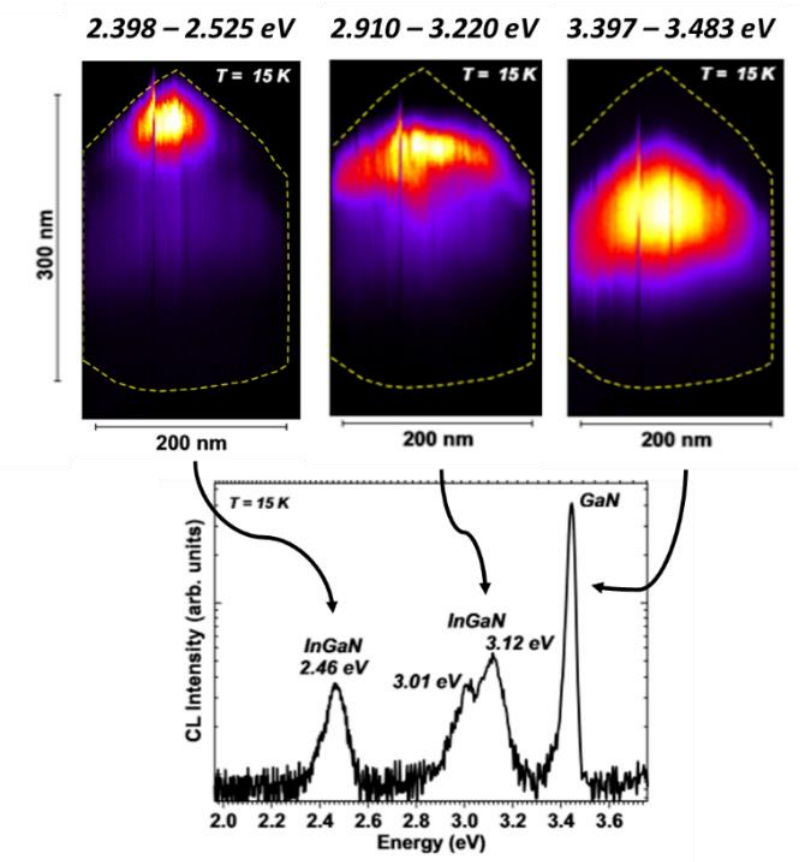

Fig. 4.2.0. Spatially resolved CL maps for selected spectral intervals of a single disk-in-a-wire structure (upper panels) and the corresponding CL spectrum (lower panel).

The low temperature CL mapping of individual disk-in-a-wire heterostructures revealed three distinct emission bands corresponding to near-band-edge luminescence originated from the GaN nanowire body (~3.4 eV) and the emission arising from the semi-polar (~3.1 eV) and polar (~2.5 eV) InGaN regions (fig. 4.2.0. upper panel). The corresponding CL-spectrum is shown in the lower panel of fig. 4.2.0.. The origin of the different energies observed will be addressed in details in the following sections.

The CL line scan, recorded at different NW heights, (fig. 4.2.1.) revealed the non-uniform distribution of In content for both polar and semi-polar parts of InGaN nanodisk. As would be discussed latter, the fluctuations of In concentration in polar region form QD-like confinement potentials manifesting themselves in the PL spectra as a sharp emission lines.

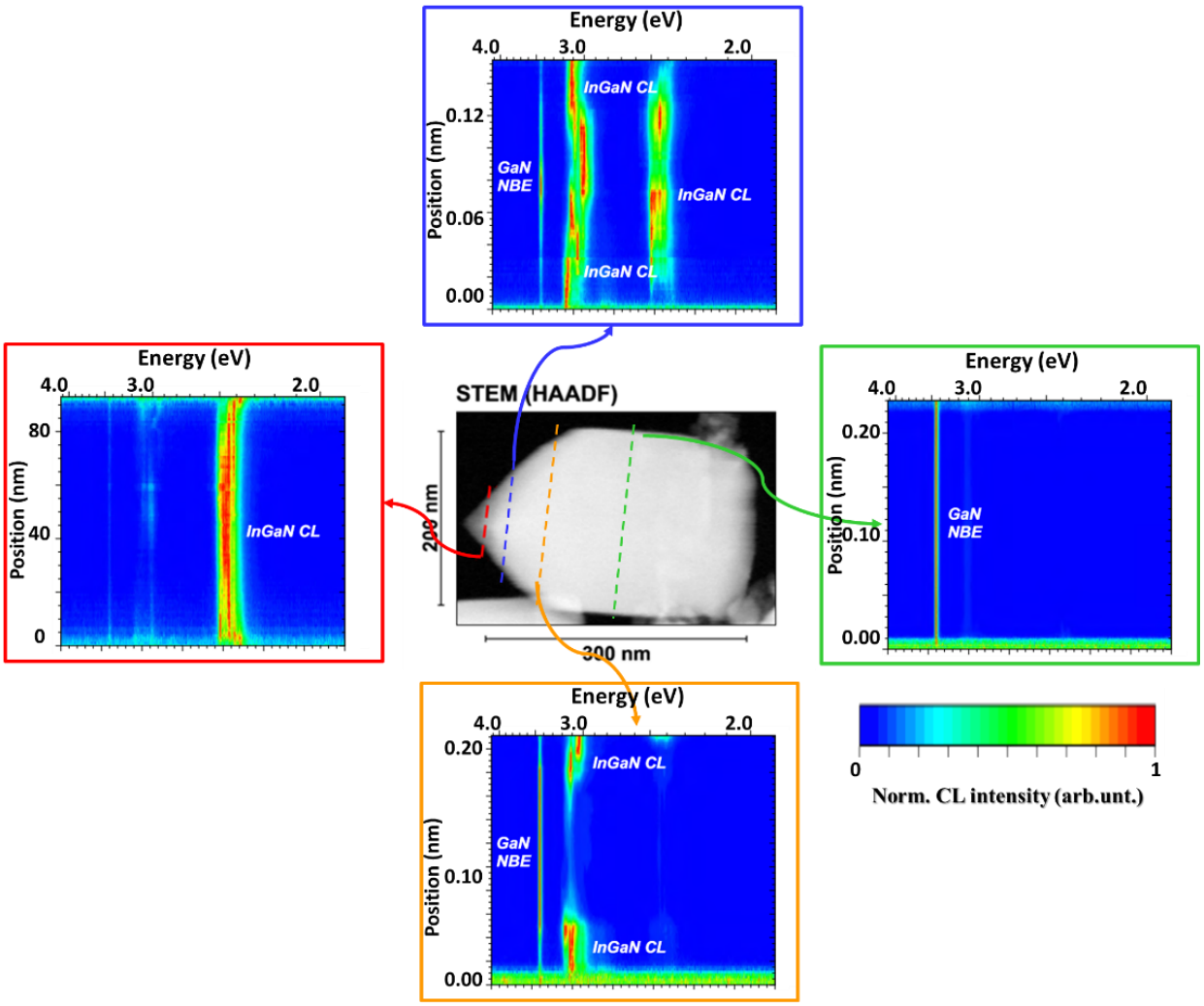

Fig. 4.2.1. CL scans recorded at different heights (colored dashed lines). GaN NBE stands for the GaN near-band-edge emission.

4.2.2 Micro-photoluminescence of as-grown and dispersed samples

The low temperature µ-PL measurements under cw UV excitation of the as-grown sample reveal emission from GaN nanowire body centered roughly at 3.40 eV and two emission bands from the InGaN inclusion, centered at 2.50 eV for polar and at 3.06 eV for semi-polar respectively (fig. 4.2.2.(a)). Thus µ-PL results are in good agreement with those obtained in the CL experiments. No yellow band emission was observed, contrary to what is typically reported for GaN-based systems. This is expected since the nanowire geometry provides better structural quality ***[Gac 2015]***. The observed sharp lines superimposed on the broad background emission were attributed to the formation of the quantum dot-like structures. The origin of these QDs is in the inhomogeneity of the InGaN layer resulting from the random fluctuations in composition (see fig. 4.2.1.). As a result, In-rich islands of different size are formed which eventually can localize carriers and excitons. The broad background emission is originated from the collective luminescence from the NW ensemble within the detection area. A similar behavior has been

reported for InGaN layers *[Hsu 2011; Jar 2007]*. Owing to the enhanced In incorporation on the polar region *[Das 2010; Gac 2016]*, as it was described in Section 4.1.1, the density and depth of optically active localization centers, as well as the disorder in size and composition are the highest there (fig. 4.2.2.(b)). Consequently, the sharp emission lines are resolved only there.

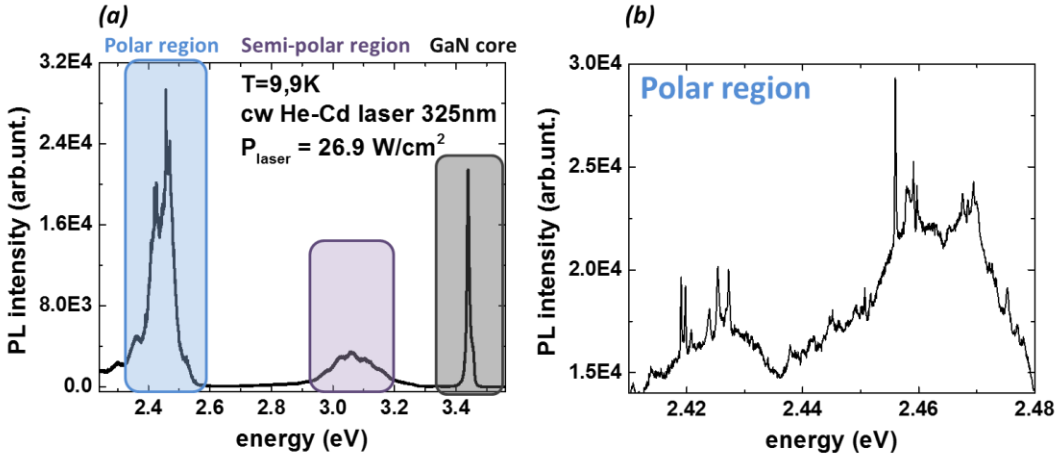

Fig. 4.2.2. Low temperature μ-PL spectrum under cw UV excitation of the as-grown sample (a). Enlarged portion of the μ-PL spectrum in (a) showing the emission from the polar region (b).

The variation of the emission energy originating from different parts of the InGaN inclusion can be explained in terms of differences in the In incorporation rate and electric fields in planes with different polarities. The internal electric field due to the spontaneous polarization, and therefore the surface charge density (σ) differs strongly for interfaces formed on polar, semi-polar and non-polar facets: $polar\ \sigma \gg semipolar\ \sigma > nonpolar\ \sigma = 0$. The modifications of the conduction and valence band profile induced by the internal electric field result in a significant spatial separation of electrons and holes *[Tak 1997; Gac 2016]*. This produces a marked QCSE leading to the reduction of emission energy (red shift), an increase of the emission lifetime and a relative intensity decrease. All QDs investigated in this Chapter were formed in the polar part of InGaN region.

The low temperature μ-PL of single isolated nanowires dispersed on the Si wafer showed similar results (fig. 4.2.3.). The background emission in the polar region is significantly reduced with respect to the as-grown sample and is due to the quantum well-like emission of the topmost InGaN section of the NW. The existence of more than one sharp emission lines in the spectrum for some single wires (fig. 4.2.3. left inset) confirms additionally that the formation of the QDs is a result of random fluctuations of In.

The full width half maximum (FWHM) of the emission lines varied from 350 μeV to 1 meV (fig. 4.2.4.(a)), in agreement with the values reported in the literature for self-assembled *[Kre 2012]* and ordered arrays of InGaN QDs *[Hsu 2011]*. Such small spectral widths are the sign of a good optical quality of the investigated emission centers. The FWHM can be increased by spectral diffusion *[Emp 1996; Jar 2007]*. Some groups also report on tendency for narrower linewidths for QDs with

higher emission energies (small QDs) *[Kin 2010]*. The suggested explanation is the weaker influence of QCSE for smaller QDs.

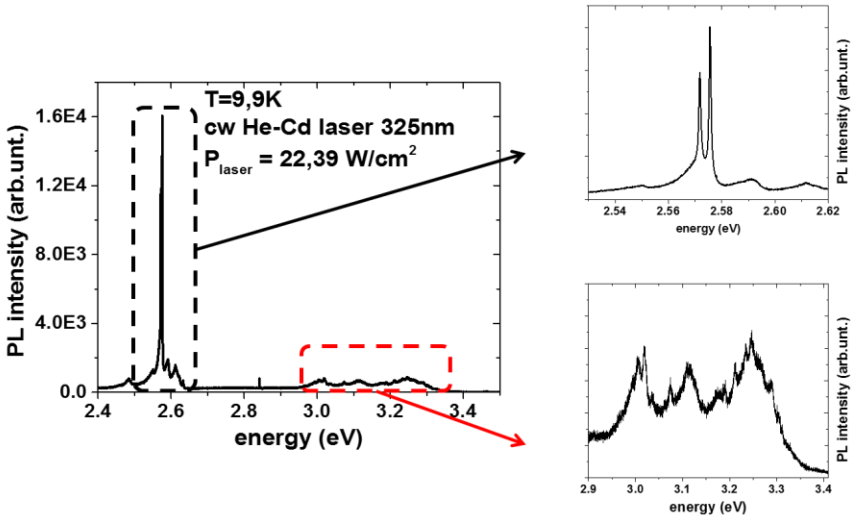

Fig. 4.2.3. Low temperature μ-PL spectrum of a single dispersed NW under cw UV excitation (right panel). Enlarged spectrum of polar (up) and semi-polar (down) regions (left panel).

In our case, no spectral diffusion or blinking effects were observed in the time scale of few minutes, but a small asymmetry in the red tail was seen in some QDs. The lack of spectral diffusion means that there were either few defects in the close proximity of the QD or their charging/discharging rate was in a larger time scale *[Jar 2007]*. Most of investigated QDs were typically detected at the high energy side of the collective spectrum, which is not always the case for ensembles of Nitride-based QDs *[Kin 2010]*.

Upon increasing the temperature, from 10 K to 55 K, the emission lines experienced a red-shift of ~1.28 meV (fig. 4.2.4.(b)), similar to the reported values from other InGaN QDs *[Hsu 2011; Oli 2003; Mor 2000]*. The linewidth roughly doubled with rising temperature, owing to exciton-acoustic phonon interactions *[Asa 1999]*, which is a characteristic feature of QDs *[Hsu 2011; Oli 2003; Mor 2000]*. For NW samples presented here, QD transitions were typically visible up to 80 K.

Most of the investigated single wires showed a dominant intense peak (fig. 4.2.4.) with linear dependence of the integrated intensity on excitation power (not shown). We assigned these lines to exciton ground state transitions. In some cases a biexciton was detected with the corresponding quadratic dependence of the integrated intensity on optical power. Large negative values of biexciton binding energy, E_b^{XX}~20 meV, detected for some QDs, indicate strong confinement and are typical for GaN *[Aml 2011; Kin 2010]* and InGaN QDs *[Aml 2014; Jar 2007]*.

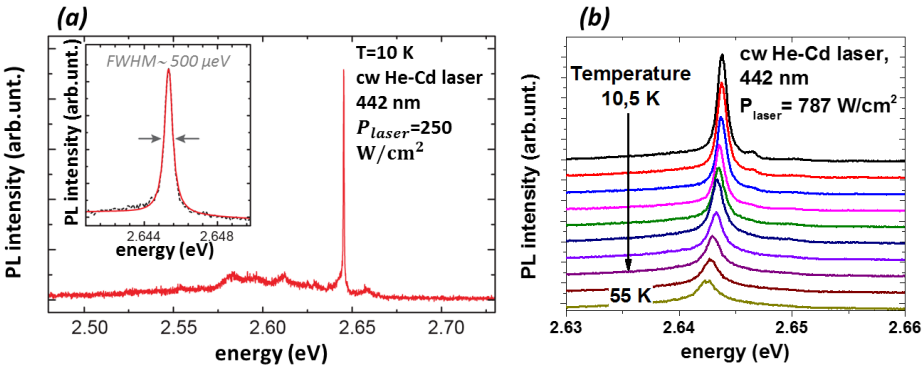

Fig. 4.2.4. Low temperature μ-PL spectrum of the polar part of a single InGaN nanodisk-in-a-wire (a) and its temperature dependence (b) under cw excitation at 442 nm.

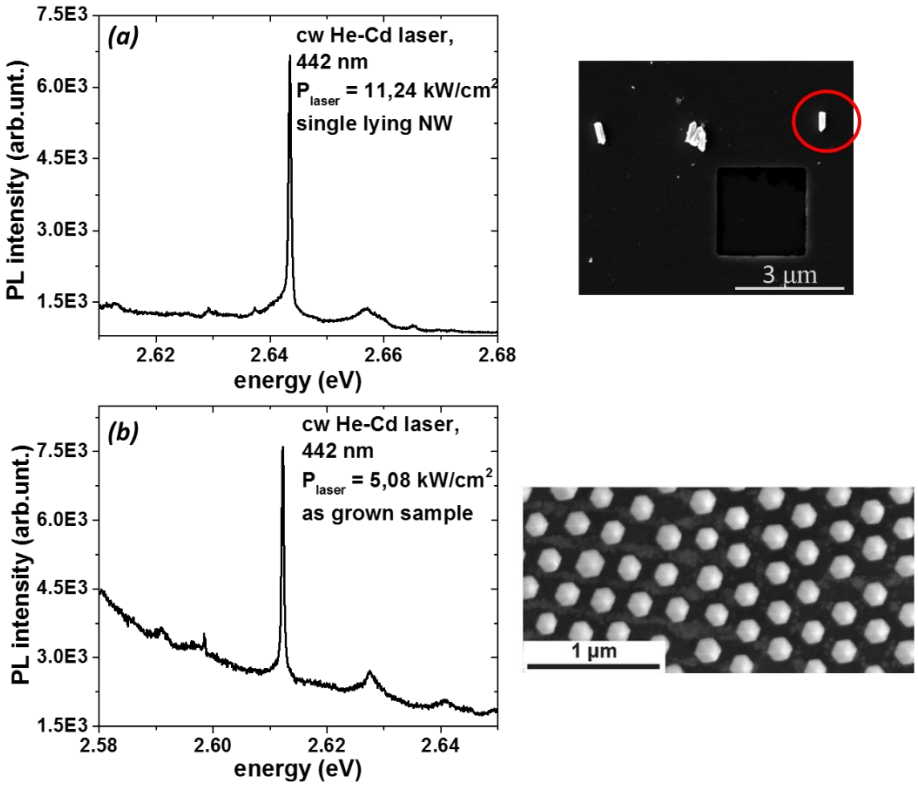

Fig. 4.2.5. Low temperature μ-PL spectra of a polar InGaN region from dispersed single wires (a) and as-grown sample (b) and their corresponding SEM images (right panels).

Owing to the dispersion process, wires fall on the Si plate randomly. Most of them were stacked in different lying positions. Thus we can compare the optical properties for two different positions of the NWs: (i) native, or standing, wires, (ii) dispersed, or lying, wires. The main limitation in the case (i) is a quite big number of neighboring NWs within the detection area, which not only gives much bigger "background" emission but also makes it difficult to determine whether or not all sharp peaks are coming from the same wire. For lying wires this problem is

almost eliminated. In fig. 4.2.5. examples for both cases are presented. One can note a significant increase of the "background" signal for the as-grown sample, as expected.

4.2.3 Polarization-resolved micro-photoluminescence

The polarization-resolved μ-PL was measured under similar conditions, as was described in the previous section. Since we focused now only on the polar region, the excitation was done with the cw 442 nm He-Cd laser. The integrated PL intensity was monitored while rotating the half-wave plate (see Chapter 3, fig. 3.1.0.) Examples of polarization plots for both as-grown and disperesed samples are presented in fig. 4.2.6.. The measured data was fitted with formula:

$$I(\theta) = Acos^2(\theta - \theta_0) + Bsin^2(\theta - \theta_0), \qquad \textbf{4.2.0.}$$

Assuming A>B the polarization degree can be written as:

$$P = \frac{A-B}{A+B}, \qquad \textbf{4.2.1.}$$

where $I(\theta)$ is the light intensity and θ_0 is the linear polarization angle of the corresponding QD line with respect to $\theta = 0$.

Most of the studied emission lines exhibited a high linear polarization degree, P ~ 90%, while the polarization angle was random. This means that there was no preferential direction for in-plane anisotropy, as expected for QD formed via random In fluctuations.

The strong linear polarization of Nitride based QDs, as it is commonly reported in the literature *[Aml 2013; Bar 2008; Kin 2010; Win 2007]*, is a signature of strong valence band mixing induced by in-plane anisotropy of the strain and/or the dot shape. Even a small magnitude of in-plane anisotropy in these QDs affects the oscillator strengths of the involved degenerate exciton states, resulting in the strong suppression of one of them. This suppression is clearly seen for the as-grown sample, where the light collected along the nanowire direction (c-axis) has almost full linear polarization, as shown in the bottom panel of fig. 4.2.6.

We conducted additional experiments with different linear polarization of the excitation source. The degree of polarization didn't change, showing that the spin of carriers is random after relaxation, as expected.

No fine structure splitting (FSS) was observed for any of the investigated QDs. This seems to be in contrast with the reported FSS values in small GaN/AlN QDs (up to 7 meV) *[Kin 2010]*. The absence of FSS in our case can be due to the fact that it is below our spectral resolution of 350 μeV. However, the most likely reason for the lack of FSS is the full linear polarization of the lowest energy emission due to the joint effects of electron-hole exchange interaction and in-plane anisotropy of strain and/or quantum dot shape *[Bar 2008]*, as explained in Chapter 2.

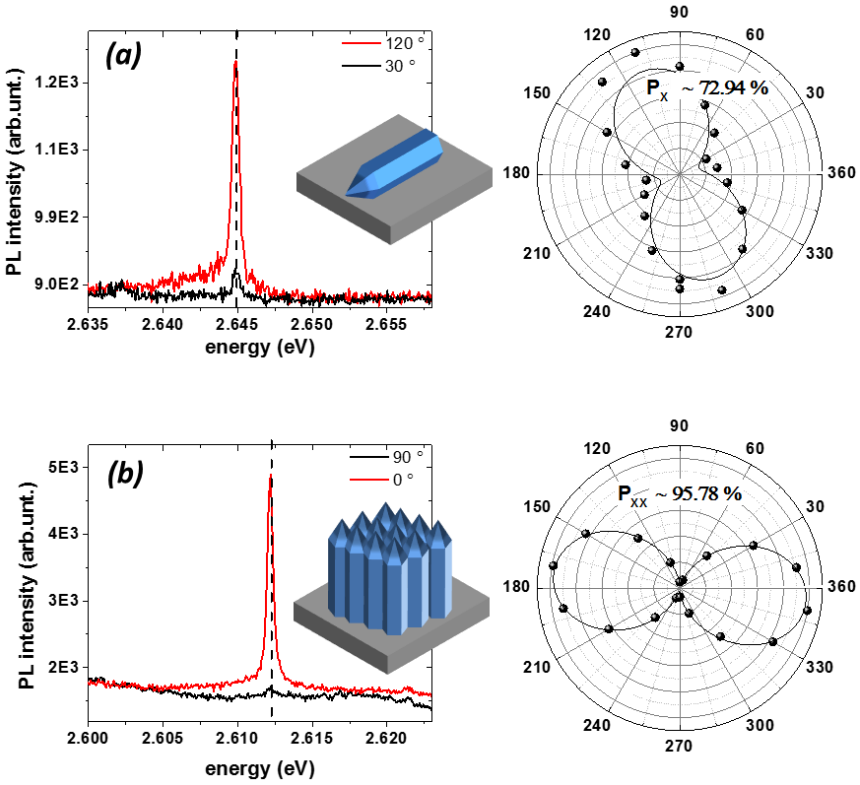

Fig. 4.2.6. Low temperature µ-PL spectra for dispersed (a) and as-grown (b) samples for two orthogonal polarizations (left panel) and their corresponding polar plots (right panel).

4.2.4 Time-resolved micro-photoluminescence

In order to gain information on the exciton dynamics in the InGaN QDs time-resolved measurements were conducted. The experimental conditions were similar to the µ-PL measurements, except for the pulsed laser excitation (see Chapter 3 for details on experimental setup) and the single channel (APD) detector. The exit slits were chosen as narrow as to select only a desired emission line and still have a sufficient signal-to-noise ratio. Only dispersed samples were subjected to this study to avoid the emission from QD-like centers as well as QW-like InGaN regions present in neighboring wires. Thus, for most of the QD-like emission lines from single wires we obtained monoexponential decays, corresponding to 3D confinement.

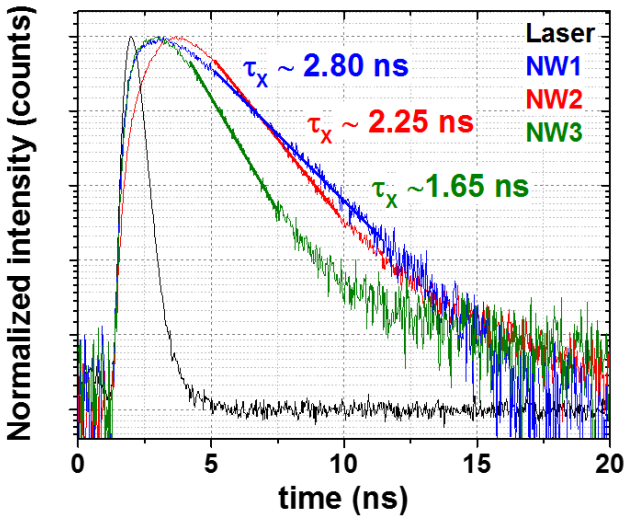

Fig. 4.2.7. TRPL decays for few dispersed NWs with the laser pulse as a reference.

The monoexponential fit resulted in time decay values ranging from 1 to 4 ns (fig. 4.2.7.) and is in agreement with typically reported values for InGaN QDs ***[Bar 2004; Win 2008; Rob 2003]***. The shift of the maximum intensity for NW2 of the order of 1 ns (fig. 4.2.7.) could be explained by the presence of biexcitons (XX) at the same emission center, which "refill" the exciton state upon recombination ***[Shi 2002]***. The recorded time transients for XX showed, indeed, decay times of the order of 1 ns. The rise times are limited by the resolution of our APD.

4.3 PHOTON CORRELATION MEASUREMENTS

An essential component in quantum information processing is a reliable and efficient single photon source (SPS). There are various schemes employed for the realization of such sources of non-classical light. Out of many, semiconductor QDs are of a particular interest, as it was already mentioned in Chapter 2, due to their size/shape-dependent optical properties, and, in the case of nitrides, the possibility of high temperature and high frequency operation (the latter in particular for non-polar QDs). In any two level system, once a photon is emitted, no more emission events are possible until the system is promoted to the excited state again. Thus, in the HBT histogram (see Chapter 2) there should be no detection events during some time after a photon is released. That will result in photon antibunching and will manifest itself as a dip in the histogram for zero time delay (see fig. 2.6.0.(c)). The mean photon coincidence rate will recover at some time delay (antibunching time), once the occupancy of the excited state will reach its steady-state value.

The presence of multi-excitonic states (especially biexcitons) in the QD depending on the excitation conditions and the recombination times have a direct impact on the dynamics of the X emission, leading to the different regimes of photon statistics. For pulsed excitation, a single

QD could be excited more than once per pulse, leading to a decrease of the antibunching depth, which is the important quantitative criterion to evaluate the performance of a single photon emitter.

4.3.1 Photon autocorrelation measurements

The single photon emission from the polar InGaN QDs was attested by HBT interferometry for both as grown and dispersed samples under cw optical excitation ($\lambda_{laser} = 442$ nm). After initial optical characterization, described in the previous sections, a few NWs were chosen to study their photon statistics. The second-order intensity correlation function measured with a time-bin of 32 ps is presented in fig. 4.3.0.(b,d) for as-grown and dispersed samples at the onset of saturation regime. Typically, the FWHM of the targeted peak varied from 8 to 12 pixels, which puts a limit on the width of the spectrometer exit slit from 200 µm to 300 µm. A particular difficulty for the as-grown sample was the strong influence of the background photons (fig. 4.3.0. (a)) originated from residual QW-like emission from the same wire as well as from neighboring NWs. The laser power regime was carefully chosen so to reduce the background emission while still collecting enough QD signal. The measured histogram was normalized to the coincidence rate of completely uncorrelated photons. The latter is the averaged value of coincidence counts for long time delays. To account for the finite time resolution of our setup it was necessary to introduce an instrument response function (IRF) as *[Rei 2008]*:

$$h(\tau) = C \cdot e^{-|\tau/\tau_{IRF}|}, \qquad \textbf{4.3.0.}$$

where C is a normalization factor and $\tau_{IRF} = 350\,ps$ is a temporal resolution of APDs. The second-order correlation function for cw excitation can be written as *[Bec 2001]*:

$$g^{(2)}(\tau) = 1 - \beta \cdot e^{-|\tau/\tau_R|}, \qquad \textbf{4.3.1.}$$

where β is the value of the antibunching dip and τ_R is the antibunching time constant.

The measured curve was fitted by the convolution of the IRF and $g^{(2)}(\tau)$, following the procedure, described in Refs. *[Bec 2001; Kim 2005; Rei 2008]*:

$$g^{(2)}_{meas}(\tau) = \int_{-\infty}^{\infty} h(\tau - \tau')g^{(2)}(\tau')d\tau' = 1 - \beta * \left[\frac{t^2{}_R * t_{IRF}}{t^2{}_{IRF} - t^2{}_R} * \left(\frac{1}{t_R} * e^{\frac{-|t|}{t_{IRF}}} - \frac{1}{t_{IRF}} * e^{\frac{-|t|}{t_R}}\right)\right], \qquad \textbf{4.3.2.}$$

The convolution was done with Wolfram Mathematica v.8 program. The resulted fit is presented by red solid lines in fig. 4.3.0. (b,d) for both as-grown and dispersed samples.

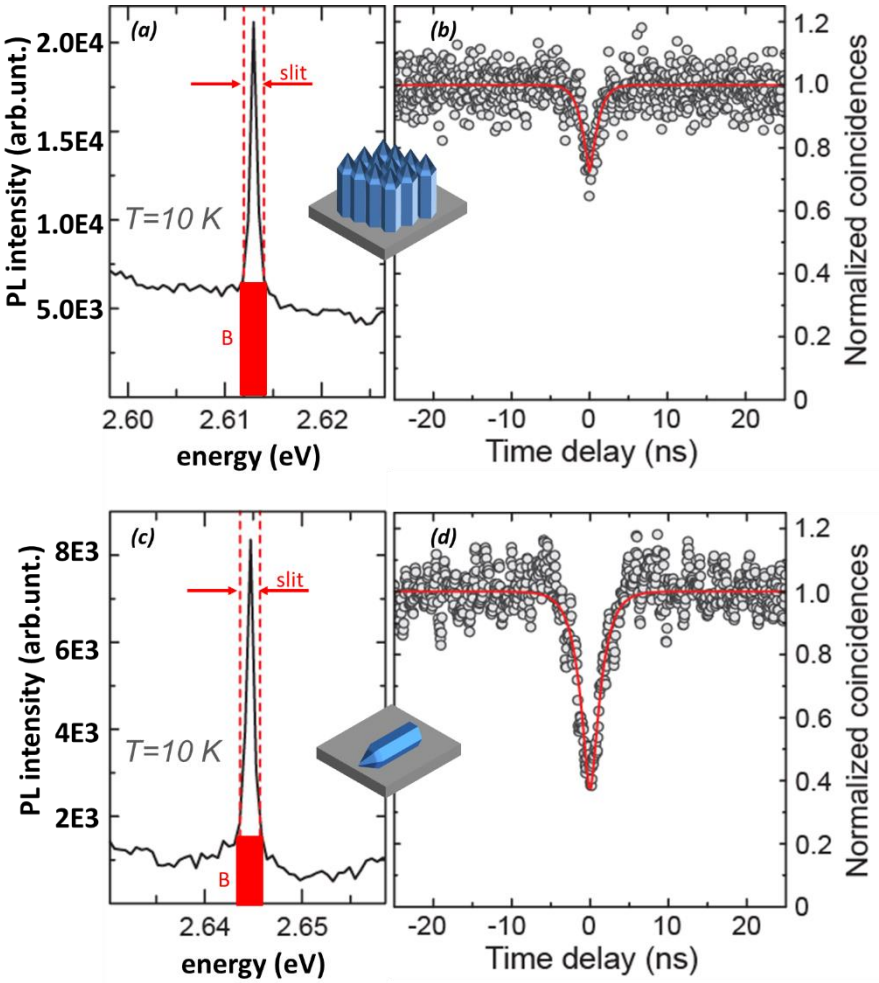

Fig. 4.3.0. μ-PL spectra of the as-grown (a) and dispersed (c) samples. The red rectangles represent the background level, denoted as "B". Dashed red lines show the spectral range selected by the exit slit of the spectrometer. (b,d) Normalized autocorrelation histograms for as-grown and dispersed sample, respectively. Red solid lines are a fit by the equation 4.3.2.

There is a clear dip in the correlation histograms for both samples, proving the non-classical nature of the emitted light. The values of the second-order correlation function at zero time delay, obtained from the fit were $g^{(2)}_{meas}(0) = 0.65 \pm 0.15$ and $g^{(2)}_{meas}(0) = 0.20 \pm 0.04$ for as-grown and dispersed samples, respectively. As mentioned before, the larger background in the as-grown sample can "spoil" the single photon performance by producing additional counts at zero time delays. Instead, for the single dispersed wire $g^{(2)}_{meas}(0)$ is already below the 0.5 threshold, corresponding to the simultaneous emission of two photons. To estimate the potential single photon performance in the absence of background we performed a background correction following the procedure from Refs. ***[Bro 2000; Bec 2001; Rei 2008]***, which strictly holds for uncorrelated background photons, flat background and cw excitation:

$$g^2_{corr}(0) = \frac{g^{(2)}_{meas}(0) - (1-\rho^2)}{\rho^2}, \qquad \textbf{4.3.3.}$$

where $\rho = S/(S+B)$ is the signal-to-total counts ratio, *S* stands for the signal counts and *B* for background counts. The value of ρ was determined from the spectra, presented in fig. 4.3.0.(a,c). An overview on the parameters, obtained from the fits is presented in table 4.3.0.

sample	$g^{(2)}_{meas}(0)$	$g^2_{corr}(0)$	t_R, ns	ρ
As-grown	0.65 ± 0.15	0.32 ± 0.15	0.96 ± 0.10	0.72
Dispersed	0.20 ± 0.04	0.06 ± 0.04	1.38 ± 0.06	0.92

Table 4.3.0. The resulted values from the fitting, described in the text.

After the background correction for both samples the second-order correlation function at zero time delay is well below the 0.5 threshold. This gives an unambiguous proof that the investigated QDs are, indeed, single photon emitters. The deviation from the ideal SPSs can be almost entirely accounted for by the finite temporal resolution of the experimental setup and the presence of uncorrelated background photons. The large difference of $g^2_{corr}(0)$ between as-grown and dispersed wires could be due to the existence of some correlation between QD photons and background ones. Indeed, part of the background comes from the same region of the NW, so that some transitions producing background photons have to compete for the same photo-excited carriers as the QD photons. Also the non-flat background of the as-grown sample can result in an inadequate background correction. This issue can be overcome by increasing the pitch of the Ti mask, so the distance between wires would be bigger.

4.3.2 Exciton decay rate

Only the sample with single dispersed wires was studied in this section, since the closely packed as-grown sample a-priori may produce additional uncorrelated emission, thus hampering the estimation of $g^{(2)}(0)$.

In the present study the strong antibunching was also observed in the power saturation regime, showing that simultaneous two-photon emission was, indeed, unlikely for the given QD. The power dependent autocorrelation measurements under cw excitation allow to obtain the exciton emission lifetime, τ_x ***[Bec 2001]***. This information is encoded in the temporal width of the antibunching dip. For a dispersed single wire a series of HBT experiments for different excitation powers were performed (fig. 4.3.1.(a)). A decrease in the dip depth with increasing optical power can be observed in fig. 4.3.1.(a). The second-order correlation function is proportional to the probability ($p_1(\tau)$) to find the QD occupied with one electron-hole pair at time τ assuming that the dot was empty at zero time delay. The value of $p_1(\tau)$ can be found by solving the rate equitation ***[Bec 2001; Kim 2005]***. Taking into account that initially the QD was empty, it can be written as:

$$p_1(\tau) = \frac{\gamma}{\gamma+\frac{1}{\tau_x}}\left(1 - e^{-\left(\gamma+\frac{1}{\tau_x}\right)\tau}\right) \propto g^2(\tau), \qquad \textbf{4.3.4.}$$

where γ is the pumping rate. Hence, the antibunching rate can be described as a linear dependence of the decay rate and pumping rate:

$$\frac{1}{\tau_R} = \frac{1}{\tau_x} + \gamma, \qquad \textbf{4.3.5.}$$

where τ_R is the width of the antibunching dip. Thus, the linear extrapolation of the antibunching rate at vanishing pump power allows to determine the exciton decay rate, which in this case is 0.84 ± 0.10 ns^{-1} (fig. 4.3.1.(b)). The corresponding value of the emission lifetime is $\tau_x = 1.19 \pm 0.14$ ns, which is in a good agreement with direct measurements of the exciton lifetime by TRPL (fig. 4.3.1.(c)).

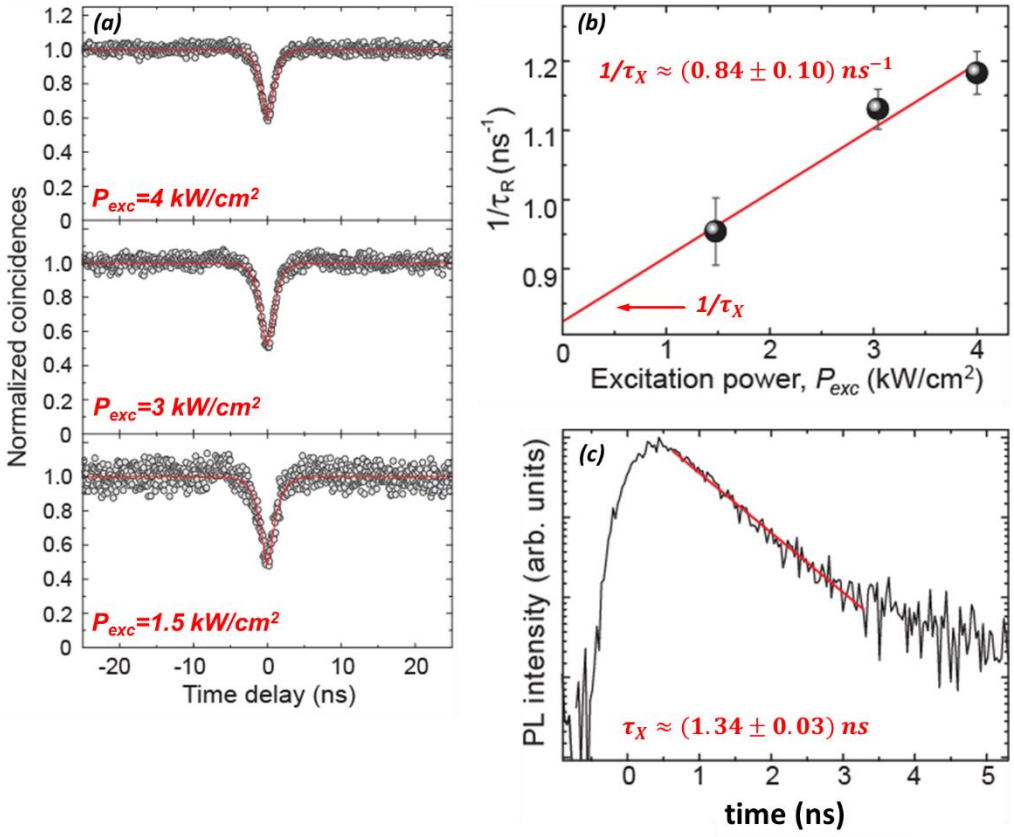

Fig. 4.3.1. Power dependent autocorrelation measurements (a) for a dispersed single NW-QD and corresponding antibunching rate as a function of optical pumping (b). TRPL spectrum of same NW-QD (c).

Such short exciton lifetime allow for high repetition rates (in the GHz range) of single photon emission, rendering this SPS useful for high frequency applications.

4.3.3 Absorption cross-section

Additionally, the absorption cross–section was determined from power dependent HBT measurements, following the procedure, developed in Ref. *[Lou 2000]*. The authors also described the QD photon statistics through the probability of finding it filled with one electron-hole pair, $p_1(\tau)$, using the rate equitation for cw excitation *[Efr 1997]*. As a result, the decay rate follows a linear trend $1/\tau_R = 1/\tau_x\,(1 + I/I_s)$ with the excitation intensity I. From the slope of the linear fit (red line in fig. 4.3.1.(b)) the fluorescence saturation intensity (I_s) was obtained. For the case of negligible two electron-hole population probability, as is the case for this QD, an equation for I_s can be written as:

$$I_s = \frac{h\nu}{\sigma\tau_X}, \qquad \textbf{4.3.6.}$$

where $h\nu$ is the excitation energy and σ is the absorption cross–section. In our case we find a value $\sigma = 1.7 \times 10^{-14}$ cm^2. The obtained value of the absorption cross–section is among the highest reported in the literature for quantum dots: $\sigma = 10^{-16} \div 10^{-14}$ cm^2 for CdSe QDs *[Lea 2002; Efr, 1997]* and $\sigma = 10^{-16}$ cm^2 for InAs QDs *[Osb 2004]*. The absorption cross-section is an important parameter for optical applications (i.e. solid state lightening), since it allows to determine the quantum efficiency of QDs.

4.4 SUMMARY

The optical properties of GaN nanowires with InGaN inclusions were investigated. It was shown that there are different emission bands from the InGaN part, originating from polar and semi-polar regions. This was also confirmed by spatially and spectrally resolved CL measurements. The origin of these bands was discussed in terms of In incorporation and differences in the electric field for the crystallographic planes with different polarities. Additionally, the emission from the polar part of the InGaN inclusion could be tuned over the entire blue-to-green spectral region by changing the growth parameters.

The sharp lines superimposed on the broad background were attributed to QD-like confinement potentials. The origin of such QDs is believed to be random In fluctuations, which results in the formation of In-rich islands with random size, shape and composition. Due to enhanced incorporation rate of In on the polar regions of the InGaN inclusions, the QD-like emission centers were detected only there. The optical spectroscopy was conducted in two geometries: as-grown or standing wires (i.e. conventional top-view geometry) and dispersed or lying wires (i.e. with optical path perpendicular to the NW axis). In the second case, the NWs were dispersed onto a Si wafer covered with a metal grid. In this way single NW spectroscopy was performed with a significant suppression of the background emission as compared to the as-grown sample.

Typical μ-PL spectra from the polar InGaN region from the dispersed sample showed narrow single emission lines proving the high optical quality of the emission centers. For some single wires more than one peak was observed in the spectra, proving that the origin of such QDs can indeed be attributed to In fluctuations. The FWHM of investigated sharp peaks was of the order of the values for InGaN QDs reported in literature. The QD emission was observed up to 80 K.

The polarization-resolved studies revealed a high degree of linear polarization for all investigated QDs. The polarization direction was found to be random, which is consistent with the fact that In fluctuations are at the origin of the QD formation mechanism. Such strong linear polarization is of the great importance for numerous applications in the field of quantum information processing (e.g. quantum key distribution and linear optical quantum computing). No FSS was observed for any of investigated QDs.

The emission lifetimes for all investigated QDs, measured directly by time-resolved μ-PL spectroscopy were of the order of 1 to 4 ns, which agreed well with the values reported in the literature for polar InGaN QDs.

The photon correlation experiments showed a pronounced antibunching for both as-grown and dispersed samples, showing antibunching dip values of 0.32 ± 0.15 and 0.06 ± 0.04, respectively. These values are below the 0.5 threshold for single photon emission, thus undoubtedly proving the single photon nature of the emitted light. After corrections for the finite time resolution of the experimental setup and for background photons the $g^2(0)$ value was almost zero for the dispersed sample, meaning that the deviation from the ideal SPS can be almost entirely accounted for the finite time resolution of the experimental setup and the contribution from the uncorrelated background emission, originating from the surrounding InGaN disk. For the case of the as-grown sample the influence of the additional background coming from the neighboring nanowires is still a major problem to produce true SPS.

The power dependent autocorrelation measurements under cw excitation for the dispersed single wire allowed to vary the antibunching time in the ns range and to obtain the exciton decay time, which coincides with the value measured by TRPL. Such single photon emitters are very attractive and desirable for high-frequency quantum information processing applications. Additionally the absorption cross-section was determined from the same series of excitation power-dependent autocorrelation experiments. The resulting value was comparable or higher than those reported for other QDs in literature.

Overall, the results of the present Chapter represent an important step towards the realization of an efficient single photon source based on nitride QDs. A high degree of linear polarization was observed and the possibility of operation up to GHz frequencies was demonstrated. The incorporation of such emitter into a SAG PAMBE grown nanowire geometry allows precise spatial control, which is important from the device-engineering point of view, as it allows the realization of arrays of SPSs on one substrate. Also these wires are easily removed from their native wafers,

which facilitates their integration with other components in on-chip photonic and optoelectronic devices. Such SPSs are not only desired for fundamental test of quantum mechanics, but also crucial for a variety of applications like: quantum metrology, quantum information processing and communication, quantum cryptography, linear optical quantum computing and quantum teleportation. The use of InGaN alloy further widens the operating spectral range of such emitter over the entire blue-to-green region.

4.5 FUTURE WORK

Firstly, improvement of the single photon performance of the as-grown sample is desired. The increasing of the pitch of the Ti mask will allow to increase the distance between the NW, facilitating the isolation of only one NW. In this way we are intending to suppress the background contribution from the neighboring NWs.

Second step is improvement of the operation range of the SPSs towards higher temperatures. That can be achieved by implementation of Al(Ga)N barriers. By increasing the band offsets the confinement can be also increased. In fact, most of the Nitride-based SPSs operating at high temperatures known nowadays were achieved in this way *[Des1 2013; Des2 2013; Hol 2014; Hol 2016]*.

Another possible step is to achieve a single QD per wire structure. That can be done by either decreasing the NW diameter *[Zha 2016; Sek 2010;; Des1 2013]* or by increasing the tapering angle of the NW tip. The latter approach also allows to improve the emission directionality *[Gre 2008]*.

References

[Alb 2012] Albert, S., Bengoechea-Encabo, A., Lefebvre, P., Barbagini, F., Sanchez-Garcia, M. A., Calleja, E., Jahn, U. & Trampert, A. Selective area growth and characterization of InGaN nano-disks implemented in GaN nanocolumns with different top morphologies. *Appl. Phys. Lett.* **100,** 231906 (2012).

[Alb 2013] Albert, S., Bengoechea-Encabo, A., Sánchez-García, M. A., Kong, X., Trampert, A. & Calleja, E. Selective area growth of In(Ga)N/GaN nanocolumns by molecular beam epitaxy on GaN-buffered Si(111): from ultraviolet to infrared emission. *Nanotechnology* **24,** 175303 (2013).

[Aml 2011] Amloy, S., Yu, K. H., Karlsson, K. F., Farivar, R., Andersson, T. G. & Holtz, P. O. Size dependent biexciton binding energies in GaN quantum dots. *Appl. Phys. Lett.* **99,** 251903 (2011).

[Aml 2013] Amloy, S., Karlsson, K. F. & Holtz, P. O. III-nitride based quantum dots for photon emission with controlled polarization switching. *arXiv:1311.573lvl [cond-mat.mes-hall]* 1–6 (2013).

[Aml 2014] Amloy, S., Karlsson, K. F., Eriksson, M. O., Palisaitis, J., Persson, P. O. Å., Chen, Y. T., Chen, K. H., Hsu, H. C., Hsiao, C. L., Chen, L. C. & Holtz, P. O. Excitons and biexcitons in InGaN quantum dot like localization centers. *Nanotechnology* **25,** 495702 (2014).

[Asa 1999] Asaoka, K., Ohno, Y., Kishimoto, S. & Mizutani, T. Microscopic Photoluminescence Study of InAs Single Quantum Dots Grown on (100) GaAs. *Japanese J. Appl. Physics, Part 1 Regul. Pap. Short Notes Rev. Pap.* **38,** 546–549 (1999).

[Bar 2004] Bartel, T., Dworzak, M., Strassburg, M., Hoffmann, A., Strittmatter, A. & Bimberg, D. Recombination dynamics of localized excitons in InGaN quantum dots. *Appl. Phys. Lett.* **85,** 1946–1948 (2004).

[Bar 2008] Bardoux, R., Guillet, T., Gil, B., Lefebvre, P., Bretagnon, T., Taliercio, T., Rousset, S. & Semond, F. Polarized emission from GaN/AlN quantum dots: Single-dot spectroscopy and symmetry-based theory. *Phys. Rev. B* **77,** 235315 (2008).

[Bec 2001] Becher, C., Kiraz, A., Michler, P., Imamoğlu, A., Schoenfeld, W. V., Petroff, P. M., Zhang, L. & Hu, E. Nonclassical radiation from a single self-assembled InAs quantum dot. *Phys. Rev. B* **63,** 121312 (2001).

[Ben 2012] Bengoechea-Encabo, A., Albert, S., Sanchez-Garcia, M. A., López, L. L., Estradé, S., Rebled, J. M., Peiró, F., Nataf, G., de Mierry, P., Zuniga-Perez, J. & Calleja, E. Selective area growth of a- and c-plane GaN nanocolumns by molecular beam epitaxy using colloidal nanolithography. *J. Cryst. Growth* **353,** 1–4 (2012).

[Bro 2000] Brouri, R., Beveratos, A., Poizat, J.-P. & Grangier, P. Photon antibunching in the fluorescence of individual color centers in diamond. *Opt. Lett.* **25,** 1294 (2000).

[Che 2015] Chernysheva, E., Gačević, Ž., García-Lepetit, N., van der Meulen, H. P., Müller, M., Bertram, F., Veit, P., Torres-Pardo, A., González Calbet, J. M., Christen, J., Calleja, E., Calleja, J. M. & Lazić, S. Blue-to-green single photons from InGaN/GaN dot-in-a-nanowire ordered arrays. *EPL (Europhysics Lett.* **111,** 24001 (2015).

[Das 2010] Das, A., Magalhães, S., Kotsar, Y., Kandaswamy, P. K., Gayral, B., Lorenz, K., Alves, E., Ruterana, P. & Monroy, E. Indium kinetics during the plasma-assisted molecular beam epitaxy of semi-polar (11-22) InGaN layers. *Appl. Phys. Lett.* **96,** (2010).

[Des 2013] Deshpande, S., Heo, J., Das, A. & Bhattacharya, P. Electrically driven polarized single-photon emission from an InGaN quantum dot in a GaN nanowire. *Nat. Commun.* **4,** 1675 (2013).

[Des1 2013] Deshpande, S. & Bhattacharya, P. An electrically driven quantum dot-in-nanowire visible single photon source operating up to 150 K. *Appl. Phys. Lett.* **103,** 241117 (2013).

[Des2 2013] Deshpande, S., Das, A. & Bhattacharya, P. Blue single photon emission up to 200 K from an InGaN quantum dot in AlGaN nanowire. *Appl. Phys. Lett.* **102,** 161114 (2013).

[Edw 2004] Edwards, P. R., Martin, R. W., Watson, I. M., Liu, C., Taylor, R. A., Rice, J. H., Na, J. H., Robinson, J. W. & Smith, J. D. Quantum dot emission from site-controlled InGaN/ GaN micropyramid arrays. *Appl. Phys. Lett.* **85,** 4281 (2004).

[Efr 1997] Efros, A. F. & Rosen, M. Random telegraph signal in the photoluminescence intensity of a single quantum dot. *Phys. Rev. Lett.* **78,** 1110–1113 (1997).

[Emp 1996] Empedocles, S. A., Norris, D. J. & Bawendi, M. G. Photoluminescence Spectroscopy of Single CdSe Nanocrystallite Quantum Dots. *Phys. Rev. Lett.* **77,** 3873–3876 (1996).

[Gac 2015] Gačević, Ž., Bengoechea-Encabo, A., Albert, S., Torres-Pardo, A., González-Calbet, J. M. & Calleja, E. Crystallographically uniform arrays of ordered (In)GaN nanocolumns. *J. Appl. Phys.* **117,** 35301 (2015).

[Gac 2016] Gačević, Ž., Vukmirović, N., García-Lepetit, N., Torres-Pardo, A., Müller, M., Metzner, S., Albert, S., Bengoechea-Encabo, A., Bertram, F., Veit, P., Christen, J., González-Calbet, J. M. & Calleja, E. Influence of composition, strain, and electric field anisotropy on different emission colors and recombination dynamics from InGaN nanodisks in pencil-like GaN nanowires. *Phys. Rev. B* **93,** 125436 (2016).

[Gre 2008] Gregersen, N., Nielsen, T. R., Claudon, J., Gérard, J.-M. & Mørk, J. Controlling the emission profile of a nanowire with a conical taper. *Opt. Lett.* **33,** 1693–1695 (2008).

[Hol 2014] Holmes, M. J., Choi, K., Kako, S., Arita, M. & Arakawa, Y. Room-temperature triggered single photon emission from a III-nitride site-controlled nanowire quantum dot. *Nano Lett.* **14,** 982–6 (2014).

[Hol 2016] Holmes, M. J., Kako, S., Choi, K., Arita, M. & Arakawa, Y. Single Photons from a Hot Solid-State Emitter at 350 K. *ACS Photonics* **3,** 543–546 (2016).

[Hsu 2011] Hsu, C.-W., Lundskog, A., Karlsson, K. F., Forsberg, U., Janzén, E. & Holtz, P. O. Single Excitons in InGaN Quantum Dots on GaN Pyramid Arrays. *Nano Lett.* **11,** 2415–2418 (2011).

[Jar 2007] Jarjour, A. F., Oliver, R. A. & Taylor, R. A. Progress in the optical studies of single InGaN/GaN quantum dots. *Philos. Mag.* **87,** 2077–2093 (2007).

[Kim 2005] Kimura, S., Kumano, H., Endo, M., Suemune, I., Yokoi, T., Sasakura, H., Adachi, S., Muto, S., Song, H. Z., Hirose, S. & Usuki, T. Photon Antibunching Observed from an InAlAs Single Quantum Dot. *Jpn. J. Appl. Phys.* **44,** L793–L796 (2005).

[Kin 2010] Kindel, C., Kako, S., Kawano, T., Oishi, H., Arakawa, Y., Hönig, G., Winkelnkemper, M., Schliwa, A., Hoffmann, A. & Bimberg, D. Exciton fine-structure splitting in GaN/AlN quantum dots. *Phys. Rev. B* **81,** 241309 (2010).

[Kis 2009] Kishino, K., Sekiguchi, H. & Kikuchi, A. Improved Ti-mask selective-area growth (SAG) by rf-plasma-assisted molecular beam epitaxy demonstrating extremely uniform GaN nanocolumn arrays. *J. Cryst. Growth* **311,** 2063–2068 (2009).

[Kre 2012] Kremling, S., Tessarek, C., Dartsch, H., Figge, S., Höfling, S., Worschech, L., Kruse, C., Hommel, D. & Forchel, A. Single photon emission from InGaN/GaN quantum dots up to 50 K. *Appl. Phys. Lett.* **100,** 61115 (2012).

[Laz 2015] Lazić, S., Chernysheva, E., Gačević, Ž., García-Lepetit, N., van der Meulen, H. P., Müller, M., Bertram, F., Veit, P., Christen, J., Torres-Pardo, A., González Calbet, J. M., Calleja, E. & Calleja, J. M. Ordered arrays of InGaN/GaN dot-in-a-wire nanostructures as single photon emitters. conf proceedings *SPIE* 93630U (2015).

[Lea 2002] Leatherdale, C. A., Woo, W. K., Mikulec, F. V & Bawendi, M. G. On the absorption cross section of CdSe nanocrystal quantum dots. *J. Phys. Chem. B* **106,** 7619–7622 (2002).

[Lou 2000] Lounis, B., Bechtel, H. A., Gerion, D., Alivisatos, P. & Moerner, W. E. Photon antibunching in single CdSe/ZnS quantum dot fluorescence. *Chem. Phys. Lett.* **329,** 399–404 (2000).

[Lun 2014] Lundskog, A., Hsu, C.-W., Fredrik Karlsson, K., Amloy, S., Nilsson, D., Forsberg, U., Olof Holtz, P. & Janzén, E. Direct generation of linearly polarized photon emission with designated orientations from site-controlled InGaN quantum dots. *Light Sci. Appl.* **3,** e139 (2014).

[Mor 2000] Moriwaki, O., Someya, T., Tachibana, K., Ishida, S. & Arakawa, Y. Narrow photoluminescence peaks from localized states in InGaN quantum dot structures. *Appl. Phys. Lett.* **76,** 2361 (2000).

[Oli 2003] Oliver, R. A., Briggs, G. A. D., Kappers, M. J., Humphreys, C. J., Yasin, S., Rice, J. H., Smith, J. D. & Taylor, R. A. InGaN quantum dots grown by metalorganic vapor phase epitaxy employing a post-growth nitrogen anneal. *Appl. Phys. Lett.* **83,** 755–757 (2003).

[Osb 2004] Osborne, S. W., Blood, P., Smowton, P. M., Xin, Y. C., Stintz, A., Huffaker, D. & Lester, L. F. Optical absorption cross section of quantum dots. *J. Phys. Condens. Matter* **16,** S3749–S3756 (2004).

[Rei 2008] Reischle, M., Beirne, G. J., Schulz, W.-M., Eichfelder, M., Roßbach, R., Jetter, M. & Michler, P. Electrically pumped single-photon emission in the visible spectral range up to 80 K. *Opt. Express* **16,** 12771 (2008).

[Rob 2003] Robinson, J. W., Rice, J. H., Jarjour, A., Smith, J. D., Taylor, R. A., Oliver, R. A., Briggs, G. A. D., Kappers, M. J., Humphreys, C. J. & Arakawa, Y. Time-resolved dynamics in single InGaN quantum dots. *Appl. Phys. Lett.* **83,** 2674 (2003).

[Shi 2002] Shields, A. J., Stevenson, R. M., Thompson, R. M., Yuan, Z. & Kardynal, B. E. chapter in *Nano-Physics Bio-Electronics A New Odyssey* 111–146 (Elsevier, 2002).

[Sek 2010] Sekiguchi, H., Kishino, K. & Kikuchi, A. Formation of InGaN quantum dots in regularly arranged GaN nanocolumns grown by rf-plasma-assisted molecular-beam epitaxy. *Phys. Status Solidi Curr. Top. Solid State Phys.* **7,** 2374–2377 (2010).

[Tak 1997] Takeuchi, T., Sota, S., Katsuragawa, M., Komori, M., Takeuchi, H., Amano, H. & Akasaki, I. Quantum Confined Stark Effect due to Piezoelectric Fields in GaInN Strained Quantum Wells. *Jpn. J. Appl. Phys.* **36,** L382–L385 (1997).

[Uni 2005] Unitt, D. C., Bennett, A. J., Atkinson, P., Ritchie, D. A. & Shields, A. J. Polarization control of quantum dot single-photon sources via a dipole-dependent Purcell effect. *Phys. Rev. B - Condens. Matter Mater. Phys.* **72,** 2–5 (2005).

[Win 2007] Winkelnkemper, M., Seguin, R., Rodt, S., Schliwa, A., Reißmann, L., Strittmatter, A., Hoffmann, A. & Bimberg, D. Polarized emission lines from A - And B -type excitonic complexes in single InGaN/GaN quantum dots. *J. Appl. Phys.* **101,** 1–5 (2007).

[Win 2008] Winkelnkemper, M., Dworzak, M., Bartel, T. P., Strittmatter, A., Hoffmann, A. & Bimberg, D. Origin of the broad lifetime distribution of localized excitons in InGaN/GaN quantum dots. *Phys. status solidi* **245,** 2766–2770 (2008).

[Zha 2016] Zhang, L., Teng, C.-H., Ku, P.-C. & Deng, H. Site-controlled InGaN/GaN single-photon-emitting diode. *Appl. Phys. Lett.* **108,** 153102 (2016).

5 CHAPTER. SEMI-POLAR AND NON-POLAR QDS IN A WIRE

Due to the significant difficulty and high cost in fabricating bulk GaN, the GaN-based technology has been mostly developed on foreign substrates. The natural growth direction of III-Nitrides is along the [0001] crystallographic direction for the most available conventional substrates *[Iwa 1997]*. Growth along this direction provides high quality materials. Unfortunately, the strong internal built-in electric field parallel to this axis, reaching up to 7 MV/cm in GaN/AlN QDs *[Bre 2006; Cro 2006]*, results in the redshift of the emission and its intensity reduction due to the quantum confined Stark effect (QCSE). That deteriorates the optical performance of III-Nitride based devices, i.e. reduces the quantum efficiency and increases the non-radiative recombination rate. It can also cause spectral diffusion, making it difficult to maintain the QD at resonance with optical cavities *[Ost 2010]*. Additionally, high internal electric fields lead to the increase of the emission lifetimes and, consequently, limit the repetition rates of single photon emitters.

Many ways were suggested to screen this internal field, i.e. by strong optical pumping, high doping, applying opposite external electric fields, strain minimization, etc. On the other hand, it is known that for semi-polar crystallographic orientations the polarization fields are significantly reduced *[Rom 2006]*. The estimation of the piezoelectric fields in III-Nitride based systems varies from few MV/cm for the c-plane to few hundreds kV/cm for semi-polar planes (($11\bar{2}2$), ($10\bar{1}1$) and ($10\bar{1}2$)) *[Wer 2012]*. The non-polar orientations, in turn, are, in principle, free of piezoelectric fields, so true flat band conditions can be restored *[Wal 2000; Spe 2009]*. Thus the emission energy from non-polar planes is solely determined by the quantum confinement and the electron-hole wave function overlap is close to unity. So, naturally, many research groups focused their attempts on fabricating structures grown along semi-polar and non-polar directions *[Zhu 2009; Wei 2008; Oka 2009; Min 2013; Das 2010]*. Successful growth of nitride zincblende *[Kak 2014; Ser 2013; Gar 2005]* as well as wurtzite QDs on non-polar *[Cro 2006; Zhu 2013; Rol 2007; Dau 2008]* and semi-polar *[Das 2011]* crystal planes has been reported. However, the poor stability of the cubic phase, makes the fabrication of high quality structures more difficult.

It has also been shown that growth kinetics and surface chemistry affect indium incorporation for different crystallographic orientations, leading to higher indium incorporation rate on polar compared to the semi-polar and non-polar planes for MBE grown structures *[Das 2010; Gac 2016]*. However, structures grown on non-polar and semi-polar planes generally exhibit a large density of threading dislocations and stacking faults which limit the critical thickness and, consequently, reduce the emission efficiency and increase the probability of non-radiative recombination *[Cra 2002; Oka 2009; Wei 2008; Zha 2012]*. The choice of suitable substrates is also limited.

As was already pointed out in Section 2.7.1., the 1D geometry can successfully overcome these problems, leading to exceptionally high crystalline quality of the material. Moreover, the pencil-like shape of the wires used in this Thesis allowed to form simultaneously QDs on planes with three different polarities, thus opening the possibility to obtain the combined single photon

sources, operating in three different regimes: (i) visible emission and $\leq$ 1 GHz operation speed (polar QDs), (ii) violet emission and $\sim$ 1.4 GHz operation speed (semi-polar QDs) and (iii) ultraviolet emission with $\sim$ 2.1 GHz operation speed (non-polar QDs).

In this chapter a sample containing dispersed coreshell NWs will be discussed in details. The differences and specific characteristics of the emission originated from semi-polar and non-polar regions of the InGaN inclusions were investigated by means of μ-PL with spectral, time and polarization resolution. The single photon performance was attested by photon autocorrelation measurements using pulsed optical excitation. It was found that emission bands arising from both semi-polar and non-polar crystallographic orientations contain linearly polarized single photon emitters of similar quality as their polar counterparts. Part of the work, concerning the TRPL and HBT experiments for non-polar and semi-polar InGaN regions was made by Dr. M. Holmes (group of Prof. Dr. Y. Arakawa) at the *Institute of Industrial Science, The University of Tokyo, Japan*, while the structural characterization was done by Prof. Dr. A. Torres-Pardo (group of Prof. J.M. González-Calbet) from *UCM-UPM, Madrid*.

5.1 SAMPLE DESCRIPTION

Ordered NW arrays with slightly different growth parameters, than the ones from Chapter 4, were fabricated by SAG PAMBE by the group of Prof. Dr. E. Calleja from ISOM-UPM. The resulted wires were approximately 500 nm in height and 200 nm in diameter and have a coreshell structure with pencil-like top (fig. 5.1.0.). High resolution transmission electron microscopy (HRTEM) ***[Gac 2016]*** confirms the formation of a fully conformal InGaN nanoshell with significantly higher In concentrations, (∼20%), as well as thickness, (∼30 nm), in its polar region compared to the semi-polar, (∼10%) and (∼10-30 nm), and non-polar, (∼10%) and (∼1-2 nm), respectively. The preferential facet for semi-polar (SP) region was changing from the $(10\bar{1}2)$ r- plane, corresponding to the initial GaN core (growth temperature 800°) to $(10\bar{1}1)$ s- planes corresponding to the InGaN shell (growth temperature 600°). The non-polar (NP) region formed a shell around the wire parallel to the $(10\bar{1}0)$ m-planes.

The same Si substrate with metal grid, as in Chapter 4, was used for dispersion. Only single wires were investigated to minimize the background contribution to the PL spectra.

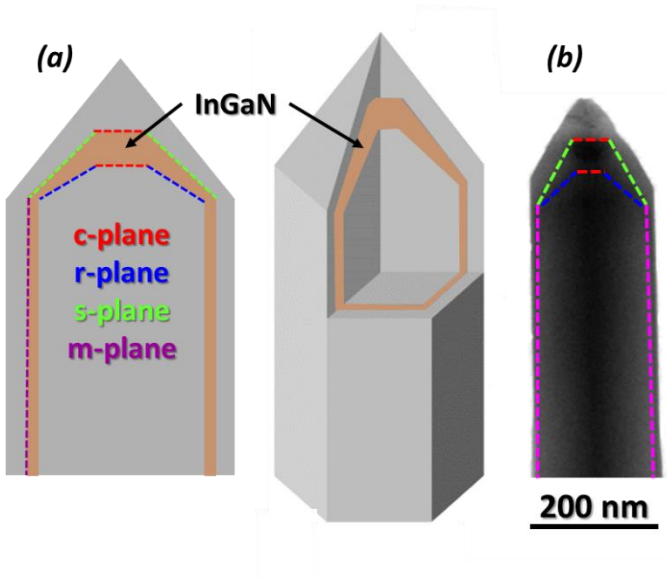

Fig. 5.1.0. (a) A sketch of the coreshell structure of InGaN/GaN nanowires. (b) HRTEM image of a representative NW. Dashed lines denote crystalline planes of inter-wire interfaces.

5.2 CATHODOLUMINESCENCE CHARACTERIZATION

Room temperature CL combined with (FEI Inspect F50) high resolution SEM measurements were performed to probe the location of both the semi-polar and non-polar regions. The experiments were made by Prof. Dr. Ž. Gačević at *ISOM-UPM*. The sample contained both standing and lying wires in order to have access to the different NW planes simultaneously (fig. 5.2.0.(a)). As can be seen in fig. 5.2.0.(e) there are four distinct CL regions: the one centered at ~365 nm (3.40 eV) is ascribed to the GaN near band edge emission and the other three to the emission from the InGaN nanoshell. An emission band roughly centered at 384 nm (3.23 eV) (fig. 5.2.0.(b)) originates from the InGaN shell and is, thus, attributed to the NP planes. A second emission band at approximately 405 nm (3.06 eV) is ascribed to the InGaN SP planes, as can be seen in fig. 5.2.0.(c). And, finally, the third emission band, at ~477 nm (2.60 eV) fig. 5.2.0.(d) originates from the NW apex, InGaN polar region (P).

Variations of the emission energy of the InGaN nanoshell, formed on planes of different polarity are commonly observed and usually attributed to the combination of differences in thickness (i.e. confinement effect), strain, piezoelectric field and In incorporation ***[Zha 2012; Nor 2009; Gac 2016; Wer 2012]***. Several groups additionally showed the facet dependent growth of III-Nitride based materials ***[Kit 1995; Lun 2012]***. Wernicke et al. reported, that In incorporation is similar in QW grown on the (0001), $(20\bar{2}1)$, $(10\bar{1}2)$ and $(10\bar{1}0)$ planes, thus ascribing the observed energy variation up to 600 meV mostly to the combination of the QCSE and anisotropic strain. However, other groups ***[Das 2010; Gac 2016; Kou 2012]*** suggested that for the semi-polar planes, $(10\bar{2}2)$, $(10\bar{1}2)$ and $(11\bar{2}2)$, the In incorporation is indeed reduced. A similar trend could be expected for QD

ensembles, although individual QDs, can fall out of this trend due to their particular geometry and composition.

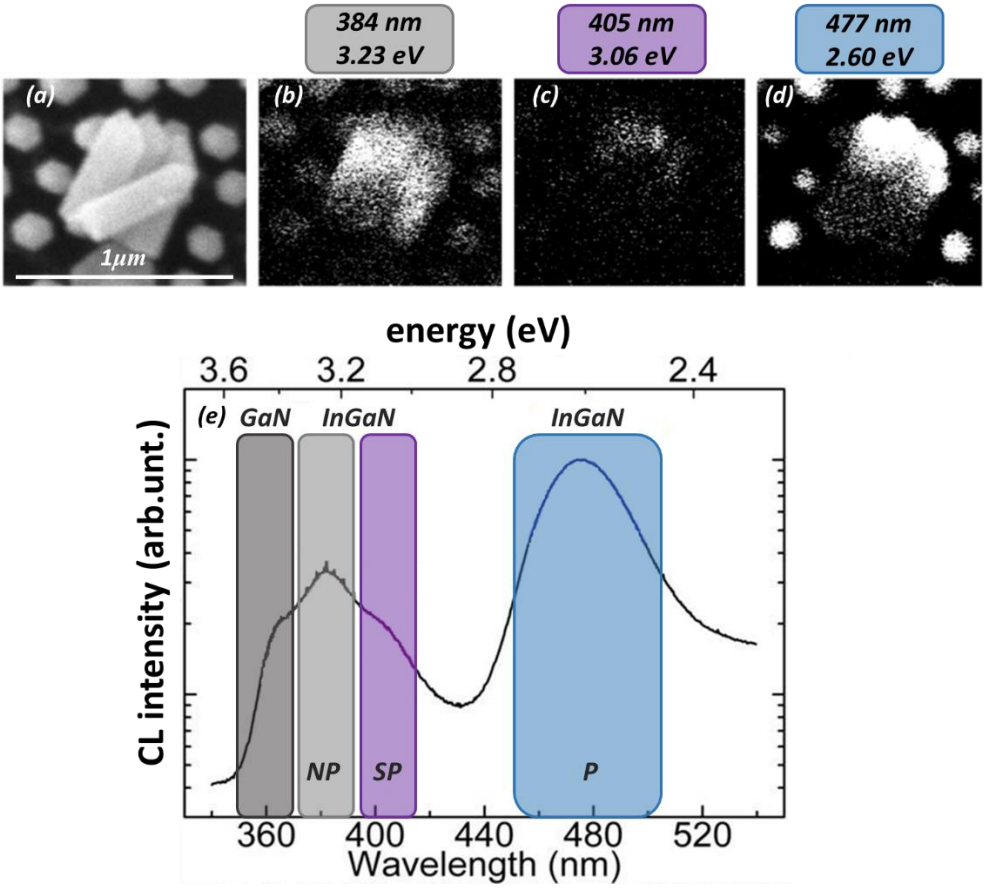

Fig. 5.2.0. (a) SEM image of the representative sample area. Room temperature SEM-CL measurements of non-polar (b), semi-polar (c) and polar (d) In-containing NW regions. (e) Corresponding room temperature CL spectrum.

We observed the maximum emission energy variation (up to 730 meV) between the (0001) and $(10\bar{1}0)$ planes and 560 meV between the (0001) and $(10\bar{1}2)$ planes, whose thicknesses varied from 30 nm (c-plane) to 1-2 nm (m-plane). Following the detailed theoretical and experimental structural analysis of similar samples, made in Ref *[Gac 2016]*, we attributed the optical differences between the planes of different polarities to the three main mechanisms: (i) In composition, (ii) electric field and (iii) strain. In composition is mostly influenced by the height- and facet dependent In incorporation. Different chemical properties of polar and semi-polar planes are responsible for the facet dependence. But the total energy minimization is the main driving mechanism of the height dependent integration of In atoms. In the other words, the compressive strain on the InGaN/GaN interface forces In atoms to move towards less strained regions. It was found that the strongest mechanism, responsible for the multicolor emission is, indeed, In concentration variations, while strain is the least important one.

5.3 MICRO-PHOTOLUMINESCENCE CHARACTERIZATION

Low temperature μ-PL spectrum of the single lying NW, shown on fig. 5.3.0., confirms the finding of CL experiments. There are also three emission bands, emitting in the UV (NP), violet (SP) and visible (P) spectral regions corresponding to the InGaN nanoshell. The identification of QD-like confinement potentials was made by μ-PL measurements under cw excitation by a He-Cd laser (λ = 325 nm) and a frequency-tripled Ti:sapphire laser (200 fs pulses at 80 MHz with λ = 266 nm) for the polar/semi-polar and non-polar emission bands respectively. Narrow peaks with Lorentzian shape, corresponding to the exciton ground state transitions were detected in all three InGaN regions (fig. 5.3.1. left panels). This assignment was attested by the linear power dependence of the integrated intensity (fig. 5.3.1. right panels). The quantity of sharp emission lines on both SP and NP facets was less than for the polar region. Indeed, the NP section had very few QD-like centers. This indicates that the potential fluctuations were the strongest for the polar part and the weakest for the NP one, which is expected from the variation of the corresponding thicknesses: ~30 nm and ~1-2 nm, respectively, and the difference in indium concentration between the involved facets. Like in the polar parts, there were more than one peak detected for some single wires in SP and NP regions, as expected for In fluctuations as the origin of such QDs.

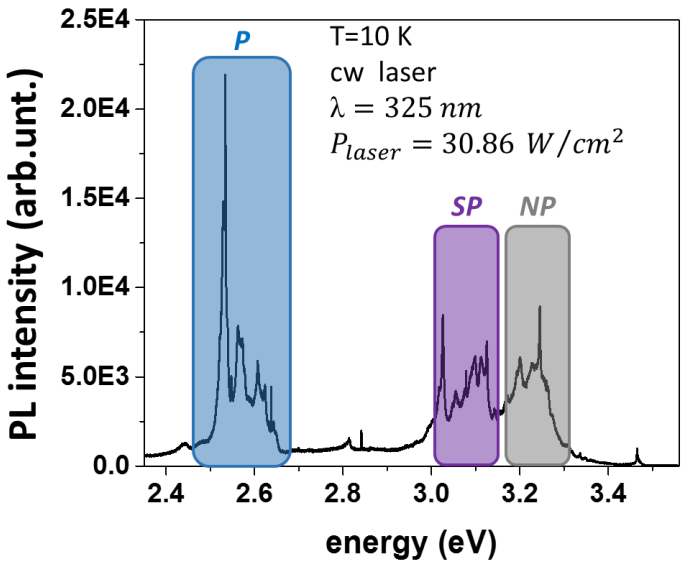

Fig. 5.3.0. Low temperature μ-PL spectrum under cw UV excitation of a single lying NW.

The FWHM of NP and SP emission lines varied from hundreds of μeV to 1-2 meV, which agrees well with literature reports ***[Zhu 2013; Rei 2014; Kak 2014; Ser 2013; Rol 2007; Dau 2008]*** and, also, they are similar to those of polar QDs.

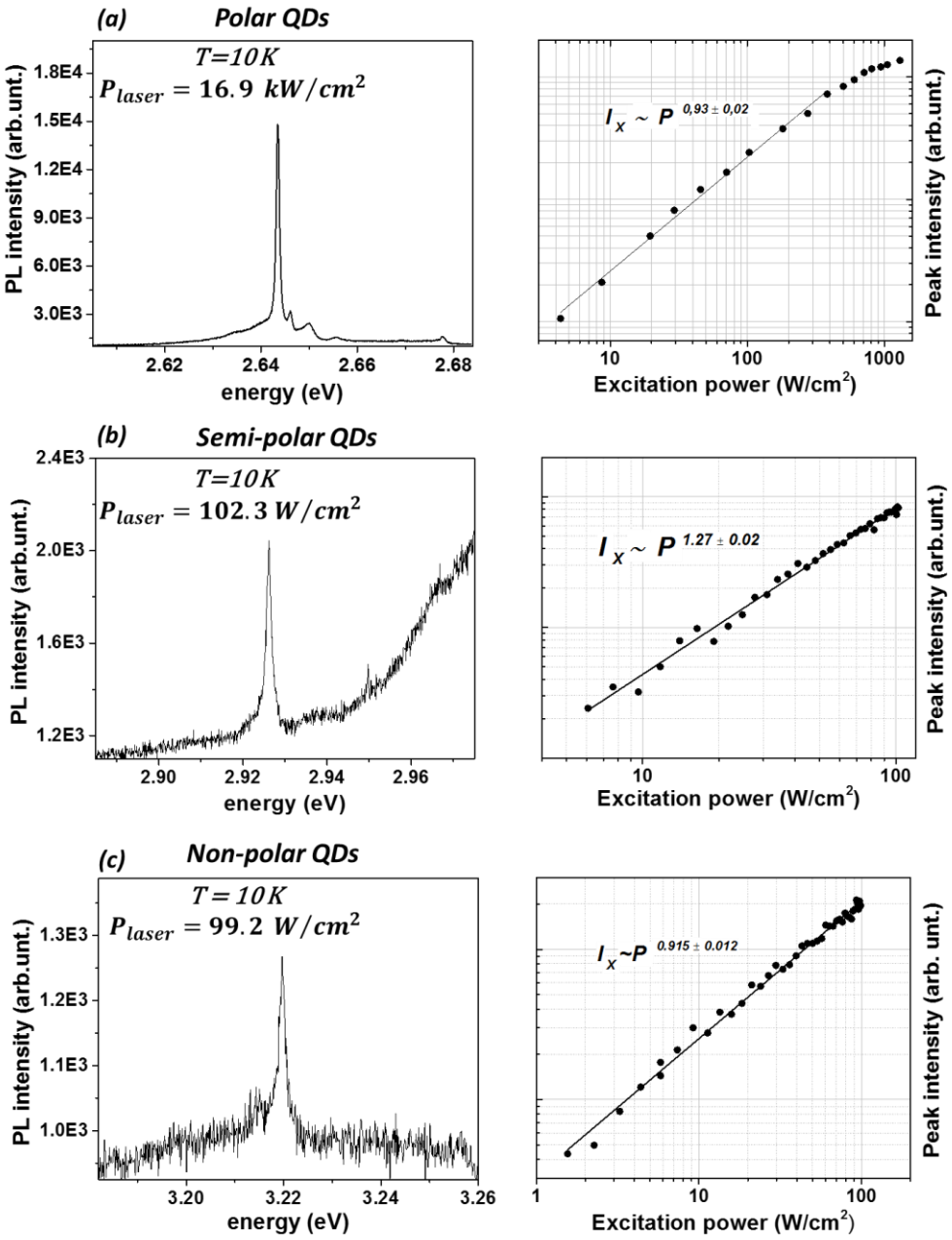

Fig. 5.3.1. Low temperature μ-PL spectra (left panels) and integrated intensity as a function of the laser power (right panels) for polar (a), semi-polar (b) and non-polar (c) QDs.

No change in the emission energy was observed for the range of excitation powers up to 140 W/cm^2 neither for SP nor for NP QDs, contrary to their polar counterparts, where a clear screening effect was evidenced by the spectral shift, reaching up to 300 μeV for similar excitation power for some QDs. This fact gives an additional proof of the minor influence of the piezoelectric field in NP QDs, as expected ***[Dau 2008]***.

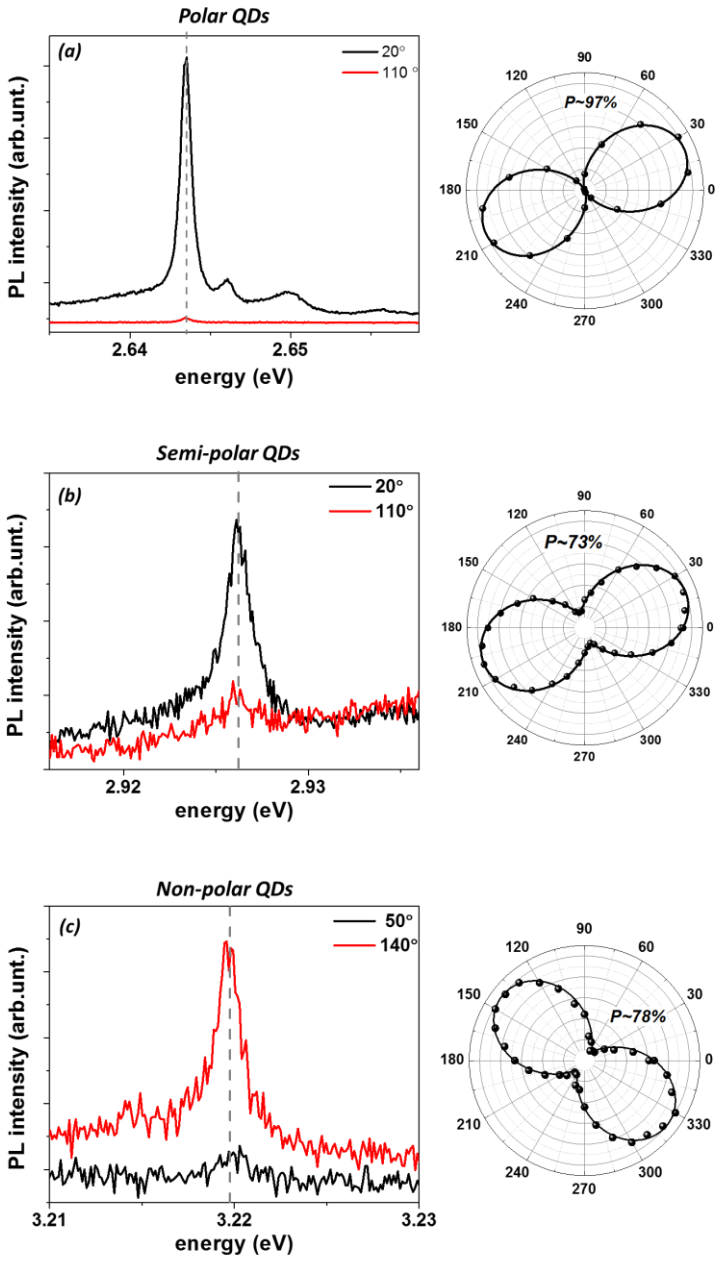

Fig. 5.3.2. Low temperature μ-PL spectra of two orthogonal polarization components (left panels) and corresponding polar plots (right panels) for polar (a), semi-polar (b) and non-polar (c) QDs. The solid lines are fit to formula 4.2.0.

A high degree of linear polarization ($P \geq 75$ %) was observed in both SP and NP QDs (fig. 5.3.2.). Polarization degrees higher than 90 % were also reported for III-Nitride based SP ***[Pat 2016]*** and NP ***[Rei 2015; Ren 2008]*** QDs. Polarization-resolved studies showed the same randomness in the polarization direction, as for polar QDs, in agreement with the In fluctuation origin of such QDs. No FSS was observed (fig. 5.3.2. left panels), similarly to the polar counterparts.

5.4 TIME-RESOLVED MICRO-PHOTOLUMINESCENCE

The TRPL experiments were carried out under excitation by a diode laser (λ = 442 nm) for P QDs and a frequency-tripled Ti:sapphire laser (200 fs pulses at 80 MHz with λ = 266 nm) for SP/NP QDs, respectively. As can be seen in fig. 5.4.0., the decay times for SP and NP regions are below the ns range. The excitation power level was kept below saturation. The monoexponential fit to the measured data gave values of 400-550 ps and 550-880 ps for NP and SP QDs decay times, respectively. These lifetimes are smaller than for the polar QDs (~2340-2720 ps), corresponding to the reduced internal electric field. Also, the thickness of the SP region (10-30 nm) is one order of magnitude larger than the NP one (1-2 nm), thus the separation between electrons and holes is expected to be larger for SP than for NP QDs. The obtained values of the emission lifetimes are in a good agreement with the values reported in the literature *[Eme 2014; Zhu 2013]*.

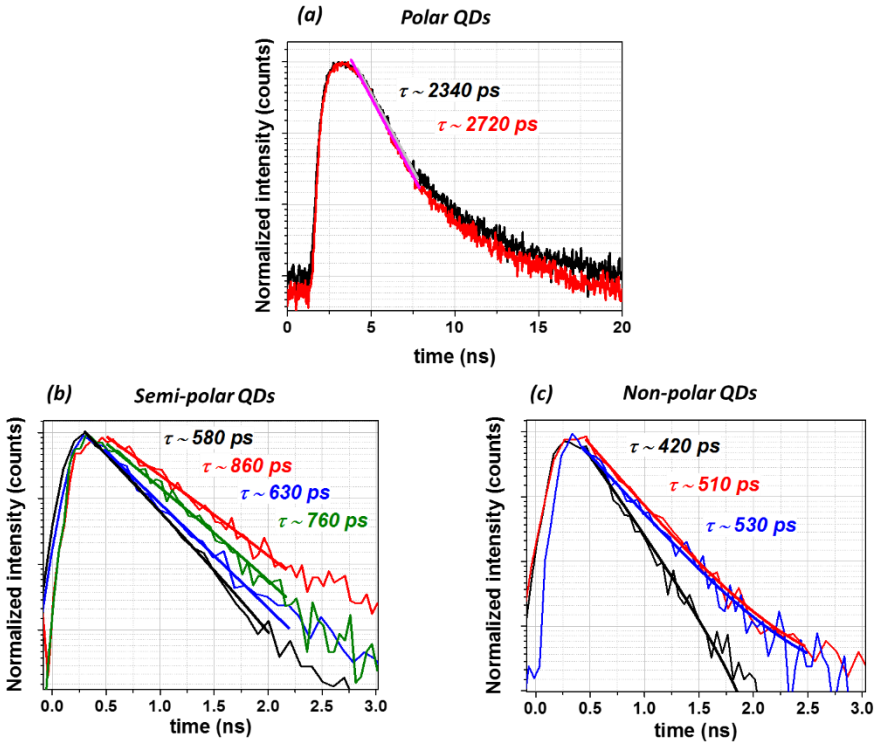

Fig. 5.4.0. Time-resolved μ-PL spectra for several polar (a), semi-polar (b) and non-polar (c) QDs

The piezoelectric and spontaneous polarization fields and composition fluctuations in the vicinity of the QDs as well as the QD size/shape variations can affect drastically their radiative lifetimes *[Wal 2000; Spe 2009; Bar 2004]*. Thus it is expected that decay times of the QDs at non-polar and semi-polar InGaN regions are different from the polar QDs. In general, QDs emitting at higher energy (or small QDs), are essentially faster, than those emitting at lower energy. But for the case of QDs formed by material composition fluctuations, as in our case, the trend can be partially masked (see polar QDs in fig. 5.4.1.(a)) by the difference in In concentration in the QD and its surroundings. Thus small sized QDs with lower In content and larger ones with higher In content can emit at similar energies, but will have different decay times, as can be seen for polar QDs in

fig. 5.4.1.. In NP QDs this effect is expected to be less important, as the size of In fluctuations is reduced.

Fig. 5.4.1. presents the PL decay times for all investigated P, SP and NP QDs as a function of their emission energy. An overall trend to shorter lifetimes for higher emission energies (smaller QDs) can be seen. Some groups reported a weaker dependence of the emission times vs emission energies for NP GaN QDs compared to polar ones *[Sim 2003; Dau 2008; Fou 2005]*.

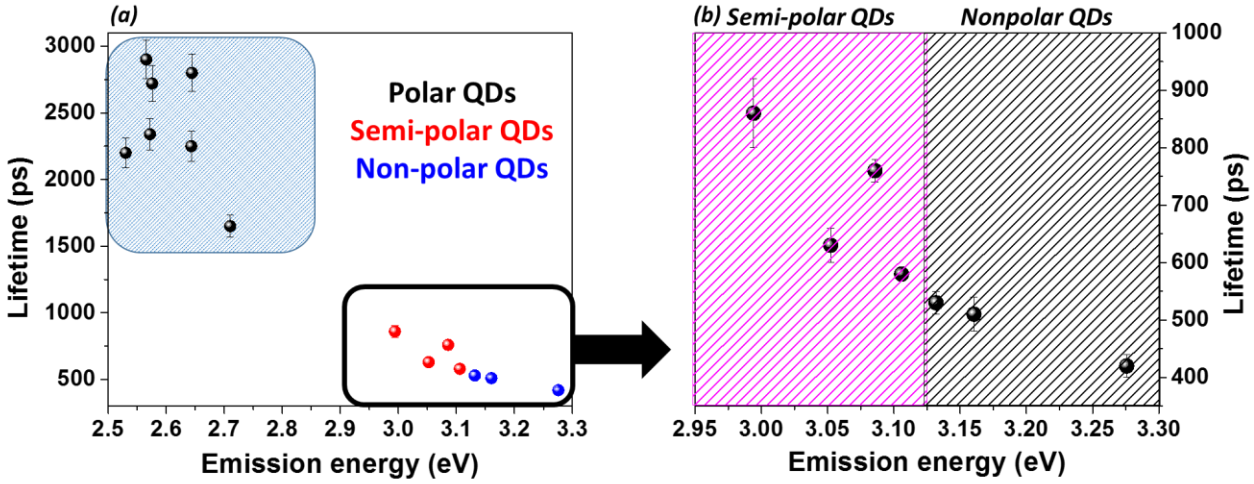

Fig. 5.4.1. Emission lifetimes for P, SP and NP QDs as a function of emission energy (a). Enlarged part, corresponding to the SP and NP QDs (b).

One can clearly see a steeper decrease for SP QDs, showing stronger dependence on QD size, than for NP QDs (fig. 5.4.1.(b).). The electron-hole wave function overlap is strongly dependent on the QD size, shape and electric field. Note, that for polar QDs, the electric filed points along the c-axis (vertical confinement direction) and, thus, causes both PL redshift and reduction of electron-hole wave function overlap. This effect is expected to depend on QD size along the c-axis, but not so much on lateral size variations, which do not affect wave function overlap. In the case of NP QDs the situation is reversed, as the piezoelectric field lies in the m-plane and is, thus, perpendicular to the QD confinent by the GaN barrier (remember that the InGaN shell is only 1-2 nm thick). Thus the field will not produce a significant red-shift but it can slightly separate electrons and holes in the c-direction, depending on the QD size in this direction. This can explain the weak slope observed for NP QDs in fig. 5.4.1.(b).. SP QDs show an intermediate behavior between NP and P QDs.

5.5 PHOTON-CORRELATION MEASUREMENTS

The autocorrelation measurements for the SP and NP QDs were performed in the HBT interferometer under pulsed excitation by a frequency-tripled Ti:sapphire laser (200 fs pulses at 80 MHz with λ = 266 nm) and for P QDs under cw optical excitation (λ = 442 nm). The clear

reduction of the central peak (fig. 5.5.0.) proves single photon emission by the QDs of all three polarities. The second order correlation function at zero time delay for SP and NP QDs was estimated as the ratio of the normalized integrated area underneath the central peak and the averaged normalized integrated area underneath the non-zero delay peaks. For the polar QDs $g^2(0)$ was evaluated following the procedure, described in Chapter 4. Its as-measured values and the corrected ones (see the background correction procedure in Chapter 4, see formula 4.3.3.) are presented in table 5.5.0. The corrected values are well below the 0.5 threshold, expected for the case of the emission of the two photons. The smaller background in NP QDs leads to the $g^2_{corr}(0) \approx 0$, suggesting that the deviation from the ideal non-classical source can be entirely accounted for by the background emission of the surrounding InGaN QW-like region.

QD	$g^{(2)}_{meas}(0)$	$g^2_{corr}(0)$	ρ
Polar	0.33 ± 0.03	0.18 ± 0.03	0.90
Semi-polar	0.54 ± 0.06	0.30 ± 0.09	0.81
Non-polar	0.40 ± 0.09	0.13 ± 0.13	0.83

Table 5.5.0. Values of second order correlation function for polar, semi-polar and non-polar QDs.

Indeed, similarly low values of the second order correlation function at zero time delay were reported for cubic GaN/AlN QDs ***[Kak 2014]***. However, to the best of our knowledge, there are no reports yet on SPS based on the semi-polar InGaN QDs.

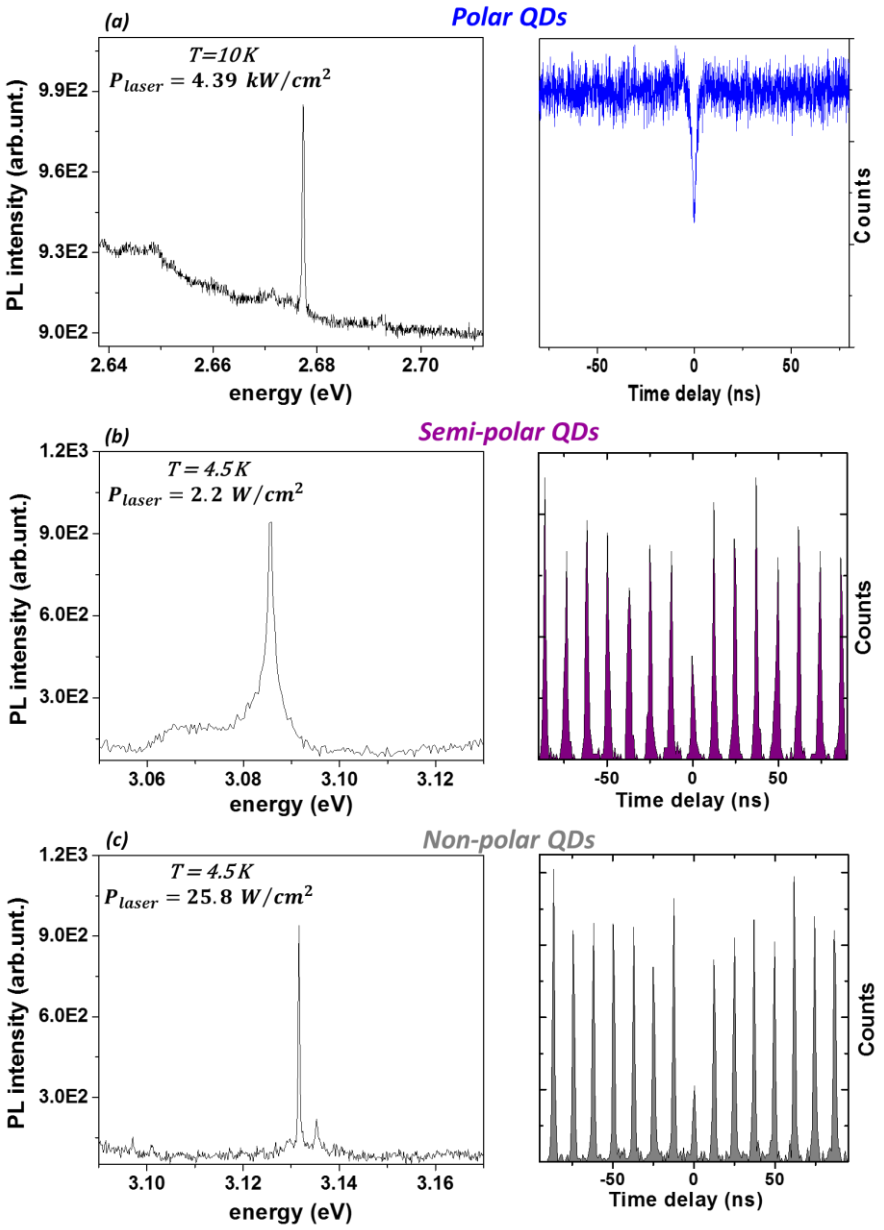

Fig. 5.5.0. Low temperature μ-PL spectra (right panel) and corresponding photon correlation data (left panel) for P (a), SP (b) and NP (c) QDs.

5.6 SUMMARY

We investigated the optical properties of QDs, formed on the polar (c-), semi-polar (r-) and non-polar (m-) planes of coreshell InGaN/GaN nanowires. The structural characterization revealed a 30 nm thick InGaN layer on the polar plane. Additionally, a 10-30 nm thick semi-polar QW is formed in between the s- and r- planes. The InGaN shell, formed along the m-plane was only 1-2 nm thick. The formation of these structures with their specific compositions and shapes was

related to the combination of three main mechanisms: (i) In incorporation, including In composition, height and facet dependence, (ii) piezoelectric fields and (iii) strain. The SP and NP QDs emission energy variation (up to 730 meV) with respect to the polar QDs was discussed in terms of the geometry (size/shape), confinement and the QD/barrier interface electrical conditions.

All three types of QDs showed narrow emission lines (0.3-2 meV) with a high degree of linear polarization (>70 %), comparable to the previous literature reports. The polarization angle was found to be random, as expected from the random In fluctuations at the origin of the QDs. The P QDs emitted in visible, SP QDs - in the violet and the NP ones in the ultraviolet spectral regions, which is also in good agreement with the literature reported values. No FSS was found. The relatively few QD-like emission centers in the NP regions compared to the polar ones were ascribed to the smaller In concentration fluctuations due to the the thinner NP region and smaller averaged In concentration.

The TRPL studies revealed emission lifetimes in the picosecond range following the sequence: $\tau_{NP} < \tau_{SP} < \tau_{polar}$. It was found that there is a tendency to shorter lifetimes for QDs emitting at higher energy (smaller QDs). The difference in slopes for NP and SP QDs was explained in terms of smaller effect of the piezoelectric field for NP QDs. Since for non-polar planes the electric field is perpendicular to the QD confinement direction by the GaN barriers, it can only separate electrons and holes in the lateral direction (c-axis), while the vertical separation is fixed by the QD height (i.e. the InGaN shell thickness). In the case of SP QDs the piezoelectric field affects both lateral and vertical e-h separation thus making their lifetimes more sensitive to the QD geometry.

The photon statistics of P, SP and NP QDs was studied by photon correlation measurements. All three types of QDs showed a clear photon antibunching with values of the second order correlation function at zero time delay well below the 0.5 threshold. After background corrections we obtained $g^2_{corr}(0) = 0.18 \pm 0.03$, $g^2_{corr}(0) = 0.30 \pm 0.09$ and $g^2_{corr}(0) = 0.13 \pm 0.13$ for P, SP and NP QDs respectively.

Thus the coreshell nanowire with the pencil-like top is indeed a highly linear polarized multicolor single photon source emitting in ultraviolet (NP QDs), violet (SP QDs) and visible (polar QDs) spectral regions. The repetition rates reach up to 2.1 GHz, in NP QDs. The low values of the second order correlation function at zero time delay together with the potential high repetition rates make this combined SPS an attractive and reliable tool for the realization of high speed quantum information processing devices. Additionally, its combination with the nanowire geometry facilitates its integration with already existing components of on-chip optoelectronic devices.

5.7 FUTURE WORK

As a future line of investigation, we point to SPSs operating in the blue and UV at high temperatures. The implementation of an AlGaN barrier should produce enough confinement for high temperature operation. The fine details of the growth procedure are crucial to obtain NP and SP QDs with better structural and optical quality.

References

[Bar 2004] Bartel, T., Dworzak, M., Strassburg, M., Hoffmann, A., Strittmatter, A. & Bimberg, D. Recombination dynamics of localized excitons in InGaN quantum dots. *Appl. Phys. Lett.* **85,** 1946–1948 (2004).

[Bre 2006] Bretagnon, T., Lefebvre, P., Valvin, P., Bardoux, R., Guillet, T., Taliercio, T., Gil, B., Grandjean, N., Semond, F., Damilano, B., Dussaigne, A. & Massies, J. Radiative lifetime of a single electron-hole pair in GaN/AlN quantum dots. *Phys. Rev. B* **73,** 113304 (2006).

[Cra 2002] Craven, M. D., Lim, S. H., Wu, F., Speck, J. S. & DenBaars, S. P. Structural characterization of non-polar (11$\bar{2}$0) a-plane GaN thin films grown on (1$\bar{1}$02) r-plane sapphire. *Appl. Phys. Lett.* **81,** 469 (2002).

[Cro 2006] Cros, A., Budagosky, J. A., García-Cristóbal, A., Garro, N., Cantarero, A., Founta, S., Mariette, H. & Daudin, B. Influence of strain in the reduction of the internal electric field in GaN/AIN quantum dots grown on a-plane 6H-SiC. *Phys. Status Solidi Basic Res.* **243,** 1499–1507 (2006).

[Das 2010] Das, A., Magalhães, S., Kotsar, Y., Kandaswamy, P. K., Gayral, B., Lorenz, K., Alves, E., Ruterana, P. & Monroy, E. Indium kinetics during the plasma-assisted molecular beam epitaxy of semi-polar (11−22) InGaN layers. *Appl. Phys. Lett.* **96,** 181907 (2010).

[Das 2011] Das, A., Dimitrakopulos, G. P., Kotsar, Y., Lotsari, A., Kehagias, T., Komninou, P. & Monroy, E. Improved luminescence and thermal stability of semi-polar (11-22) InGaN quantum dots. *Appl. Phys. Lett.* **98,** 201911 (2011).

[Dau 2008] Daudin, B. Polar and non-polar GaN quantum dots. *J. Phys. Condens. Matter* **20,** 473201 (2008).

[Eme 2014] Emery, R. M., Zhu, T., Oehler, F., Reid, B., Taylor, R. A., Kappers, M. J. & Oliver, R. A. Non-polar (11-20) InGaN quantum dots with short exciton lifetimes grown by metal-organic vapour phase epitaxy. *Phys. status solidi* **11,** 698–701 (2014).

[Fou 2005] Founta, S., Rol, F., Bellet-Amalric, E., Bleuse, J., Daudin, B., Gayral, B., Mariette, H. & Moisson, C. Optical properties of GaN quantum dots grown on non-polar (11-20) SiC by molecular-beam epitaxy. *Appl. Phys. Lett.* **86,** 171901 (2005).

[Gac 2016] Gačević, Ž., Vukmirović, N., García-Lepetit, N., Torres-Pardo, A., Müller, M., Metzner, S., Albert, S., Bengoechea-Encabo, A., Bertram, F., Veit, P., Christen, J., González-Calbet, J. M. & Calleja, E. Influence of composition, strain, and electric field anisotropy on different emission colors and recombination dynamics from InGaN nanodisks in pencil-like GaN nanowires. *Phys. Rev. B* **93,** 125436 (2016).

[Gar 2005] Garayt, J. P., Gérard, J. M., Enjalbert, F., Ferlazzo, L., Founta, S., Martinez-Guerrero, E., Rol, F., Araujo, D., Cox, R., Daudin, B., Gayral, B., Si Dang, L. & Mariette, H. Study of isolated cubic GaN quantum dots by low temperature cathodoluminescence. *Phys. E Low-Dimensional Syst. Nanostructures* **26,** 203–206 (2005).

[Iwa 1997] Iwata, K., Asahi, H., Asami, K., Kuroiwa, R. & Gonda, S. Gas Source Molecular Beam Epitaxy Growth of GaN on C-, A-, R- and M-Plane Sapphire and Silica Glass Substrates. *Jpn. J. Appl. Phys.* **36,** L661–L664 (1997).

[Kak 2014] Kako, S., Holmes, M., Sergent, S., Bürger, M., As, D. J. & Arakawa, Y. Single-photon emission from cubic GaN quantum dots. *Appl. Phys. Lett.* **104,** 11101 (2014).

[Kit 1995] Kitamura, S., Hiramatsu, K. & Sawaki, N. Fabrication of GaN Hexagonal Pyramids on Dot-Patterned GaN/Sapphire Substrates via Selective Metalorganic Vapor Phase Epitaxy. *Jpn. J. Appl. Phys.* **34,** L1184–L1186 (1995).

[Kou 2012] Koukoula, T., Lotsari, A., Kehagias, T., Dimitrakopulos, G. P., Häusler, I., Das, A., Monroy, E., Karakostas, T. & Komninou, P. Structure and strain state of polar and semi-polar InGaN quantum dots. *Appl. Surf. Sci.* **260,** 7–12 (2012).

[Lun 2012] Lundskog, A., Palisaitis, J., Hsu, C. W., Eriksson, M., Karlsson, K. F., Hultman, L., Persson, P. O. Å., Forsberg, U., Holtz, P. O. & Janzén, E. InGaN quantum dot formation mechanism on hexagonal GaN/InGaN/GaN pyramids. *Nanotechnology* **23,** 305708 (2012).

[Min 2013] Min, D., Yoo, G., Ryu, Y., Moon, S., Nam, K., Lim, H. & Nam, O. Improved Performance of (1122) Semi-polar InGaN/GaN Light-Emitting Diodes Grown Using a Hemispherically Patterned SiO_2 Mask. *Jpn. J. Appl. Phys.* **52,** 10MA03 (2013).

[Nor 2009] Northrup, J. E. GaN and InGaN (11-22) surfaces: Group-III adlayers and indium incorporation. *Appl. Phys. Lett.* **95,** 133107 (2009).

[Oka 2009] Okada, N., Kurisu, A., Murakami, K. & Tadatomo, K. Growth of Semi-polar (11-22) GaN Layer by Controlling Anisotropic Growth Rates in r -Plane Patterned Sapphire Substrate. *Appl. Phys. Express* **2,** 91001 (2009).

[Ost 2010] Ostapenko, I. A., Hönig, G., Kindel, C., Rodt, S., Strittmatter, A., Hoffmann, A. & Bimberg, D. Large internal dipole moment in InGaN/GaN quantum dots. *Appl. Phys. Lett.* **97,** 63103 (2010).

[Pat 2016] Patra, S. K., Marquardt, O. & Schulz, S. Polar, semi- and non-polar nitride-based quantum dots: influence of substrate orientation and material parameter sets on electronic and optical properties. *Opt. Quantum Electron.* **48,** 151 (2016).

[Rei 2014] Reid, B. P. L., Zhu, T., Chan, C. C. S., Kocher, C., Oehler, F., Emery, R., Kappers, M. J., Oliver, R. A. & Taylor, R. A. High temperature stability in non-polar (11-20) InGaN quantum dots: Exciton and biexciton dynamics. *Phys. status solidi* **11,** 702–705 (2014).

[Rei 2015] Reid, B. P. L., Kocher, C., Zhu, T., Oehler, F., Chan, C. C. S., Oliver, R. A. & Taylor, R. A. Non-polar InGaN quantum dot emission with crystal-axis oriented linear polarization. *Appl. Phys. Lett.* **106,** 1–9 (2015).

[Ren 2008] Renard, J., Amstatt, B., Bougerol, C., Bellet-Amalric, E., Daudin, B. & Gayral, B. Optical properties of m-plane GaN quantum dots and quantum wires. *J. Appl. Phys.* **104,** 103528 (2008).

[Rol 2007] Rol, F., Founta, S., Mariette, H., Daudin, B., Dang, L. S., Bleuse, J., Peyrade, D., Gérard, J.-M. & Gayral, B. Probing exciton localization in non-polar GaN/AlN quantum dots by single-dot optical spectroscopy. *Phys. Rev. B* **75,** 125306 (2007).

[Rom 2006] Romanov, A. E., Baker, T. J., Nakamura, S., Speck, J. S. Strain-induced polarization in wurtzite III-nitride semi-polar layers. *J. Appl. Phys.* **100,** 23522 (2006).

[Ser 2013] Sergent, S., Kako, S., Bürger, M., As, D. J. & Arakawa, Y. Narrow spectral linewidth of single zinc-blende GaN/AlN self-assembled quantum dots. *Appl. Phys. Lett.* **103,** 151109 (2013).

[Sim 2003] Simon, J., Pelekanos, N. T., Adelmann, C., Martinez-Guerrero, E., Andre, R., Daudin, B., Dang, L. S. & Mariette, H. Direct comparison of recombination dynamics in cubic and hexagonal GaN/AlN quantum dots. *Phys. Rev. B* **68,** 35312 (2003).

[Spe 2009] Speck, J. S. & Chichibu, S. F. Non-polar and Semi-polar Group III Nitride-Based Materials. *MRS Bull.* **34,** 304–312 (2009).

[Wal 2000] Waltereit, P., Brandt, O., Trampert, A., Grahn, H. T., Menniger, J., Ramsteiner, M., Reiche, M. & Ploog, K. H. Nitride semiconductors free of electrostatic fields for efficient white light-emitting diodes. *Nature* **406,** 865–868 (2000).

[Wei 2008] Wei, T., Duan, R., Wang, J., Li, J., Huo, Z., Yang, J. & Zeng, Y. Microstructure and Optical Properties of Non-polar m -Plane GaN Films Grown on m -Plane Sapphire by Hydride Vapor Phase Epitaxy. *Jpn. J. Appl. Phys.* **47,** 3346–3349 (2008).

[Wer 2012] Wernicke, T., Schade, L., Netzel, C., Rass, J., Hoffmann, V., Ploch, S., Knauer, A., Weyers, M., Schwarz, U. & Kneissl, M. Indium incorporation and emission wavelength of polar, non-polar and semi-polar InGaN quantum wells. *Semicond. Sci. Technol.* **27,** 24014 (2012).

[Zha 2012] Zhao, Y., Yan, Q., Huang, C.-Y., Huang, S.-C., Shan Hsu, P., Tanaka, S., Pan, C.-C., Kawaguchi, Y., Fujito, K., Van de Walle, C. G., Speck, J. S., DenBaars, S. P., Nakamura, S. & Feezell, D. Indium incorporation and emission properties of non-polar and semi-polar InGaN quantum wells. *Appl. Phys. Lett.* **100,** 201108 (2012).

[Zhu 2009] Zhu, T., Martin, D. & Grandjean, N. M -Plane GaN Grown on m -Plane Sapphire by Hydride Vapor Phase Epitaxy. *Jpn. J. Appl. Phys.* **48,** 20226 (2009).

[Zhu 2013] Zhu, T., Oehler, F., Reid, B. P. L., Emery, R. M., Taylor, R. A., Kappers, M. J. & Oliver, R. A. Non-polar (11-20) InGaN quantum dots with short exciton lifetimes grown by metal- organic vapor phase epitaxy Non-polar (11-20) InGaN quantum dots with short exciton lifetimes grown by metal-organic vapor phase epitaxy. *Appl. Phys. Lett.* **102,** 251905–3388 (2013).

6 CHAPTER. ACOUSTICALLY CONTROLLED PHOTON EMISSION DYNAMICS IN III-NITRIDE NANOWIRE QDS

The modulation of optical properties under SAW-induced fields is investigated in this Chapter. Different stroboscopic techniques were employed along with μ-PL spectroscopy to study both spectral and temporal dynamics of the system. A detailed description of the specific sample design, preparation and characterization will be addressed. Finally, possible future lines of investigation will be outlined and some preliminary results will be briefly discussed.

6.1 SAMPLE PREPARATION

The SAW delay lines with pairs of unidirectional floating electrode IDTs *[Yam 1992]* were fabricated by optical lithography on an undoped 128° Y-cut lithium niobate ($LiNbO_3$) substrate. They were designed to generate multiple harmonics of a fundamental frequency of 110 MHz (at room temperature), which corresponds to the SAW wavelength of 35 μm. The IDT design and processing were done by the group of Prof. Dr. P.V. Santos at the *Paul Drude Institute (PDI)* in Berlin, Germany. The next step was to transfer the InGaN/GaN nanowire heterostructures onto the SAW pathway between the two IDTs forming a delay line. As described in Chapter 4, both mechanical scratching and droplet dispersion were used to disperse the wires onto a $LiNbO_3$ surface. The density and the homogeneity of the NWs dispersion was monitored by optical and scanning electron microscopies (fig. 6.1.0. (a-e)). Once a desired NW density and distribution was achieved the sample was mounted on a chip carrier. The IDT pads were then bonded to the metal pins on the chip case (see Section 3.3 for more details on sample mount and bonding). The dispersion was done by Profs. Drs. S. Lazić and Ž. Gačević and bonding by Mrs. M. C. Sabido Siller at *ISOM-UPM*.

The IDTs were approximately 700 μm long and have an aperture approximately equal to the finger length, $l_{IDT} = 400$ μm. The metal deposition was done following the sequence: a 10 nm layer of Ti, followed by 30 nm of Al and again 10 nm of Ti. The double finger design was used to reduce scattering and reflection losses. For most of the measurements the third harmonic was used as it had the highest electro-acoustic conversion efficiency. The corresponding resonance band was centered roughly at 337.5 MHz at 10 K, which corresponds to a SAW period of ~3 ns. Since the IDTs resonance frequencies are temperature dependent, it was necessary to check them with a vector network analyzer (VNA) before each experiment.

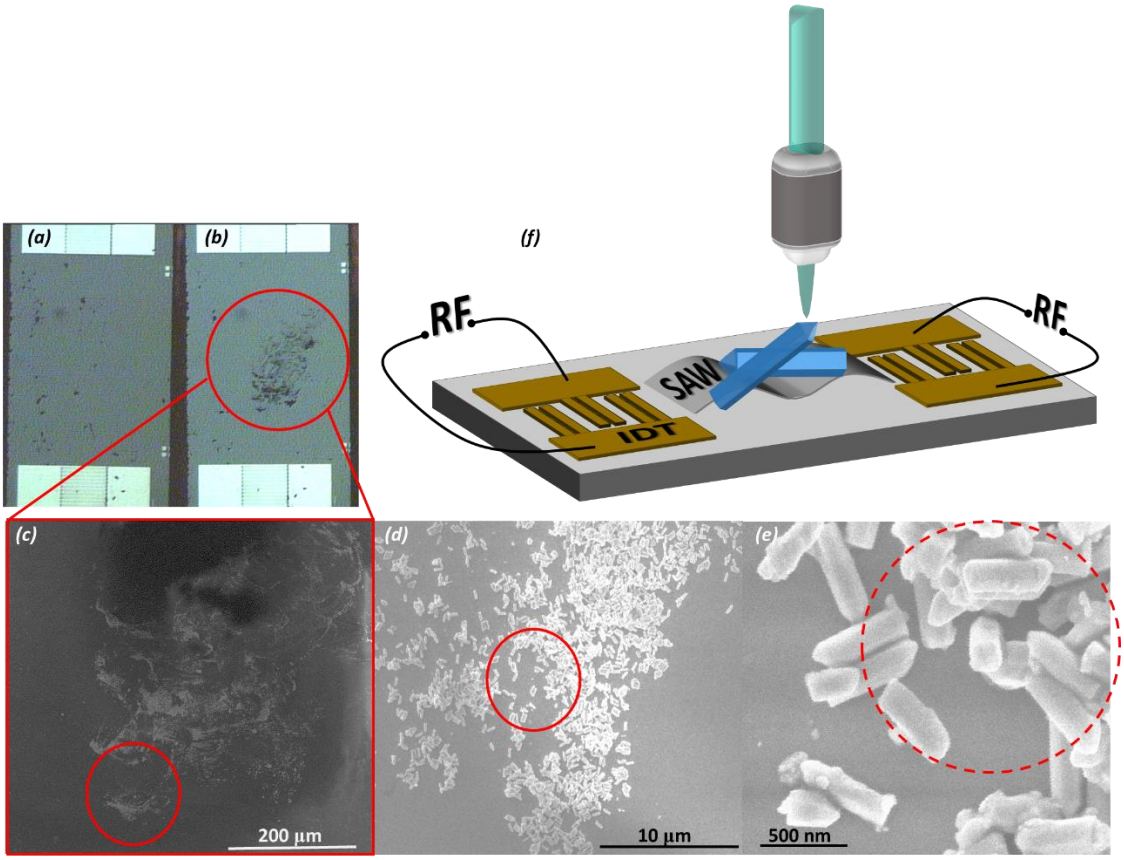

Fig. 6.1.0. The optical microscope image of the sample before (a) and after NW dispersion (b). (c-d) A series of zoomed SEM images of the NW bunch. The dashed red circle roughly shows the sample area probed by the excitation laser in the µ-PL experiment. (f) The sketch of the sample, not in scale.

6.2 IDT CHARACTERIZATION

The IDT characterization was carried out at room temperature by measuring the reflection and transmission parameters, as was explained in Chapter 2. As seen in fig. 6.2.0.(a) both electrodes have similar RF power reflection and transmission coefficients, indicating that the lithographic procedure was successful and the finger electrodes were properly developed. In order to evaluate the IDT performance the third harmonic of the fundamental frequency was used (fig. 6.2.0.(b)). The bandwidth of approximately 2 MHz was centered at 331 MHz. The insertion losses were calculated using formulas 2.9.6.-7 from Section 2.9.2. and the estimated value was 10.5 dBm. The return losses were approximately 21 dBm. The electro-acoustic conversion efficiency for symmetric delay lines is half of the insertion losses, i.e. 5.3 dBm. Therefore the fraction of input electric power converted to acoustic power by the IDTs is $r_a = 29.8\%$.

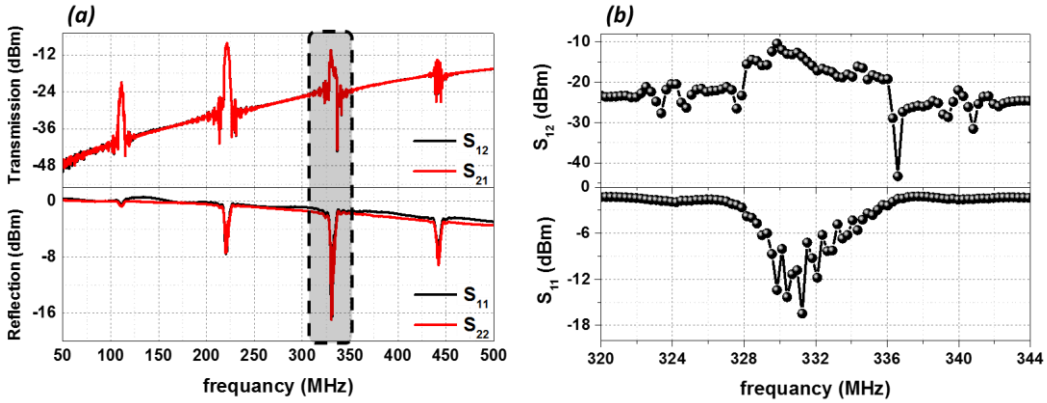

Fig. 6.2.0. (a) RF power transmission (S_{12}, S_{21}) and reflection (S_{11}, S_{22}) coefficients (b) A zoomed-in frequency region showing the RF power transmission S_{12} (upper panel) and reflection S_{11} (lower panel) coefficient for the third harmonic of the fundamental frequency.

It is important to note, that the evaluation of IDTs performance is also dependent on the way it is measured. Although for some purposes the uncorrected performance of the VNA is sufficient. However, for the losses calculations a higher level of accuracy is required. Thus the calibration procedure, explained in Chapter 3 was employed.

6.3 MICRO PL CHARACTERIZATION

The preliminary low temperature optical characterization was performed in the μ-PL setup as described in Chapter 3. Firstly, in the absence of the SAW the emission from the NW bunch, showed in fig. 6.1.0., was studied. The two intense narrow lines were attributed to the recombination of the X (~ 2.565 eV) and XX (~ 2.588 eV) complexes originating from the same NW-QD (fig. 6.3.0.(a)). This was attested by the linear and quadratic dependence of the integrated peak intensities on the excitation power, respectively (fig. 6.3.0.(b)). Besides, it was experimentally determined that both X and XX, originating from the same QDs, not only have identical polarization direction, as expected, but also similar degree of polarization ***[Aml 2012; Win 2007]***. That allows to determine if different emission lines are originating from the same QDs. As can be clearly seen in fig. 6.3.0.(c) both conditions are fulfilled. The biexciton binding energy was estimated to be -22.9 meV. Such large negative binding energy is in good agreement with the literature and is a sign of strong confinement potential ***[Aml 2014; Sim, 2008; Aml 2011]***.

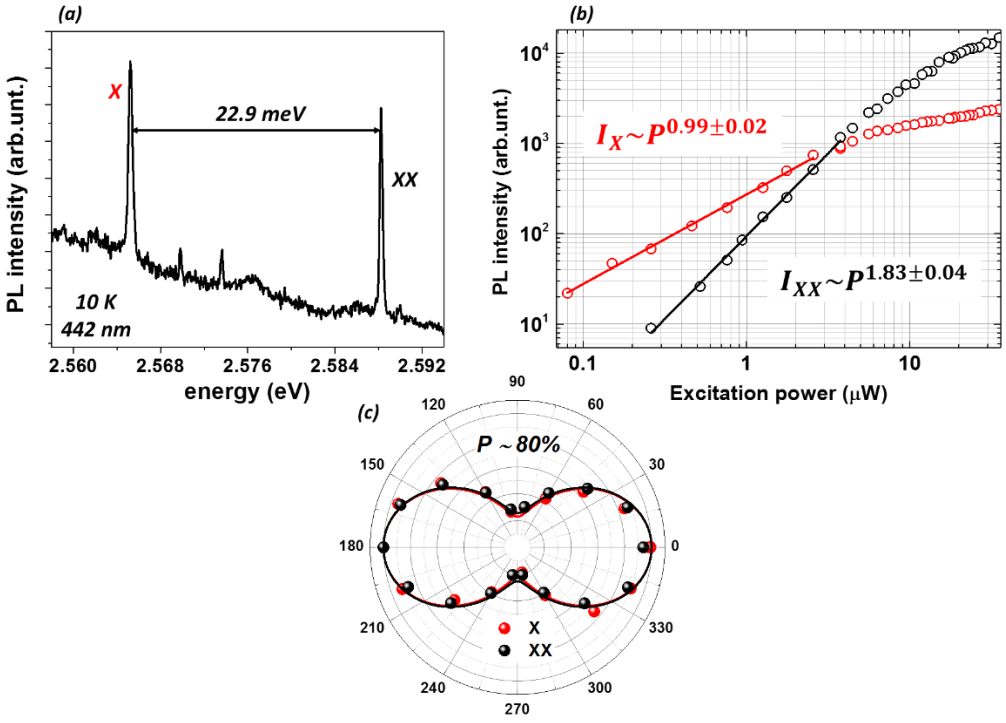

Fig. 6.3.0. (a) A μ-PL spectrum of targeted nanowire-QD. (b,c) Laser power dependence of integrated peak intensity (I_X and I_{XX}) and polar plots for the X and XX from (a), respectively. Solid lines in (c) are fit to the formula 4.2.0.

Once the SAW is applied, the emission lines exhibit a characteristic splitting into two components (fig. 6.3.1.(a)). As was already mentioned in Section 2.9.4. the SAW fields applied to a QW induce a splitting of PL peaks due to the modulation of the band gap. In the case of QDs the periodic SAW strain field modulates the optical transitions, resulting in the observed shift of the emission energy around its equilibrium position. In this context, the energy separation between split doublet lines reflects the difference between the transition energies corresponding to maximum compressive and tensile strain. These results indicate that SAW can be used for the in-situ fine-tuning of the QD emission energy within a bandwidth up to some 1.5 meV.

An acoustic excitation can produce sample heating and partially mask the SAW effect on PL emission ***[Cam 2003]***. In order to correct for this effect a series of differential PL experiments were performed. The laser and the RF signal were chopped at 400 Hz and duty cycle of 1:1. Such procedure allowed to separate fast effects induced by the SAW fields from slower ones induced by heating. By recording, for each acoustic power, the PL spectrum with the optical and rf excitations in-phase (SAW plus thermal effects) and out-of-phase (only thermal effects), we found no significant rf-induced thermal contribution on the PL peak position and intensity.

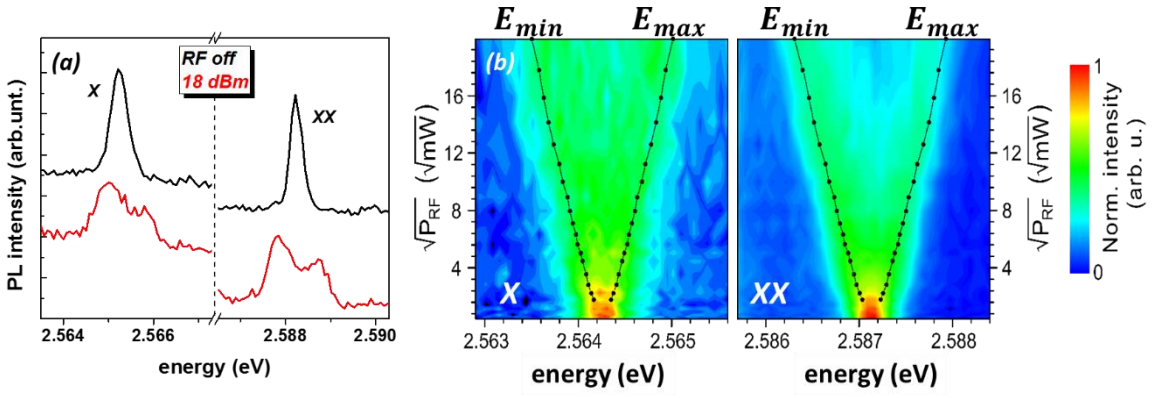

Fig. 6.3.1. (a) Low temperature time-averaged μ-PL spectra under cw excitation for a given NW-QD with (red) and without (black) SAW applied. The spectra are vertically shifted for clarity. (b) A false-color representation of the SAW-induced splitting of both excitonic lines under different RF powers applied. The black lines are fits to the equation 6.3.2.

Fig. 6.3.1.(b) shows false-color plots of the PL emission as a function of the acoustic amplitude (~square root of the applied RF power) for both exciton and biexciton lines. The energy splitting directly reflects the amplitude of the SAW-induced modulation of the QD energy levels. The actual strain value in the NW-QD was calculated using the experimentally obtained energy shifts for the highest acoustic power applied, the elastic stiffness constants (see Section 2.3.) and the deformation potentials ***[Lep 2013]*** for $In_xGa_{1-x}N$ (table 6.3.0.) with $x \approx 0.33$. The elastic stiffness constants for ternary alloy were estimated by Vegard's law, while deformation potentials were obtained using ***[Lep 2013]***:

$$D_i^{In_xGa_{1-x}N} = (1-x) * D_i^{GaN} + x * D_i^{InN} - b * x(1-x), \qquad \textbf{6.3.0.}$$

where D_i is the deformation potential (a_i or b_i from the table) and *b* is a bowing parameter.

parameters	GaN	InN	b	InGaN
a_1, eV	-6.01	-5.85	-0.202	-5.91
a_2, eV	-9.1	-2.93		-7.02
b_1, eV	-5.79	-2.7		-4.72
b_2, eV	3.11	1.51		2.63
C_{13}, GPa	103	92		99.4
C_{33}, GPa	405	224		345

*Table 6.3.0. The elastic stiffness constants and deformation potentials **[Lep 2013]** for $In_{0.3}Ga_{0.7}N$.*

Following the procedure from Ref. ***[Wag 2002; Sha 1996]*** the strain components along the SAW propagation direction (ϵ_{xx}) and perpendicular to it (ϵ_{zz}) can be estimated as:

$$\delta E = (a_1 + b_1) * \epsilon_{zz} + (a_2 + b_2) * \epsilon_{xx}, \qquad \textbf{6.3.1.}$$
$$\epsilon_{zz} = -\frac{2C_{13}}{C_{33}} * \epsilon_{xx},$$

where, $\delta E = (E_{max} - E_{min})/2$. In this way, neglecting the contribution from the SAW piezoelectric field, we obtained $\epsilon_{xx} = 0.04\%$ and $\epsilon_{zz} = 0.03\%$. Thus the dominant strain component is along the SAW propagation direction. The estimation of strain for $LiNbO_3$ gave $\epsilon_{xx} = 0.05\%$, indicating good mechanical coupling between the SAW and the targeted nanowire.

An asymmetry in the intensity of split PL doublets for both excitonic complexes towards minimum energy was observed (fig. 6.3.1.(a)). Such behavior was indeed already seen in InAs QDs ***[Gel 2008]***, GaAs QW ***[Als 2006; Sog 2001]*** and GaN films ***[Cam 2003]***. The authors indicated that the spectral modulation of the transition energy levels is mostly due to the SAW strain field, while the relative intensities of the split doublets is due to the SAW piezoelectric field. In particular, in QWs the relative intensities of the split PL components depend on the carrier distribution in the modulated 2D potential, which is controlled by the piezoelectric field ***[Sog 2001]***. In QDs the observed behavior could be ascribed to an effect of the SAW piezoelectric field on the QD charge population.

Additionally, the observed intensity correlation in the doublet asymmetry of X and XX further confirms the assignment of these lines. Some research groups ***[Gel 2008; Wei 2014; Wei1 2014]*** showed that there is an anti-correlation of intensities between the complexes with even (X, XX, etc.) and odd (trions) number of charges, thus making it an additional tool for identifying different charge emission lines.

We also performed calculations using the finite-element modeling for the 128° Y-cut $LiNbO_3$ layer, following the procedure developed in Ref. ***[Sog 2001; San 2004; Lim 2005]***, in order to gain insight on the relation between the piezoelectric field orientation and strain. The polarization resolved studies suggested that the targeted wire was oriented perpendicular to the SAW pathway. However, the exact orientation is difficult to determine, since the dispersion procedure resulted in the random orientation of wires, together with some bunching tendency. Nevertheless, the SEM image of the investigated area in fig. 6.1.0.(e) suggests the possible orientation of the targeted wire as upside down. The number of wires, responding to the SAW fields is scarce, meaning that coupling to acoustic waves is inefficient for the most frequent dispersion geometry (lying wires). On the other hand an “upside down” configuration should provide a better mechanical contact between the pyramidal nanowire top, containing the QDs, and the piezoelectric substrate. Thus the calculations were performed with the Z direction corresponding to the NW growth axis and X along the SAW propagation. The calculations were performed for the linear power density (i.e. the ratio between the acoustic power and the width of acoustic beam) of $P_\ell = 230\ W/m$. It is estimated as the real acoustic power divided by the IDT aperture: $P_\ell = \frac{r_a \times P_{RF}}{l_{IDT}}$. The use of P_ℓ rather than nominal RF power (i.e. the input electrical power applied to the IDT), allowed to make the calculation procedure independent on the IDT design and to take into account the coupling losses in the electrical setup.

The calculation results are presented in fig. 6.3.2. for the hydrostatic component of strain ($\epsilon_0 = \epsilon_{XX} + \epsilon_{YY} + \epsilon_{ZZ}$) and the three components of uniaxial strain (ϵ_{XX}, ϵ_{YY} and ϵ_{ZZ}). The dominant strain is along the SAW propagation direction (i.e. x-axis) and it alternates between compression

corresponding to $\epsilon_{XX} < 0$ and tension corresponding to $\epsilon_{XX} > 0$ (blue and violet areas in fig. 6.3.2., respectively). These phases of the SAW strain field (fig. 6.3.2. upper panel) coincide with the vertical components of the piezoelectric field, F_Z (fig. 6.3.2. lower panel). In particular, for the compressive strain $F_Z > 0$ and is oriented along the NW growth direction (i.e. along the internal built-in field). On the other hand, for the maximum tensile strain, $F_Z < 0$ and is opposite to the NW growth direction.

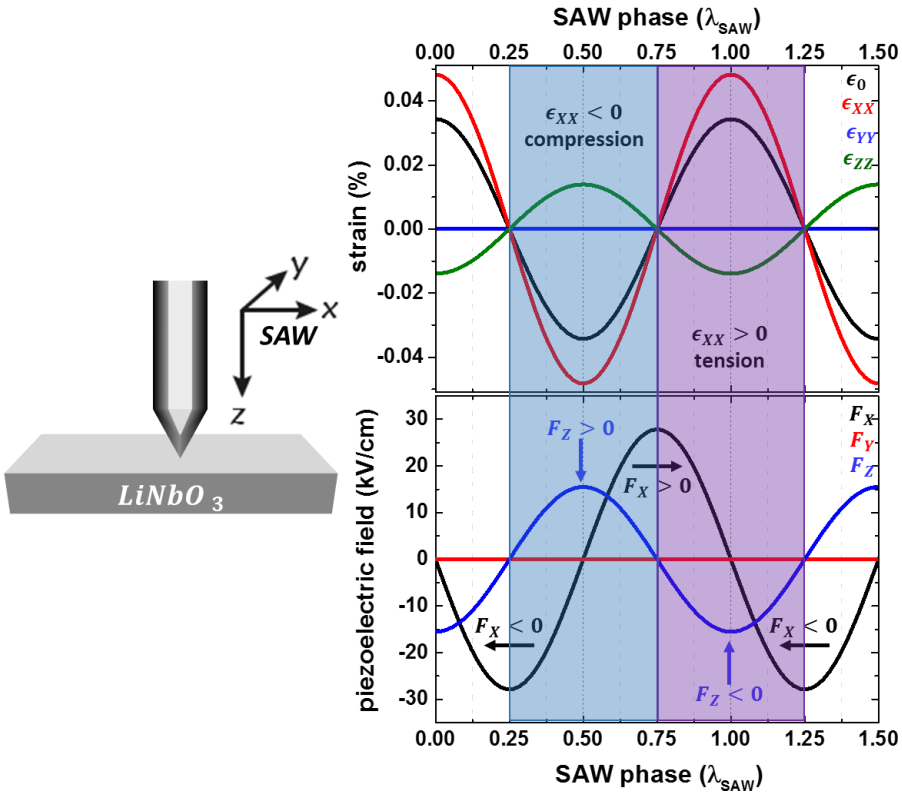

Fig. 6.3.2. The calculated SAW-induced strain (upper panel) and piezoelectric (lower panel) fields at the surface of the 128° Y-cut $LiNbO_3$ crystal. The arrows denote the field orientation. The calculations were done for the acoustic linear power density of 230 W/m. The sketch of NW-$LiNbO_3$ substrate configuration is depicted on the left.

The evolution of the spectra for both excitonic lines as a function of the SAW amplitude ($\sqrt{P_{RF}}$) is displayed in fig. 6.3.1.(b). It can be seen that the splitting of emission peaks increases with increasing the RF power applied to the IDT and reaches the maximum values of 1.51 meV for X and 1.62 meV for XX for this particular QD. Further insight onto the underlying mechanisms controlling the SAW-induced modulation of the excitonic energy levels can be gained by studying the dependence of this energy modulation on the acoustic amplitude. In order to get accurate values of the energy splittings these spectra were fitted with a Lorentzian function, taking into account the sinusoidal modulation induced by the SAW:

$$y(x, E_0, \delta E, w) = y_0 + \frac{1}{T}\int_0^T \left(\frac{2A}{\pi}\right) \frac{w}{4\left(x-(E_0+\delta E*\sin(\omega_{SAW}t))\right)^2+w^2}\,dt, \qquad \textbf{6.3.2.}$$

where E_0 is the transition energy in the absence of SAW (i.e. X and XX peak position), $\delta E = (E_{max} - E_{min})/2$ is the modulation amplitude, ω_{SAW} is the SAW frequency, w is FWHM of a given PL peak, A is the peak area and y_0 is the baseline. The resulting values of the energy splitting for both X and XX, obtained from the fit are plotted as a function of the SAW amplitude in fig. 6.3.3.(a) in double logarithmic scale. A linear trend for both lines can be seen over the entire investigated RF power range. Such behavior is consistent with the deformation potential coupling to the SAW strain field (ΔE_{strain}), which is expected to be dominant in the small RF power regime ***[Wei 2014; Pus 2015]***. The SAW piezoelectric field, on the contrary, produces spectral shifts associated with quantum confined Stark effect (ΔE_{QCSE}) and is generally quadratic with the SAW amplitude ***[Wei 2014]***. However, there are reports on a linear dependence of ΔE_{QCSE} for polar III-N QDs for an electric field applied parallel ***[Nak 2006; Jar 2008; Jar 2007; Rob 2005]*** to the QD polar axis. The linear dependence is due to the fact that the vertical component of the SAW-induced piezoelectric field adds to the built-in one. Thus the piezoelectric effect along the c-axis and the strain can have a similar effect on the modulation of the emission energy. That could, in principle, explain the slight sub-linear trend observed in fig. 6.3.3.(a).

However, the dominant strain component of the SAW field is along its propagation direction. So for the maximum tensile/compressive strain and vertical NW orientation, only transverse electric field (F_z) is present and can, in turn, change the internal built-in field (fig. 6.3.2.). We recorded the μ-PL spectra for different excitation powers with and without SAW applied (fig. 6.3.3.(c)) since the field parallel to the c-axis of QDs is expected to be partially screened under high optical pumping. No appreciable change was found in the SAW-induced exciton splitting over the broad range of excitation powers (red points in fig. 6.3.3.(c)), reaching well above the X and XX saturation limit. Note that in the absence of the SAW for the same optical power range there is a clear blueshift of the X peak (up to 300 μeV) (black points in fig. 6.3.3.(c)), evidencing partial screening of the internal built-in field. Hence, one can conclude that the electrical field, parallel to the c-axis of QDs has no measurable effect on the SAW induced energy splitting.

As for the lateral electric field, parallel to the SAW propagation direction, its influence can be excluded assuming the symmetry of the investigated QD around the c-axis. In this geometry there should be a blueshift observed for both field orientations (i.e. positive and negative) ***[Nak1 2006]***, which would result in the asymmetric splitting of emission peaks. This is contrary to the observed symmetric splitting of the X and XX lines around their unperturbed positions, when no SAW is applied (fig. 6.3.1.(b)). Thus the spectral behavior of X and XX within the investigated range of RF powers is mainly governed by deformation potential coupling with a possible minor contribution of linear QCSE.

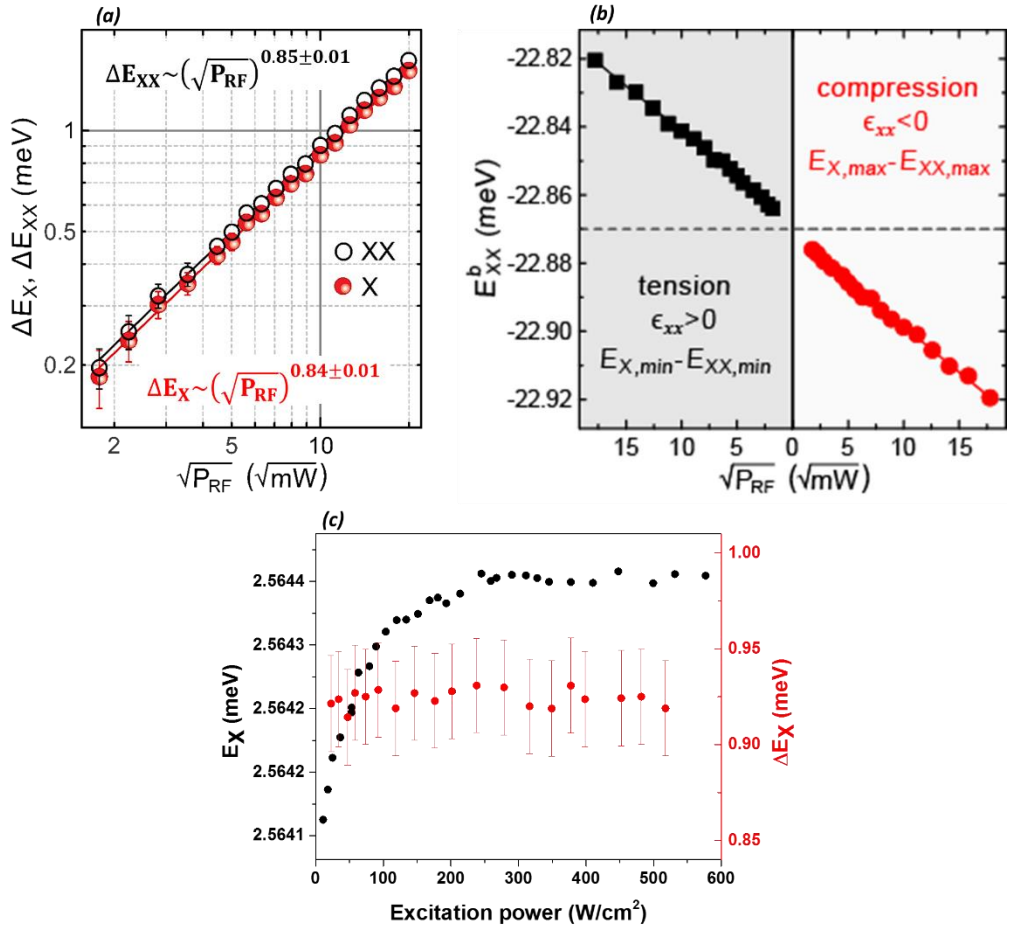

Fig. 6.3.3. (a) The energy splitting for exciton, ΔE_X, (red dots) and biexciton, ΔE_{XX}, (black circles) as a function of SAW amplitude, $\sqrt{P_{RF}}$, estimated from the fit presented in fig 6.3.1(b). The lines are linear fits to the experimental data. (b) The evolution of the biexciton binding energy, E^b_{XX}, for the tension (black) and compression (red) phases. (c) The exciton energy, E_X, in the absence of a SAW (black) and SAW-induced splitting of the X line upon SAW excitation at P_{RF} =21 dBm (red) as a function of laser excitation power.

The small difference between exciton and biexciton splitting in fig. 6.3.3.(a) can be explained by the SAW influence on the biexciton binding energy (E^b_{XX}). This effect is more clearly seen in fig. 6.3.3.(b), where E^b_{XX} is plotted as a function of the acoustic amplitude for the tensile ($E^b_{XX} = E^{min}_X - E^{min}_{XX}$) and compressive ($E^b_{XX} = E^{max}_X - E^{max}_{XX}$) strain (black and red circles respectively). The variation of the biexciton binding energy over the full investigated RF power range is within ~100 μeV. The simple way of describing E^b_{XX} is through the Coulomb interactions within the XX complex:

$$E^b_{XX} = 2J_{eh} - J_{ee} - J_{hh}, \qquad \textbf{6.3.3.}$$

where J_{eh} is the electron-hole Coulomb attraction and J_{ee} and J_{hh} are electro-electron and hole-hole Coulomb repulsions, respectively. Compression along the SAW pathway (perpendicular to

the QD polar axis) would result in the increase of the repulsive electron-electron and hole-hole interactions, thus reducing the biexciton binding energy (fig. 6.3.4.(right panel)). Tension applied in the same direction would lead to a reduction of both repulsion terms and, consequently, to the increase of E_{XX}^{b} (fig. 6.3.4.(left panel)). The opposite holds for the strain applied perpendicular to the SAW propagation direction (along the c-axis of the QD), which will mainly affect the attraction component. Similar results were reported for InGaAs/GaAs ***[Din 2010]***, GaN/AlN ***[Sim 2008]*** and GaN/AlGaN QDs ***[Aml 2011]***. Considering the vertical orientation of the NW, the experimental findings depicted in fig. 6.3.3.(b) are qualitatively consistent with the effect of lateral size variation of the QD confinement potential (i.e. in the plane perpendicular to the QD polar axis) on the biexciton binding energy, as reported in Refs. ***[Sim 2008; Aml 2011]***.

So the observed changes in the biexciton binding energy can be explained by the SAW-induced strain field as a dominant mechanism with possibly a minor contribution of the vertical component (F_z) of the SAW-induced piezoelectric field (along the QD polar axis) affecting the Coulomb interactions within the biexciton complex. It is worth noting that such SAW-governed tuning of the biexciton binding energy was achieved without any appreciable degradation of the emission, thus providing a reliable tool for the in-situ control of the exciton-biexciton system.

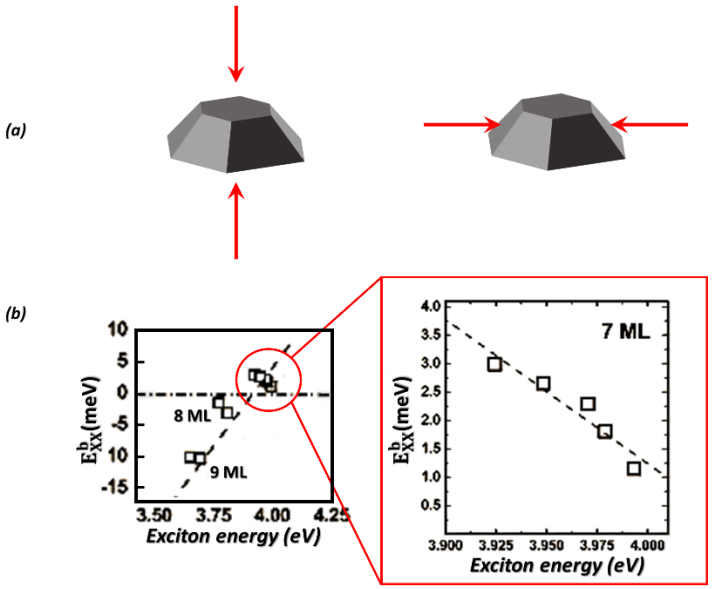

Fig. 6.3.4. (a) Schematics of strain applied along the QD polar axis and along the SAW propagation direction (perpendicular to the QD polar axis). (b) The biexciton binding energy as a function of the GaN/AlN QD emission energy for different vertical (left panel) and lateral (right panel) QD sizes ***[Sim 2008]****. Dashed lines are guide for the eyes. ML denotes monolayer.*

6.4 STROBOSCOPIC TECHNIQUES

The main difference between the SAW-induced (i.e. dynamic) and static modulation is its time and spatial dependence, which, in turn, allows to dynamically control structural, electronic and

optical properties of the material *[Pus 2015]*. The interplay between the two SAW contributions (i.e. strain and piezoelectric fields) makes it challenging to identify exactly what is the mechanism responsible for the interactions between the SAW and the photo-generated carriers. In order to try to clarify this issue we employed stroboscopic techniques. The detailed description of the experimental setup is given in Section 3.3.

6.4.1 CW optical excitation with stroboscopic detection

The stroboscopic detection allowed to probe the influence of the SAW strain field under constant optical pumping. The targeted wire was continuously pumped, while the detection was synchronized with the RF signal (for details concerning the synchronization see Section 3.3.2). The detection wavelength for the APD was determined by the spectrometer. In addition, the exit slit was chosen to be approximately one third of the peak splitting in the time-averaged spectra recorded on the CCD for each RF power. In this way only one component of the split doublet line (i.e. E_{min}, E_{middle} or E_{max}) was measured at the APD.

In fig. 6.4.0. the time-resolved photoluminescence (TRPL) corresponding to the three different spectral positions for both exciton and biexciton is presented. Both lines exhibit similar intensity oscillations following the SAW-induced sine type spectral modulation of the QD emission *[Gel 2008; Als 2001]*. The acoustic wave forces the QD to move in and out of the chosen spectral window, thus causing the repeatable variation in the detector count rate within each SAW cycle (fig. 6.4.0.(a-b)). As can be clearly seen from fig. 6.4.0.(c-d) the light detected at E_{min} and at E_{max} is out of phase and is oscillating with the SAW period, as expected. Instead, emission at the central energy (E_{middle}) oscillates with twice the SAW frequency, since the QD moves past this energy twice per SAW cycle. The visibility of the oscillations of the exciton is limited, because its signal to background ratio is smaller than for XX (see fig. 6.3.0.(a)). We can exclude any effects other than interactions with SAW, since the oscillations disappear once the acoustic frequency is out of the IDT resonance.

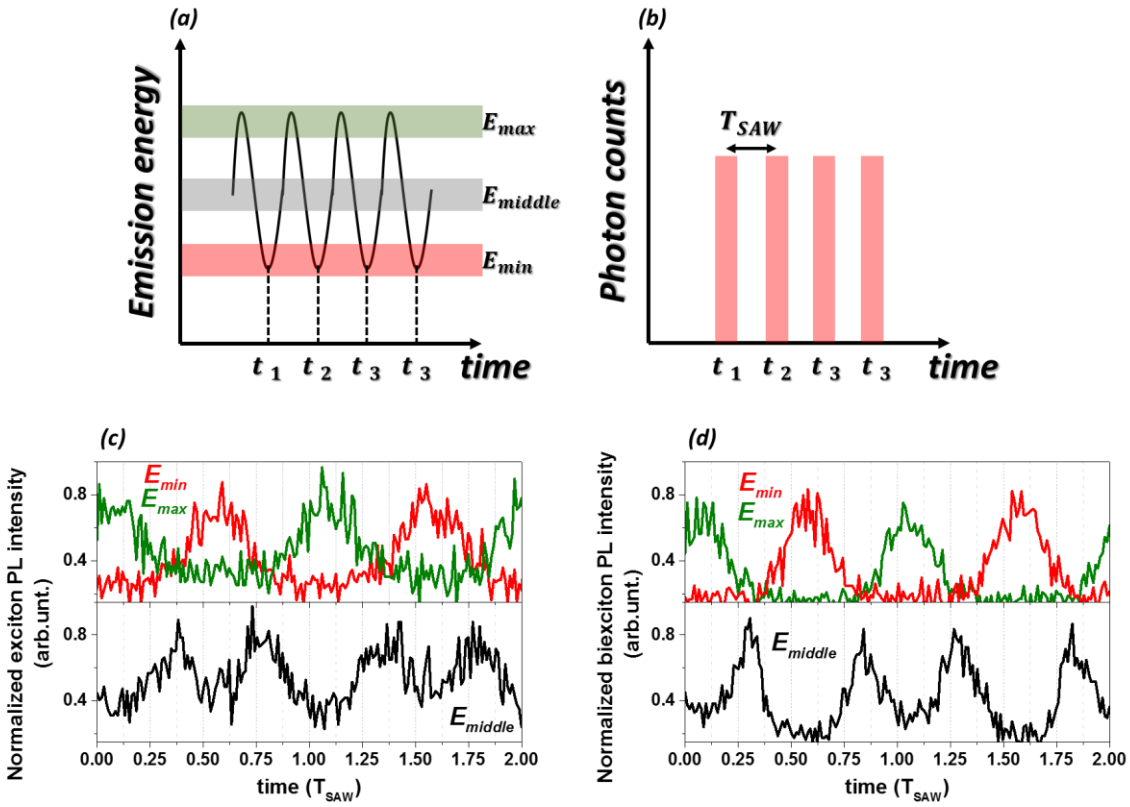

Fig. 6.4.0. (a) The schematics of the SAW-induced QD emission modulation as a function of time. Spectral detection window is indicated by filled rectangles labeled E_{min}, E_{middle} and E_{max}. (b) Temporal profile recorded at E_{min} spectral window. The PL intensity recorded under stroboscopic detection at minimum (red), maximum (green) and middle (black) spectral position for both exciton (c) and biexciton (d).

Also, varying the spectral detection window from E_{min} to E_{max} the time intervals between the two consequent PL pulses changes within the T_{SAW} range (fig. 6.4.1.).

Spectral filtering of the SAW-driven oscillation of the QD emission energy can be used to control the photon emission times. As was already shown for the InAs QDs ***[Gel 2008]*** such technique allows to produce the deterministic on-demand source of single photons without use of the pulsed laser. By increasing the SAW frequency, a high photon repetition rates (up to GHz range) can be achieved.

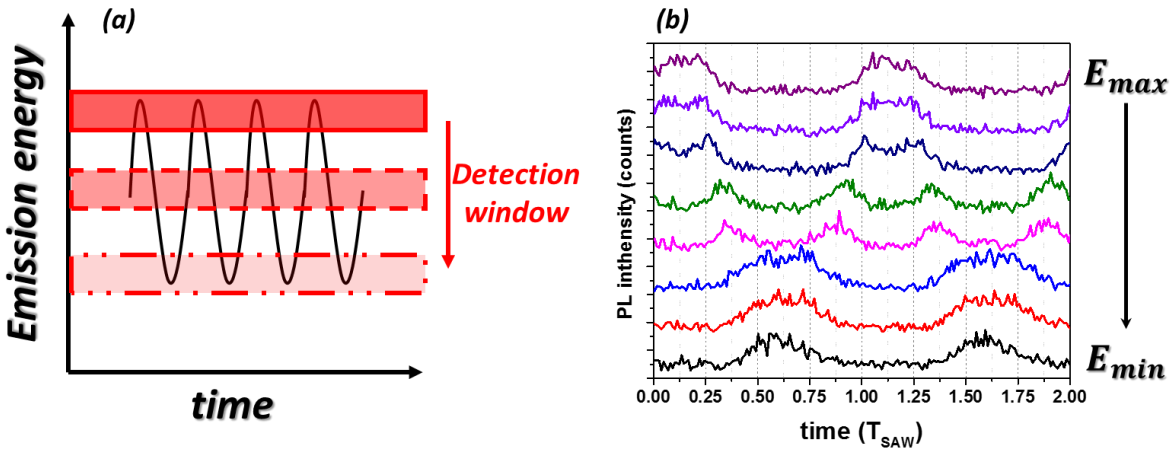

Fig. 6.4.1. (a) The schematics of the stroboscopic detection experiment. (b) The TRPL for exciton transition recorded at different spectral position of the detection window.

6.4.2 Stroboscopic pulsed optical excitation

In these experiments the targeted wire was pumped by a pulsed laser at a precise phase of the SAW cycle (details on the synchronization setup can be found in Section 3.3.1.). That allowed us to measure the optical response of the QD as a function of the SAW phase. Two types of the detectors were used: CCD camera for time-averaged and APD for time-resolved μ-PL detection. In the time-averaged measurements, the spectral resolution allowed to directly monitor the modulation of the emission lines, while in the TRPL experiments the temporal resolution gave an additional information about the SAW influence on the recombination processes.

6.4.2.1 SAW-induced spectral modulation in time-averaged detection.

The laser excitation at different SAW phases was achieved by delaying the laser trigger with steps of 200 ps. In this way, the full phase information over two acoustic periods was assessed. An example of the obtained results is presented in fig. 6.4.2. A clear sine-type spectral modulation for the XX with the SAW period can be seen, while the X shows a rather broad band emission independent of the SAW phase. Similar spectral modulation was also reported in III-As material system for QDs ***[Pus 2015; Sch 2015]***, nanocavities ***[Fuh 2011]***, quantum posts and wells ***[Vol 2011; Vol 2010]***. Völk and coworkers showed that the stroboscopic excitation combined with the time-averaged detection can be applied to resolve periodic SAW-driven processes only if the involved radiative transitions are faster than the half of the SAW period ($\tau_{PL} < \frac{T_{SAW}}{2}$). As shown in fig. 6.4.3. in the next section, decay times of the X and XX observed in TRPL experiments in the absence of the SAW are $\tau_x = 2.9$ ns and $\tau_{xx} = 0.8$ ns, respectively. The SAW period is ~3 ns, so $\tau_{xx} < T_{SAW}/2$ and the full phase information of the XX spectral position can be obtained (fig. 6.4.2.(b)). On the contrary, owing to its long lifetime $\tau_x \approx T_{SAW}$, the X emission is averaged over the whole spectral range of the SAW-induced splitting (fig. 6.4.2.(a)).

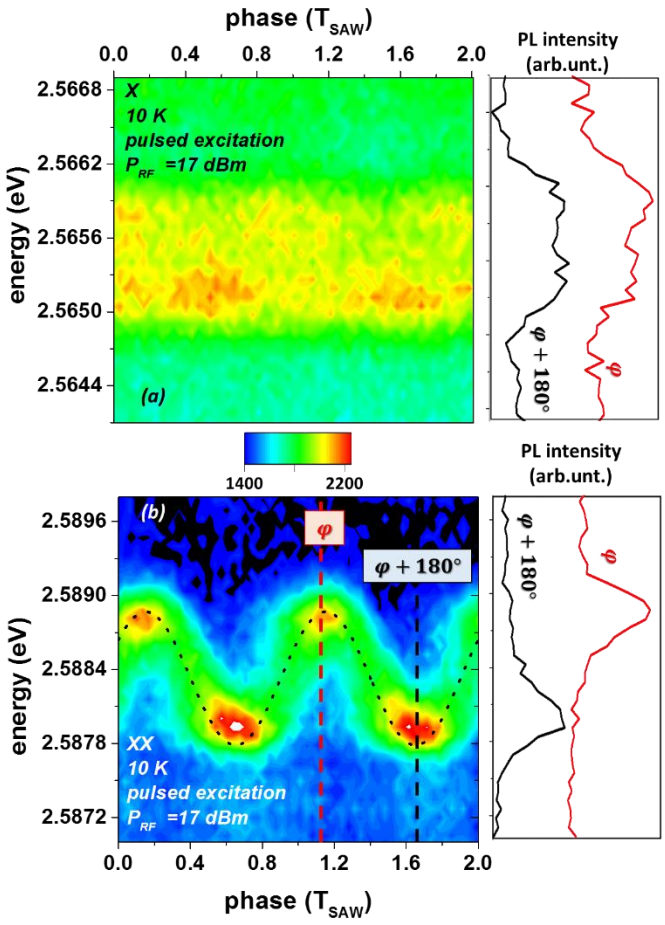

Fig. 6.4.2. A false-color representation of the SAW-induced spectral modulation as a function of the SAW phase for the exciton (a) and the biexciton (b) transitions. The black dot line in (b) represents a sine function. The right panels show the time-averaged μ-PL spectra excited at two opposite SAW phases (i.e. φ and φ + 180°) corresponding to the maximum and minimum transition energies, respectively.

6.4.2.2 SAW-induced spectral modulation in time-resolved detection

Contrary to the findings of the previous section, in time-resolved detection experiments, slow radiative processes with PL decay time constants of the order of the SAW period or longer should exhibit an acoustically-driven spectral modulation during the SAW cycle.

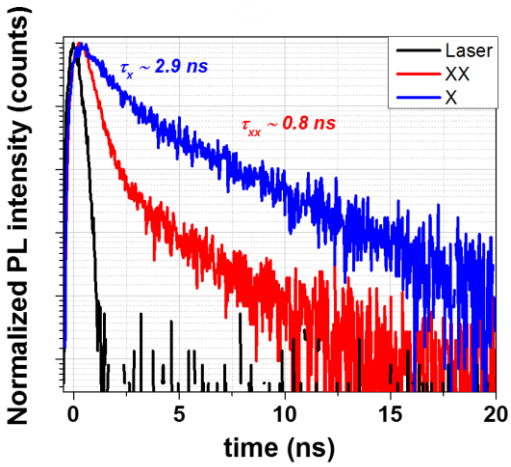

Fig. 6.4.3. Laser pulse (black) and TRPL of XX (red) and X (blue) in the absence of the SAW.

Thus, we also performed a series of time-resolved μ-PL measurements with stroboscopic optical excitation for different spectral positions within the split doublets (the spectral detection window bandwidth was chosen as described in Section 6.4.1.). In the absence of SAW, the X and XX decays are shown in fig. 6.4.3. Upon applying the SAW we can indeed clearly resolve for the exciton the spectral modulation during the decay at the time scales defined by the acoustic cycle (fig. 6.4.4.(a)). The same is not observed for the XX, since its lifetime is shorter than $T_{SAW}/2$ (fig. 6.4.4.(b)).

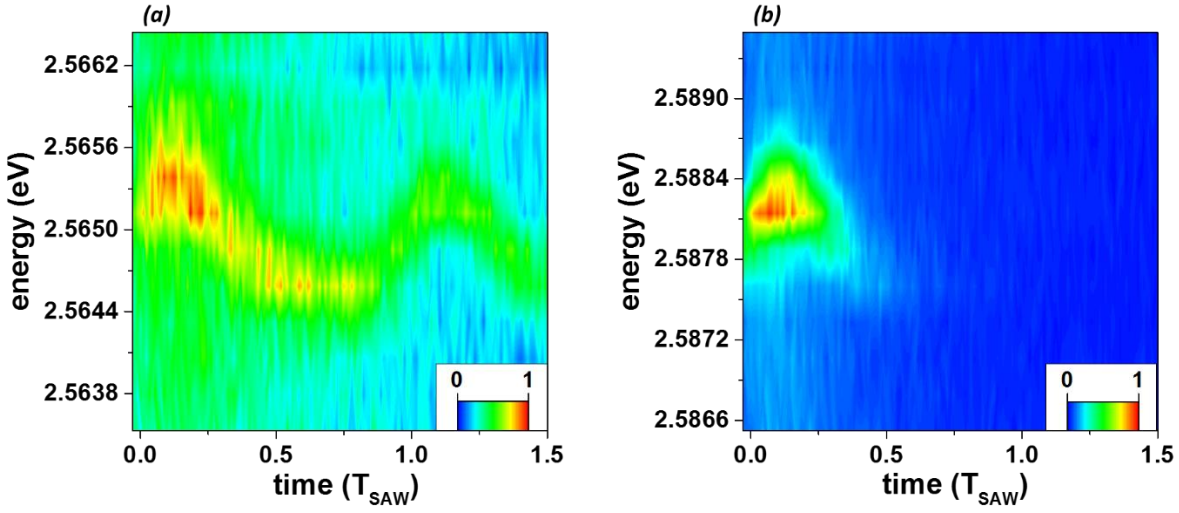

Fig. 6.4.4. A false-color representation of the time-resolved spectra for the exciton (a) and biexciton (b) excited at fixed SAW phase, corresponding to the E_{max}, for RF power 15 dBm.

Furthermore, we recorded the time-resolved traces for X and XX for a RF power of 18 dBm and plotted them as a function of the SAW period. The experiments were done with the spectrometer exit slit open to register the entire spectral modulation range. Clear intensity wiggles,

superimposed on the X decay and separated by the half of the SAW period (fig. 6.4.5.) were observed. This behavior can be explained by the SAW-induced piezoelectric field (fig. 6.4.5.(b) upper panel). It can be seen that wiggles are coincident in time with the maxima of the lateral piezoelectric field. We interpret the wiggles in terms of carrier injection, as explained in the sketch on fig. 6.4.6. The laser pulse creates a pool of carriers in the entire InGaN apex, which acts as a QW with QDs embedded in it. For both field directions both electrons and holes can be injected in the QD after every exciton recombination, thus giving rise to an increase in the emission probability.

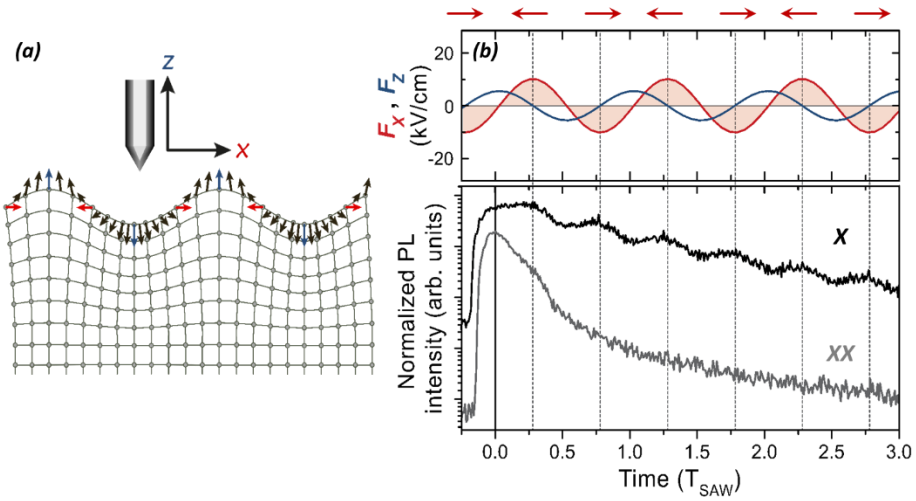

Fig. 6.4.5. (a) Propagating mechanical wave with its associated piezoelectric field (arrows). (b) Lateral (red) and vertical (blue) components of the calculated SAW-induced piezoelectric field (upper panel) and TRPL traces (lower panel) for the exciton (black) and biexciton (gray) for the RF power of 18 dBm. The traces are shifted vertically for clarity and time is given in units of the SAW period T_{SAW}.

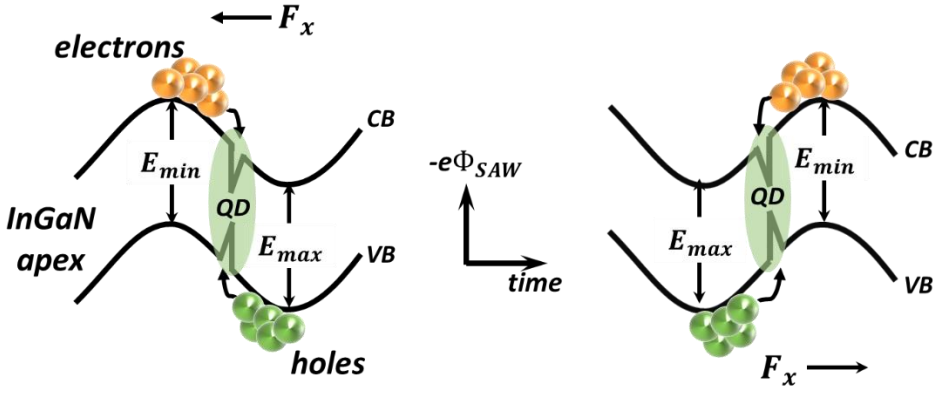

Fig. 6.4.6. Schematics of the SAW-induced band gap modulation of InGaN apex.

On the other hand, for the XX trace only one wiggle, delayed by $\sim T_{SAW}/4$ with respect to the photoexcitation, can be resolved before PL decays. Once XX is decayed, there are not enough carriers to form another biexciton until the next laser pulse comes. The amplitude of these oscillations scales with the strength of the piezoelectric field. For very low acoustic powers, the

acoustically induced piezoelectric field are weaker and these oscillations can no longer be resolved.

An example of similar experiments, carried out under higher SAW power ($P_{RF} = 21$ dBm), is presented in fig. 6.4.7. Most strikingly, at such high SAW amplitude the time-averaged spectral modulation of the biexciton showed a non-sinusoidal waveform (fig. 6.4.7.(a)). As the origin of such change, we can safely disregard other periodic signals, produced by any electrical component of our setup. This was attested by adding a narrow-band frequency filter directly before the IDTs, to suppress any signal other than the desired central frequency. However, even after adding such filter, the shape of the spectral modulation did not change. The other possibility to explain the observed changes in the waveform at high RF powers can be attributed to non-linearities of the SAW propagating on dispersive piezoelectric substrates (such as $LiNbO_3$). These can lead to non-linear dependence of the acoustic velocity on the SAW amplitude as well as frequency conversion resulting in generation of higher-order harmonics. Such substrate-related non-linear effects *[Kav 2000]* would then directly interact with a QD acting as a sensor deposited on the surface, resulting in a distorted opto-mechanical QD response, as recently shown in Ref. *[Sch 2015]*. The observed waveform can be reproduced by Fourier synthesis including the second harmonic of the fundamental frequency ω_1. The spectral modulation of fig. 6.4.7.(a) was fitted (dashed line) to the formula:

$$\delta E(t) = E_0 + E_1 \sin[\omega_1 t - \varphi_1] + E_2 \sin[2\omega_1 t - \varphi_2], \qquad \textbf{6.4.0}$$

where E_i are the amplitudes, and φ_i the phases of the two Fourier components.

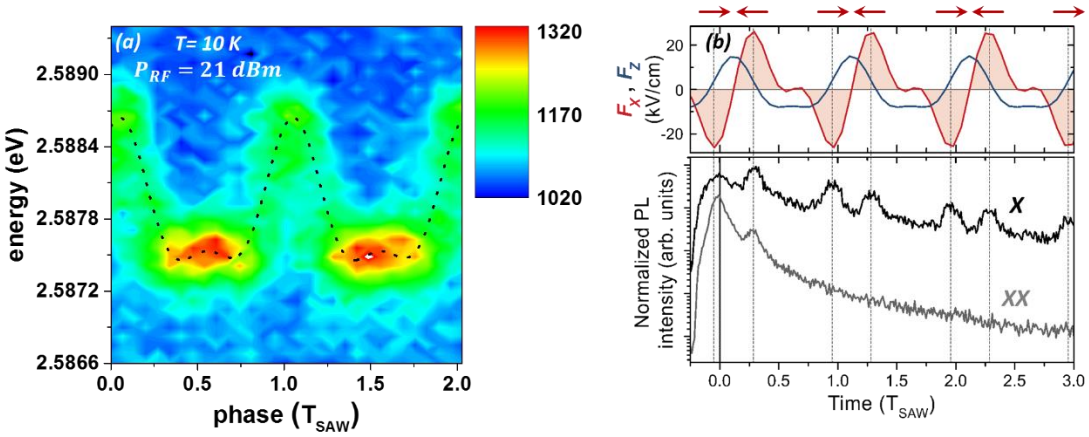

Fig. 6.4.7. (a) A false-color representation of the XX spectral modulation for RF power of 21 dBm as function of the SAW phase. Dashed black line is the fit to equation 6.4.0. (b) Lateral (red) and vertical (blue) components of calculated SAW electric field (upper panel) and TRPL traces (lower panel) for the exciton (black) and biexciton (gray) over three acoustic cycles The traces are vertically shifted for clarity. Phase delay and time axis in (a) and (b), respectively, are given in units of the SAW period T_{SAW}.

Again similar correlations between lateral field and emission intensity are observed for both exciton and biexciton lines in TRPL. The time separation between the wiggles also follows the

maxima of the lateral piezoelectric field. In this case the wiggles are not evenly spaced and are more intense, as expected for stronger lateral field.

Such non-linear acoustic effects can be used to deliberately engineer complex periodic waveforms, as recently demonstrated by additive Fourier synthesis in GaAs system *[Sch 2015]*. By combining the spectral filtering described in Section 6.4.1 with different waveforms, the time-dependent response of the QD sensor to the potential landscape created by the propagating acoustic wave can be further exploited to achieve more complex temporal sequence of the emitted photons. This could potentially lead to novel applications in quantum communication and information processing.

6.5 SUMMARY

In conclusion, we performed a detailed study of the acoustically induced modulation of the optical emission from excitonic complexes originated at the apices of QD-in-a-wire structures. It was found, that the SAW-induced strain field is responsible for the splitting of the PL emission lines into doublets in the time-averaged spectra.

The RF power dependence showed similar behavior for both excitonic lines, reaching modulation amplitudes of 1.51 meV for X and 1.62 meV for XX. The values of the energy splitting for both X and XX showed sub-linear dependence on the acoustic amplitude. Such sub-linear dependence can be explained by the deformation potential coupling with the possible small contribution of the linear Stark effect, expected for III-Nitrides systems. A small difference in the exciton and biexciton splitting with the RF power was attributed to the SAW effect on the biexciton binding energy. It was found that for compressive strain $\mathrm{E}_{\mathrm{XX}}^{\mathrm{b}}$ decreases linearly, while for tensile strain it increases with increasing the RF power. The overall tuning range of the biexciton binding energy was of the order of 100 μeV. The observed dependence was discussed in terms of Coulomb interactions inside the biexciton complex. No appreciable degradation of the biexcitonic emission was detected. Thus SAWs can be used as a reliable tool for the dynamic control of the excitonic complexes.

Furthermore, a series of stroboscopic experiments were conducted to study in details the influence of SAW-induced strain and piezoelectric fields on the QD optical properties. The cw optical excitation with the stroboscopic detection technique resulted in the periodic oscillation of the emission intensities at different spectral positions between E_{max}, and E_{min}. It was determined that the PL intensity oscillates with the SAW period with a phase difference of π between the maximum and minimum emission energy positions, while at the middle energy it oscillates with double of the SAW frequency. Such technique can help to produce a deterministic on-demand source of single photons without use of the pulsed laser. Also high photon repetition rates (up to GHz range) can be achieved by increasing the SAW frequency.

The stroboscopic excitation allowed to resolve the full SAW-driven spectral and temporal dynamics. A sine-type modulation of the XX emission energy was observed for intermediate RF powers in time-averaged spectra, and, in the same time, the X showed a broad band emission independent of the SAW phase. On the contrary, in time-resolved spectra only the exciton showed the sine-type modulation. Such differences were discussed in terms of the relation between the emission lifetime and the SAW period. It was found that if $\tau < \frac{T_{SAW}}{2}$, as was the case for XX, than it is possible to resolve the spectral modulation in time-averaged detection. On the other hand, when $\tau \geq \frac{T_{SAW}}{2}$, as was for X, the spectral modulation can only be observed in time-resolved detection.

The study of X and XX decays as a function of the SAW phase resulted in periodic intensity oscillations. They were assigned to the *e-h* pair injection into the QD from the surrounding InGaN region due to the lateral component of the piezoelectric field. For high acoustic power the sine-type modulation changed to a more complex waveform, which was assigned to the non-linearities associated with the SAW propagation in the $LiNbO_3$ substrate.

6.6 FUTURE WORK

As in the present work only few NWs were coupled to the acoustic waves, it became important to look for ways to improve the coupling efficiency. One of the ways to do that was to embed the wires into the piezoelectric material. Thus, new samples were prepared (fig. 6.6.0.) by Mr. Seidel from the technical department at PDI, Berlin (Germany). Silicon dioxide (SiO_2) was used as a piezoelectric material. A thin layer of Hydrogen silsesquioxane (HSQ) was deposited by spin coating between the two IDTs on the $LiNbO_3$ substrate on top of dispersed nanowires. Then it was baked to obtain the layer of SiO_2. The nanowires from the same batch were used for dispersion. The quality and density of the dispersion was monitored by optical microscopy as can be seen in fig. 6.6.0.(b). Finally, the position of the NWs immersed into SiO_2 was mapped by SEM (fig. 6.6.0.(c)). Bonding of IDT pads to the chip metal pins was done by Mrs. M. C. Sabido Siller at the *UPM-ISOM*, Madrid (see Chapter 3 for details). The preliminary optical characterization revealed that the number of NWs, showing acoustically modulated emission was indeed higher. It was also noted, that the same range of acoustic powers produced a huge shift of the PL emission, caused by the heating of the SiO_2 layer. Thus the range of both laser and acoustic powers had to be carefully chosen to avoid sample damaging due to excessive heating.

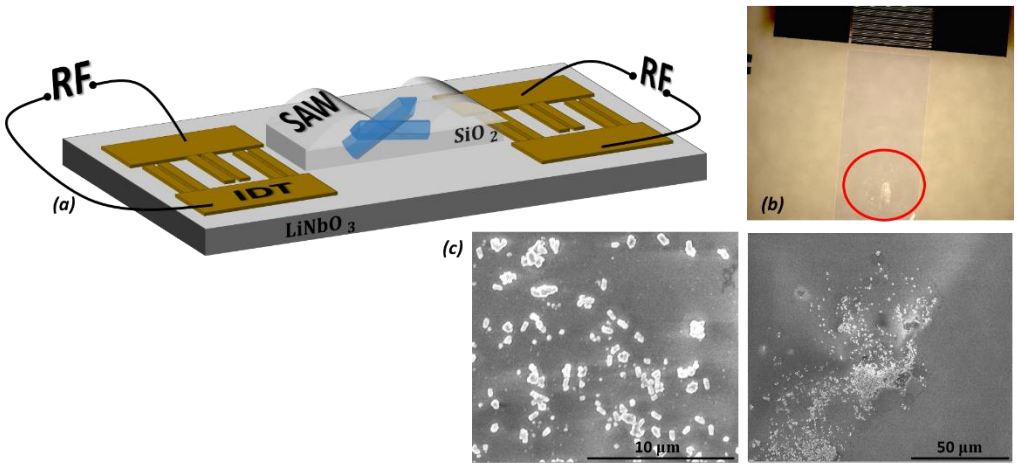

Fig. 6.6.0. (a) A sketch of the sample. (b) Optical microscopy image of the sample surface after processing. (c) SEM mapping of dispersed nanowires.

The second line suggested for future investigation is to study polarization properties of the emission upon acoustic excitation. As was already discussed in Section 2.7.2. the polarization properties of III-Nitride QDs are sensitive to the applied strain. Any variation of the in-plane anisotropy could result in the change of the polarization degree. Thus, the use of SAW is an important step towards the in-situ control of the photon polarization state, which has not yet been achieved in III-N QD systems and is required for many quantum information processing schemes, including quantum key distribution and linear optical quantum computing using photonic qubits. In this context, the SAW induced strain and piezoelectric fields can be employed to control the polarization degree (P_X) of the investigated QD-in-a-wire structures. The preliminary results indeed showed a clear reduction of P_X for the excitonic transition for both maximum compressive and tensile strain with increasing the RF power (fig. 6.6.1.). The mechanism leading to such effect is not yet understood, especially considering that the acoustic strain alone cannot be responsible for this behaviour since compressive and tensile strain are expected to produce changes of opposite signs in the polarization degree, which is contrary to our results. This suggests that the origin is the piezoelectric field produced by the SAW which, irrespective of the field orientation, can have an effect on the in-plane QD anisotropy and the resulting mixing of valence band states, which governs the polarization degree of excitonic transitions in wurtzite III-Nitride QDs. Further experimental and theoretical investigations are under way.

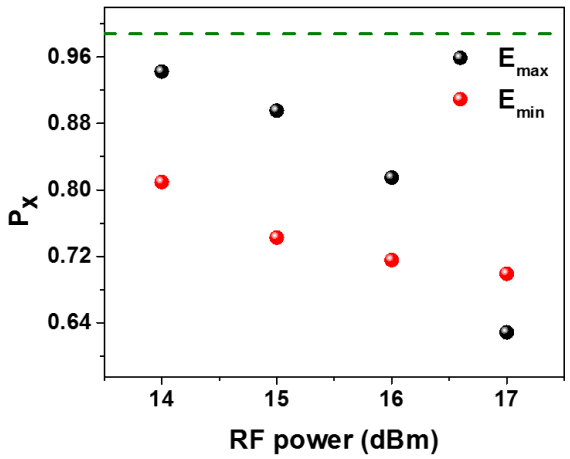

Fig. 6.6.1.The exciton polarization degree (P_x) as function of RF power for the maximum tension (red circles) and compression (black circles). The green dashed line denotes the polarization degree for no RF signal applied.

References

[Als 2001] Alsina, F., Santos, P., Hey, R., García-Cristóbal, A. & Cantarero, A. Dynamic carrier distribution in quantum wells modulated by surface acoustic waves. *Phys. Rev. B* **64,** 41304 (2001).

[Als 2006] Alsina, F., Stotz, J. A. H., Hey, R. & Santos, P. V. Radiative recombination during acoustically induced transport in GaAs quantum wells. *J. Vac. Sci. Technol. B Microelectron. Nanom. Struct.* **24,** 2029 (2006).

[Aml 2011] Amloy, S., Yu, K. H., Karlsson, K. F., Farivar, R., Andersson, T. G. & Holtz, P. O. Size dependent biexciton binding energies in GaN quantum dots. *Appl. Phys. Lett.* **99,** (2011).

[Aml 2012] Amloy, S., Karlsson, K. F., Andersson, T. G. & Holtz, P. O. On the polarized emission from exciton complexes in GaN quantum dots. *Appl. Phys. Lett.* **100,** 21901 (2012).

[Aml 2014] Amloy, S., Karlsson, K. F., Eriksson, M. O., Palisaitis, J., Persson, P. O. Å., Chen, Y. T., Chen, K. H., Hsu, H. C., Hsiao, C. L., Chen, L. C. & Holtz, P. O. Excitons and biexcitons in InGaN quantum dot like localization centers. *Nanotechnology* **25,** 495702 (2014).

[Cam 2003] Camacho, J., Santos, P. V., Alsina, F., Ramsteiner, M., Ploog, K. H., Cantarero, A., Obloh, H. & Wagner, J. Modulation of the electronic properties of GaN films by surface acoustic waves. *J. Appl. Phys.* **94,** 1892–1897 (2003).

[Din 2010] Ding, F., Singh, R., Plumhof, J. D., Zander, T., Křápek, V., Chen, Y. H., Benyoucef, M., Zwiller, V., Dörr, K., Bester, G., Rastelli, A. & Schmidt, O. G. Tuning the Exciton Binding Energies in Single Self-Assembled InGaAs/GaAs Quantum Dots by Piezoelectric-Induced Biaxial Stress. *Phys. Rev. Lett.* **104,** 67405 (2010).

[Fuh 2011] Fuhrmann, D. A., Thon, S. M., Kim, H., Bouwmeester, D., Petroff, P. M., Wixforth, A. & Krenner, H. J. Dynamic modulation of photonic crystal nanocavities using gigahertz acoustic phonons. *Nat. Photonics* **5,** 605–609 (2011).

[Gel 2008] Gell, J. R., Ward, M. B., Young, R. J., Stevenson, R. M., Atkinson, P., Anderson, D., Jones, G. A. C., Ritchie, D. A. & Shields, A. J. Modulation of single quantum dot energy levels by a surface-acoustic-wave. *Appl. Phys. Lett.* **93,** 81115 (2008).

[Jar 2007] Jarjour, A. F., Oliver, R. A., Tahraoui, A., Kappers, M. J., Humphreys, C. J. & Taylor, R. A. Control of the oscillator strength of the exciton in a single InGaN-GaN quantum dot. *Phys. Rev. Lett.* **99,** 1–4 (2007).

[Jar 2008] Jarjour, A. F., Oliver, R. A., Tahraoui, A., Kappers, M. J., Taylor, R. A. & Humphreys, C. J. Experimental and theoretical study of the quantum-confined Stark effect in a single InGaN/GaN quantum dot under applied vertical electric field. *Superlattices Microstruct.* **43,** 431–435 (2008).

[Kav 2000] Kavalerov, V., Fujii, T. & Inoue, M. Observation of highly nonlinear surface-acoustic waves on single crystal lithium–niobate plates by means of an optical sampling probe. *J. Appl. Phys.* **87,** 907 (2000).

[Lep 2013] Łepkowski, S. P., Gorczyca, I., Stefańska-Skrobas, K., Christensen, N. E. & Svane, A. Deformation potentials in AlGaN and InGaN alloys and their impact on optical polarization properties of nitride quantum wells. *Phys. Rev. B - Condens. Matter Mater. Phys.* **88,** (2013).

[Lim 2005] Lima, M. M. & Santos, P. V. Modulation of photonic structures by surface acoustic waves. *Reports Prog. Phys.* **68,** 1639–1701 (2005).

[Nak 2006] Nakaoka, T., Kako, S. & Arakawa, Y. Quantum confined Stark effect in single self-assembled GaN/AlN quantum dots. *Phys. E Low-dimensional Syst. Nanostructures* **32,** 148–151 (2006).

[Nak1 2006] Nakaoka, T., Kako, S. & Arakawa, Y. Unconventional quantum-confined Stark effect in a single GaN quantum dot. *Phys. Rev. B* **73,** 121305 (2006).

[Pus 2015] Pustiowski, J., Müller, K., Bichler, M., Koblmüller, G., Finley, J. J., Wixforth, A. & Krenner, H. J. Independent dynamic acousto-mechanical and electrostatic control of individual quantum dots in a LiNbO3-GaAs hybrid. *Appl. Phys. Lett.* **106,** 13107 (2015).

[Rob 2005] Robinson, J. W., Rice, J. H., Lee, K. H., Na, J. H., Taylor, R. A., Hasko, D. G., Oliver, R. A., Kappers, M. J., Humphreys, C. J. & Briggs, G. A. D. Quantum-confined Stark effect in a single InGaN quantum dot under a lateral electric field. *Appl. Phys. Lett.* **86,** 213103 (2005).

[San 2004] Santos, P., Alsina, F., Stotz, J., Hey, R., Eshlaghi, S. & Wieck, A. Band mixing and ambipolar transport by surface acoustic waves in GaAs quantum wells. *Phys. Rev. B* **69,** 1–11 (2004).

[Sch 2015] Schülein, F. J. R., Zallo, E., Atkinson, P., Schmidt, O. G., Trotta, R., Rastelli, A., Wixforth, A. & Krenner, H. J. Fourier synthesis of radiofrequency nanomechanical pulses with different shapes. *Nat. Nanotechnol.* **10,** 512–516 (2015).

[Sha 1996] Shan, W., Hauenstein, R., Fischer, A., Song, J., Perry, W., Bremser, M., Davis, R. & Goldenberg, B. Strain effects on excitonic transitions in GaN: Deformation potentials. *Phys. Rev. B* **54,** 13460–13463 (1996).

[Sim 2008] Simeonov, D., Dussaigne, A., Butté, R. & Grandjean, N. Complex behavior of biexcitons in GaN quantum dots due to a giant built-in polarization field. *Phys. Rev. B - Condens. Matter Mater. Phys.* **77,** 1–5 (2008).

[Sog 2001] Sogawa, T., Santos, P., Zhang, S., Eshlaghi, S., Wieck, A. & Ploog, K. Dynamic band-structure modulation of quantum wells by surface acoustic waves. *Phys. Rev. B* **63,** 3–5 (2001).

[Vol 2010] Völk, S., Schülein, F. J. R., Knall, F., Reuter, D., Wieck, A. D., Truong, T. A., Kim, H., Petroff, P. M., Wixforth, A. & Krenner, H. J. Enhanced Sequential Carrier Capture into Individual Quantum Dots and Quantum Posts Controlled by Surface Acoustic Waves. *Nano Lett.* **10,** 3399–3407 (2010).

[Vol 2011] Völk, S., Knall, F., Schülein, F. J. R., Truong, T. A., Kim, H., Petroff, P. M., Wixforth, A. & Krenner, H. J. Direct observation of dynamic surface acoustic wave controlled carrier injection into single quantum posts using phase-resolved optical spectroscopy. *Appl. Phys. Lett.* **98,** 23109 (2011).

[Wag 2002] Wagner, J.-M. & Bechstedt, F. Properties of strained wurtzite GaN and AlN: Ab initio studies. *Phys. Rev. B* **66,** 115202 (2002).

[Wei 2014] Weiß, M., Kinzel, J. B., Schülein, F. J. R., Heigl, M., Rudolph, D., Morkötter, S., Döblinger, M., Bichler, M., Abstreiter, G., Finley, J. J., Koblmüller, G., Wixforth, A. & Krenner, H. J. Dynamic acoustic control of individual optically active quantum dot-like emission centers in heterostructure nanowires. *Nano Lett.* **14,** 2256–2264 (2014).

[Wei1 2014] Weiß, M., Schülein, F. J. R., Kinzel, J. B., Heigl, M., Rudolph, D., Bichler, M., Abstreiter, G., Finley, J. J., Wixforth, A., Koblmüller, G. & Krenner, H. J. Radio frequency occupancy state control of a single nanowire quantum dot. *J. Phys. D. Appl. Phys.* **47,** 394011 (2014).

[Win 2007] Winkelnkemper, M., Seguin, R., Rodt, S., Schliwa, A., Reißmann, L., Strittmatter, A., Hoffmann, A. & Bimberg, D. Polarized emission lines from A - And B -type excitonic complexes in single InGaN/GaN quantum dots. *J. Appl. Phys.* **101,** 1–5 (2007).

[Yam 1992] Yamanouchi, K., Lee, C. H. S., Yamamoto, K., Meguro, T. & Odagawa, H. GHz-range low-loss wide band filter using new floating electrode type unidirectional transducers. *IEEE 1992 Ultrason. Symp. Proc.* 139–142 (IEEE, 1992).

7 CHAPTER. CONCLUSIONS

Ordered arrays of hexagonal GaN nanowires including InGaN quantum dots grown by plasma-assisted molecular beam epitaxy were investigated in this Thesis. The optical properties of the InGaN quantum dots formed on the polar, semi-polar and non-polar planes were studied. For single nanowire spectroscopy, nanowires were removed from their native substrate and dispersed onto a silicon wafer. A metal grid, patterned on the silicon surface, facilitated the access to specific nanowires. The main conclusions are divided in two parts, corresponding to the polar and semi-/non-polar QDs, followed by the final remarks:

- InGaN/GaN polar QDs

  - ✓ The structural analysis, optical properties and photon statistics of InGaN QDs formed in InGaN/GaN disk-in-a-wire structures were investigated. Structural analysis made by spatially and spectrally resolved cathodoluminescence revealed the formation of the two distinct InGaN regions inside the nanowire tip. The thickest one is formed on the polar plane (wire apex), and have the highest In concentration. The second InGaN region is formed on the semi-polar side facets of the nanowire. The cathodoluminescence line scan, recorded at different wire heights, revealed the non-uniform distribution of In content. The low temperature micro-photoluminescence spectroscopy confirmed CL findings, revealing similar broad emission bands. The origin of these bands was discussed in terms of In incorporation and differences in the electric field for the crystallographic planes with different polarities.

  - ✓ Additionally the emission from the top part of InGaN nanodisk (polar region) exhibits sharp and intense peaks superimposed on a broad background. The sharp lines were attributed to QD-like confinement potentials formed by random In fluctuations and the background – to the emission from the surrounding InGaN QW-like region. The μ-PL spectra recorded for single wires showed occasionally more than one emission peak confirming the suggested origin of such QDs. The QDs emit in the visible spectral range and are observable up to 80 K. Most of the investigated emission lines have a high degree of linear polarization with random polarization direction. Such strong linear polarization is of great importance for numerous applications in the field of quantum information processing (e.g. quantum key distribution and linear optical quantum computing).The observed peaks were assigned to excitons and biexcitons, as attested by the power dependence of the corresponding integrated peak intensity. No fine structure splitting was detected. The exciton decay times, measured by time-resolve μ-PL, were in the nanosecond range.
    The single photon performance of the nanowire-QDs was demonstrated by the strong antibunching observed in photon correlation measurements for two nanowire

geometries (standing, or as-grown, wires and single lying wires). The second order correlation function at zero time delay after the correction procedure was well below the 0.5 threshold for both standing and lying wires, thus proving the single photon nature of the emitted light. The exciton decay rate was estimated from the power dependent autocorrelation measurements under cw excitation for single lying nanowires. The obtained value was in the GHz range and in good agreement with the direct measurement of exciton lifetime by time-resolved μ-PL. Such single photon emitters are very attractive and desirable for high-frequency quantum information processing applications. Additionally, the absorption cross-section was estimated from the same power dependent autocorrelation measurements and its estimated value was among the highest reported for QDs.

- ✓ The modulation of the emission energies induced by surface acoustic waves for both exciton and biexciton, was achieved. It was determined that the SAW-induced strain field is responsible for the splitting of exciton and biexciton peaks into doublets in the time-averaged spectra. The modulation amplitude reaches 1.51 meV for the exciton and 1.62 meV for the biexciton for the highest acoustic power applied. The sub-linear dependence of the energy splitting on SAW amplitude for both emission lines was explained by deformation potential coupling with a possible contribution of the linear quantum confined Stark effect, expected for III-Nitrides. A SAW-induced modulation of the biexciton binding energy up to 100 μeV was also achieved without any appreciable degradation of biexciton emission, thus allowing the in-situ control of the exciton-biexciton system. It was found that for increasing acoustic power the biexciton binding energy decreases linearly for compressive and increases for tensile strain. Such behavior was discussed in terms of Coulomb interactions inside the biexciton complex.

- ✓ The use of different stroboscopic techniques allowed to observe the emission energy oscillations of the exciton and the biexciton.The latter is observed in time-averaged μ-PL spectra, while the exciton energy oscillations are observed in time-resolved μ-PL spectra. This difference was explained by the ratio between the lifetime of the emitted photon and the SAW half of period. The decay of the emission intensity for both excitonic complexes were studied for various SAW phases revealing periodic intensity oscillations. These oscillations were assigned to the electron-hole pair injection into the QD from the surrounding InGaN region due to the lateral component of the SAW-induced piezoelectric field.

◆ InGaN/GaN semi-polar and non-polar QDs

- ✓ In coreshell nanowire, QDs were formed also in semi-polar and non-polar surfaces (in addidion to the polar ones) of the InGaN region. Their optical properties were investigated by means of μ-PL and CL spectroscopy, revealing three emission bands,

corresponding to the three orientations. The polar QDs are emitting in the visible, semi-polar QDs in the violet and non-polar ones in the ultraviolet spectral range. The difference in the QD emission energy was discussed in terms of the In content, the geometry (size/shape), the confinement and the effect of the piezoelectric field. All three types of QDs have also high degree of linear polarization and showed no fine structure splitting. The random polarization direction, found for all investigated QDs, is consistent with the In fluctuations as an origin of such emission centers. The decay times were in the picosecond range for SP and NP QDs and followed the sequence: $\tau_{NP} < \tau_{SP} < \tau_{polar}$. A tendency to shorter lifetimes for smaller QDs (emitting at higher energy) was observed. Moreover, semi-polar QDs showed stronger size dependence than non-polar ones. Such difference in slopes was explained by the smaller effect of the piezoelectric field in non-polar QDs, since in this case the internal electric field is in the m-plane and affects only the electron-hole lateral separation, while the vertical confinement is fixed by the GaN barriers.

The non-classical nature of the emitted light was attested by HBT interferometry. The values of the second order correlation function at zero time delay after correction procedure were below the two photon threshold for QDs of all polarities

- Final remark

A high linearly polarized disk-in-a-wire SPS emitting in the visible spectral range and a multicolor coreshell SPS, spanning from ultraviolet to visible, both operating in the GHz range, were obtained. The low values of the second order correlation function at zero time delay for these SPSs opens an opportunity for the realization of high speed quantum information processing devices. Moreover, their integration into the nanowires facilitates its transfer and combination with other components of on-chip optoelectronic devices. The high polarization degree makes these SPSs an attractive tool for quantum key distribution, quantum cryptography and linear optical quantum computing applications. Also, their combination with the SAW technology opens the possibility of the dynamic on-demand control of the optical properties of the single photon emitter.

ABBREVIATIONS

ADC	analog to digital converter
APD	avalanche photo diode
BS	beam splitter
BW	bandwidth
CB	conduction band
CCD	charged coupled device
CFD	constant fraction discriminator
CL	cathodoluminescence
CW	continuous wave
CWL	central wavelength
DUT	device under testing
e-h pair	electron-hole pair
F	focal length
FSS	fine structure splitting
FWHM	full width at half maximum
HAADF	High Angle Annular Dark Field
He	helium
HBT	Hanbury Brown and Twiss
HRTEM	high resolution transmission electron microscope
IDT	interdigital transducer
IL	insertion losses
IR	infrared
IRF	instrument response function
LED	light emitting diode
μ-PL	micro-photoluminescence
ML	monolayer
MOCVD	metal organic chemical vapor deposition
NA	numerical aperture
NBE	near band edge emission
NP	non-polar
NW	nanowire
P	polar
PAMBE	plasma-assisted molecular beam epitaxy
PL	photoluminescence
PMT	photomultiplier tube
R	reflection
RF	radio frequency
RL	return losses
SA	self-assembled
SAG	selective area growth
SAW	surface acoustic wave
SEM	scanning electron microscope
Si	silicon
SK	Stranski-Krastanow
SP	semi-polar
SPAD	silicon avalanche photodiode
SPS	single photon source
STEM	scanning transmission electron microscope
T	transmission
TAC	time to amplitude converter
TCSPC	time-correlated single photon counting
Ti	titanium
TRPL	time-resolved photoluminescence
TTTR	time-tagging time-resolved
QCSE	quantum confined Stark effect
QD	quantum dot
QW	quantum well
UV	ultraviolet
VB	valence band
VIS	visible
VNA	vector network analyzer
VW	Volmer-Weber
WD	working distance
X (XX)	exciton (biexciton)
III-N	III-Nitride
3(2,1,0)D	3(2,1,0) dimension

LIST OF FIGURES

LIST OF TABLES

LIST OF PUBLICATIONS

PUBLICATIONS RELATED TO THIS THESIS

- S. Lazić, E. Chernysheva, Ž. Gačević, N. García-Lepetit, H. P. van der Meulen, M. Müller, F. Bertram, P. Veit, J. Christen, A. Torres-Pardo, J. M. González Calbet, E. Calleja, J. M. Calleja "*Ordered arrays of InGaN/GaN dot-in-a-wire nanostructures as single photon emitters*" *SPIE OPTO*, 93630U-93630U-8 (2015)

- S. Lazić, E. Chernysheva, Ž. Gačević, H. P. van der Meulen, E. Calleja and J. M. Calleja Pardo "*Dynamic control of the optical emission from GaN/InGaN nanowire quantum dots by surface acoustic waves*" *AIP Advances* 5, 097217 (2015)

- E. Chernysheva, Ž. Gacević, N. García-Lepetit, H.P. van der Meulen, M. Müller, F. Bertram, P. Veit, A. Torres-Pardo, J. M. González Calbet, J. Christen, E. Calleja, J.M. Calleja and S. Lazić "*Blue-to-green single photons from InGaN/GaN dot-in-a-nanowire ordered arrays*" *Europhysics Letters* 111, 2 *perspective* (2015)

- Ž. Gačević, M. Holmes, E. Chernysheva, A. Torres-Pardo, J. M. González Calbet, Y. Arakawa, E. Calleja, and S. Lazić "*Non-polar, semi-polar and polar III-nitride dot-in-a-wire sources of linearly polarized single photons*" submitted (2016)

- E. Chernysheva, Ž. Gačević, E. Calleja, J.M. Calleja and S. Lazić "*Charge distribution and exciton emission intensity modulation studied by stroboscopic analysis with surface acoustic waves*" in preparation (2016)

OTHER PUBLICATIONS

- M. Maragkou, C. Sánchez-Muñoz, S. Lazić, E. Chernysheva, H. P. van der Meulen, A. González-Tudela, C. Tejedor, L. J. Martínez, I. Prieto, P. A. Postigo, and J. M. Calleja "*Bichromatic dressing of a quantum dot detected by a remote second quantum dot*" *Physical Review B* 88, 075309 (2013)

- E. A. Chernysheva, A. V. Sakharov, N. A. Cherkashin, W. V. Lundin, and A. F. Tsatsulnikov "*Investigation of reactor pressure effect on optical properties of MOVPE grown InGaN heterostructures*" Scientific technical statements, St Petersburg State Polytechnical University , 2(146), 32 (2012)

PARTICIPATION IN CONFERENCES

- E. Chernysheva, Ž. Gačević, H. P. van der Meulen, E. Calleja, J. M. Calleja and S. Lazić "*Acoustically induced dynamic tuning of the optical emission from GaN/InGaN nanowire quantum dots*" XVIII JJC INC, Madrid, Spain, 2015 (oral)

- Ž. Gačević, S. Lazić, E. Chernysheva, A. Torres-Pardo, J. M. González Calbet, J.M. Calleja and E. Calleja "*Arrays of GaN nanowires hosting polar and semi-polar InGaN quantum dots*" ICNS-11, Beijing, China, 2015 (poster)

- E. Chernysheva, S. Lazić, Ž. Gačević, N. García-Lepetit, H. P. van der Meulen, E. Calleja and J. M. Calleja "*InGaN single photon emitters modulated by surface acoustic waves*" ICNS-11, Beijing, China, 2015 (oral)

- E. Chernysheva, S. Lazić, H.P. van der Meulen, J.M. Calleja and K. Pierz "*Electric field dependent fine-structure splitting in single InAs/AlAs quantum dots*" ICPS, Austin, Texas, 2014 (poster)

- E. Chernysheva, S. Lazić, Ž. Gacević, N. García-Lepetit, S.Albert, A. Bengochea-Encabo, M. Müller, F. Bertram, J. Christen, H.P. van der Meulen, J.M. Calleja, and E. Calleja "*Single photon emitters based on (In,Ga)N nano-disks embedded into ordered arrays of GaN nanowires*" ICPS, Austin, Texas, 2014 (oral)

- S. Lazić, E. Chernysheva, Ž. Gacević, N. García-Lepetit, S.Albert, A. Bengochea-Encabo, M. Müller, F. Bertram, J. Christen, Herko van der Meulen, J.M. Calleja, and E. Calleja "*Ordered arrays of single photon emitters based on (In,Ga)N nanodisks embedded in GaN nanowires*" CSWEEK, Montpellier, France, 2014 (oral)

- E. Chernysheva, S. Lazić and J.M. Calleja "*Semiconductor nanostructures for generation of polarization entangled photons*" Proceedings of 6th NTT-BRL School, Atsugi, Japan, 2013 (poster)